Assessing the Structural Performance of Cold Spray Additive Manufacturing on Retrofitting Steel Elements

Evi Troulis

Assessing the Structural Performance of Cold Spray Additive Manufacturing on Retrofitting Steel Elements

by

Evi Troulis

To obtain the degree of Master of Science at the Delft University of Technology,
defended publicly on Thursday January 29, 2026

Student Name	Student Number
E. Troulis	6057837

Chair:	Prof.dr. M. Veljkovic
Daily Supervisor:	Dr. F. Kavoura
External Member:	Prof.dr. H. Jonkers
Committee Member:	B. Schagen
Faculty:	Faculty of Civil Engineering and Geosciences

Cover: Technology Connection Solvable by geralt via Pixabay,
Pixabay License (Modified)

Contents

List of Tables

List of Figures

Acknowledgments

I would like to thank my thesis committee, Milan Veljkovic, Florentia Kavoura, Henk Jonkers, and Brian Schagen, for their guidance and feedback throughout this project. I am particularly grateful to Yufei Zhang for generously sharing her expertise in ABAQUS modeling and for her guidance during the development of the numerical models. I also thank Iman Shakeri for providing valuable insights into fracture mechanics and finite element modeling.

I further acknowledge the University of Massachusetts and Vic Obdam for sharing research materials and resources relevant to this study.

Finally, I would like to thank my family and friends for their constant encouragement and support throughout my years of study. Their continued support helped me through both rewarding and challenging periods of my academic journey.

Summary

Overconsumption, loss of biodiversity, and global warming are pressing issues that have driven the EU and the Netherlands to adopt policies towards a fully circular economy by 2050. In the Netherlands, construction is one of two largest consumers of steel, accounting for 32% of the national steel use. This thesis addresses the growing need to reduce construction material consumption and carbon emissions to support these new regulations. This is done by exploring methods to retrofit and extend the technical lifespan of existing structural steel components. Cold spray additive manufacturing (CSAM) is investigated as a method to restore an end-of-life (EoL) steel riveted connection and extend its lifespan with partial disassembly of the full structure.

CSAM works by accelerating powdered feedstock, which consists of micron-sized metal particles, to a high velocity. The particles bond onto the substrate upon impact to form a multi-layered deposit. The bonding, mechanical properties, and porosity of the resulting material heavily relies on process parameters. Nitrogen is commonly selected as an affordable gas type for this process, and when paired with annealing, it is the most feasible method for producing 316L stainless-steel deposits with ductile mechanical properties suitable for structural applications.

Two parametric finite-element models were developed in ABAQUS to investigate how the mechanical response of steel–deposit composites is influenced by deposit percentage, substrate strength, and interface bonding conditions. The main findings are summarized as follows:

- Model A.1: Substrate material significantly affects composite behaviour. Coupons with an S355 substrate exhibited higher strength and ductility than those with S235. As the cross-section became increasingly deposit-dominated, tensile strength continued to increase while ductility reached a plateau. The S235 substrate showed a stronger sensitivity to retrofit percentage due to the larger mismatch in tensile strength between the substrate and deposit materials.

- Model A.2: Increasing the retrofit percentage enhanced the difference in peak load between full-shear and no-shear interaction assumption, Insufficient bonding reduced load-carrying capacity, partly due to substrate material removal required for retrofitting. These results indicate that for applications involving large retrofit volumes, experimental characterization of interface behaviour is essential.

Additional ABAQUS models representing damaged bolt holes with fatigue-induced cracks were used to assess the potential of CSAM for defect rehabilitation:

- Model B: Crack-propagation analyses demonstrated up to a 935% increase in uniaxial load capacity prior to fast fracture.

- Model C: Ductile-damage simulations showed 139.8% improved load capacity due to the increased effective cross-section. Due to the substantial mechanical mismatch between the deposit and substrate materials, interface debonding governed

failure even under full shear-interaction assumptions. This limitation is primarily attributed to the deposit orientation being perpendicular to the loading direction, in contrast to the parametric study of model A.1

Overall, the results indicate that CSAM can significantly improve structural performance, but success depends on bond quality and mechanical compatibility between deposit and substrate. Selecting powders with properties closer to S235 steel would improve predictability and reduce premature interface failure for cases where the load and interface are perpendicular. A life cycle analysis showed that CSAM retrofitting has a much lower carbon footprint than recycling or manufacturing new steel elements if the rivets are replaced with reusable bolts. When rivets are utilized, the global warming potential (GWP) of CSAM is estimated to be 65% greater than the recycling scenario. This LCA relies on several assumptions regarding CO_2 emissions and lifespan extension resulting from CSAM application. It is thus subject to change, once EPD and experimental data specific to 316L powder is available.

Cold spray additive manufacturing offers a promising method for remanufacturing reclaimed steel elements in an environmentally conscious way. While further experimental validation and powder optimization are needed, CSAM has high potential as a viable option toward high-quality steel reuse and a more circular construction economy.

Abstract

The overconsumption and depletion of raw materials have increased pressure for the EU and the Netherlands to adopt policies towards a fully circular economy by 2050. This transition has raised the demand for reuse of materials, thus increasing the need for retrofitting technology. End of life (EoL) steel elements have undergone damages that new elements have not, such as corrosion, cross-section loss, and fatigue cracking at riveted connections. The potential of lifetime extension through cold spray additive manufacturing (CSAM) of EoL structural steel elements, particularly in bridges with riveted connections, was explored through FEM modeling in ABAQUS. First, the composite behavior of a S235 steel substrate retrofitted with annealed 316L CSAM powder was studied, followed by a study of the effect of full-bonding and no-bonding between the two materials. This parametric analysis indicated that structural performance is confined by substrate mechanical properties, retrofit volume, and bonding quality at the interface. Retrofitted crack specimens exhibited a 935% increase in allowable uniaxial load before fast fracture, while ductile-damage simulations revealed that mismatched material strengths can lead to premature debonding when loading is perpendicular to the interface. This is true even when full-shear-interaction properties are defined. A life cycle assessment demonstrated that due to the added maintenance requirement of CSAM-retrofitted elements, replacing a fatigue-damaged steel connection with recycled steel is the most favorable solution. This is because when using rivets, the global warming potential (GWP) emissions are the lowest at $6.72\,\mathrm{kg\,CO_2}$, without jeopardizing the structural stability. The CSAM-retrofitted connection yields the lowest CO2 emissions at $1.35\,\mathrm{kg\,CO_2}$ only when reusable bolts are used instead of rivets. Regardless of the bolt type used, there are several assumptions that must be proven or countered before CSAM is considered a structurally reliable solution.

Chapter 1

Introduction

1.1 Introduction to Problem

Global population growth and rapid industrialization have intensified pressures on environmental systems, leading to overconsumption of raw materials, biodiversity loss, and global warming. Global demand for fossil fuels, metals, and minerals is projected to double within forty years, while annual waste generation may increase by 70% by 2050 [2]. In response, the EU and the Netherlands have introduced policies to mitigate these impacts and support long-term environmental sustainability.

The EU Circular Economy Action Plan (2020) complements the Netherlands' Circular Economy program, which outlines four key objectives for achieving a fully circular economy by 2050:

- Reducing raw material consumption
- Substituting raw materials
- Extending product life through reuse and retrofitting
- High-grade processing through recycling

These goals primarily focus on reducing raw material consumption, thereby decreasing the need for their trade and production [3]. Increasing the reuse and recycling of raw materials holds significant potential for environmental and economic benefits in the Netherlands and the EU.

The Netherlands produced 6.4 million metric tonnes of raw steel in 2024, ranking 26th across the world [4]. Most of this production is attributed to Tata Steel, the country's primary steel manufacturer, which relies on blast furnace technology. In addition, the Netherlands traded over 7 million tonnes of any recyclable material in the year 2023 [5]. While these figures show participation in sustainable practices, further action is required to meet the 2030 and 2050 climate targets. Producers such as Tata Steel must implement new methods to reduce carbon emissions while supporting the needs of the Dutch economy.

Construction is the second largest consumer of steel in the Netherlands, accounting for 22% of national steel use [6]. This highlights the importance of sustainable steel production for the construction sector.

Members of the Steel Construction Agreement share the goal of ensuring that all building materials, including steel, become sustainable. Improving the sustainability of steel in construction can significantly reduce environmental impact, provided quality and safety are maintained. Historically, the Netherlands has exported approximately 60% of its used steel as scrap and recycled the remaining 40%, but recent growth in demolition and circular design has increased demand for high-quality reused materials [7]. The publication of NTA 8713 by Bouwen met Staal provides a step-by-step methodology for the direct reuse of reclaimed steel in new construction, offering a feasible and accessible framework for safe implementation [8].

Challenges to steel reuse include material availability, which may fluctuate with EU-wide demand [7], and regulatory requirements, several of which have already been published. The costs associated with material recovery, specifically regarding time and deconstruction methods, must remain low to encourage client cooperation [9].

This study examines cold spray additive manufacturing (CSAM) as a retrofitting technique to support steel lifetime extension. Originally developed for coating applications, CSAM has evolved into a method for localized damage repair, volumetric filling, feature reconstruction, and crack remediation[10]. While common in the automotive, aerospace, and medical industries, its application to structural steel has only recently gained attention. Restoring original geometries using CSAM can reduce repair costs by avoiding dismantling and transportation [10].

CSAM functions by propelling metal particles at high velocity onto a substrate, producing particle–substrate co-deformation that enables interfacial bonding and mechanical interlocking [10]. The technique is suitable for addressing wear, thermal fatigue, erosion, corrosion, and chemical degradation.

Advancing reuse and retrofitting practices through technologies such as CSAM offers a promising pathway for reducing raw material dependence, extending the service life of steel components, and contributing to the Netherlands' circular economy objectives.

1.2 Research Gap and Significance

Recycling of steel is often advertised as a green solution to the increasing carbon emissions of steel infrastructure, however direct reuse offers even greater environmental benefits.

The publication of NEN NTA 8713 in June 2023 provides the first Dutch technical agreement dedicated to the reuse of reclaimed structural steel. It specifies that unused bolt holes, welds, and any forms of damage must be inspected and accounted for in calculations; however, it provides no framework for retrofitting options. This thesis aims to extend the existing methodology provided in the NTA 8713 to retrofit damaged details found in structural steel that may pose a threat to future construction projects.

The retrofitting method explored is the utilization of cold spray additive manufacturing. Existing research, primarily from the U.S., has focused on restoring the original geometry of end-of-life steel components in infrastructure through CSAM [10][11]. A key research gap is the limited understanding of CSAM performance when applied to various damage types for structural integrity and lifetime extension. CSAM has shown potential as a coating material for corrosion resistance [12], thus new studies sought to explore its potential regarding structural repair. The study by Schagen, for example, studies the use of CSAM on repairing corroded steel beam ends that have undergone severe cross-sectional loss [13]. Many more applications for structural repair through CSAM exist.

The primary damaged detail group examined in this thesis is bolt holes from riveted connections, which are particularly susceptible to fatigue cracking. Concerns regarding old riveted steel bridges have increased due to rising traffic intensity [14]. A recent survey of European bridge infrastructure shows that over 30% of existing steel bridges are more than 100 years old, which is the typical design service life for such structures [15]. These aging bridges are prone to deformation-induced cracking, especially at riveted connections [14], making this a significant issue across Europe.

1.3 Research scope, objectives, and questions

1.3.1 Scope

This research evaluates the effectiveness of CSAM as both a strengthening technique and investigates its influence on the structural performance of EoL riveted elements.

The scope of this thesis concerns the application of cold spray additive manufacturing (CSAM) to structural steel elements. A literature review was conducted to characterize riveted connections, including common cracking patterns, crack locations, and material properties. The structural performance of bolt holes combined with cracking will be investigated through ABAQUS modelling. In addition, CSAM process parameters optimized for corrosion prevention, strength enhancement, and cost-effectiveness were selected based on existing experimental research.

The structural behavior and CO2 footprint of the reclaimed elements, both with and without retrofitting, will be evaluated using available online databases.

1.3.2 Research Objectives

General Objective:

- To assess both the structural and environmental performance of CSAM retrofitting for EoL steel elements in the context of the Netherlands' 2030 and 2050 sustainability goals.

Specific Objectives:

- Determine the effect of cracking and holes on the structural capacity of steel elements through FEM modeling.
- Explore the potential CSAM as a retrofitting option of the abovementioned damages through FEM modeling.
- Study the governing failure mechanisms of the pre and post-retrofitted elements through FEM modeling.
- Determine the carbon footprint of the new structure after retrofitting through cold spray additive manufacturing.

1.4 Research Questions

Considering the given problem statement and objectives, the following research questions and sub-questions arise:

Main research questions:

1. **What factors govern the structural performance of a steel element retrofitted with cold-spray deposited material?**
2. **How does cold-spray remanufacturing influence the overall structural performance of reclaimed steel elements with riveted connection damaged details, and what is the environmental impact of its application?**

Sub questions:

- How can remanufacturing techniques such as CSAM be applied on a reclaimed element's damaged details for reinforcing its cross section performance?
- How does the combined effect of bolt holes and fatigue cracks influence the structural behavior of a steel element in remanufactured and non-remanufactured conditions? How does this compare to the element's original capacity?
- How can ABAQUS modeling be implemented in the context of studying structural damages pre and post retrofitting?
- What are the CO2 emissions induced from the necessary CSAM application found in this research? How do these compare to the CO2 emissions of producing new steel, recycling steel, and reusing steel without retrofitting?

1.5 Thesis Structure

The expected outline of this thesis is demonstrated as follows.

Chapter 1 - Introduction
This chapter provides an introduction to the real-world problem and the relevance of the research. It proceeds with the research gap, scope, research objectives, and research questions.

Chapter 2 - State of the Art
An overview of relevant literature and existing background information that can assist in this thesis is listed in this chapter.

Chapter 3 - Material Properties Selection
This chapter outlines the selected materials for the riveted connection steel and the cold spray deposit, with their corresponding justifications.

Chapter 4 - Research Methodology
In this chapter, the research methodology is presented. The appropriate steps for responding to the main and sub-questions mentioned previously are outlined.

Chapter 5 - FEA Models and Setup
All the outlined models from the methodology are discussed in depth, highlighting the modeling parameters and the reasoning behind them,

Chapter 6 - Results and processing
In this section, the results from the different retrofitting techniques are compared in preparation for the final conclusions.

Chapter 7 - Life Cycle Analysis
An LCA is performed between a newly produced steel plate, a recycled steel plate, and a retrofitted steel plate to assess the CO2 emissions between each variant.

Chapter 8 - Conclusions and Recommendations
The final results are summarized and applied to the real-life problems presented in the introduction.

Chapter 2

State of the Art

2.1 Introduction to State of the Art

The main questions to be answered in these sections are as follows: What is the significance of steel reusability and how is it different from steel recycling? What research has been done to support this?

What are some existing methods for retrofitting damages in steel elements? How have they been used previously and how can they be applied to this thesis?

2.1.1 NTA 8713

The NEN NTA 8713 is the official Dutch technical agreement for the reuse of structural steel. This document details the process of assembling an inspection document with the necessary information required for the safe reuse of structural steel elements. This code only applies when requested by the client, as it is not designated in the building regulations. The end goal of this procedure is that the reclaimed steel still satisfies the requirements set by NEN-EN 1993 [16].

This code does *not* apply to:

- steel from before 1955
- steel from outside the Netherlands
- fatigue-tested steel
- steel under significant plastic deformation
- weather-resistant steel/stainless steel
- cast iron, rivets, and preloaded bolts

Through this research, riveted connections can be considered for reuse as part of future codes, research, and industry applications.

2.2 Structural Damages on Reclaimed Elements

2.2.1 Fatigue Cracking on Riveted Connections

There are two principal damage modes for fatigue cracking on riveted connections of steel bridges [14]:

- Cracking in the connection angles
- Cracking in the rivet

Cracking location and shape forms based on different connection types in the bridge. The following connection types or beam elements are prone to fatigue cracking [15]:

- Beams with reduced depth
- Hangers
- Timber Tie Connections
- Diaphragms and cross-bracing connections
- Stringer to floor beam connections
- Floor beams to main-load-carrying members connections
- Elements with Coped Ends
- Girder Splices connections

One of the most reported types of connections at risk are stringer-to-floor-beam connections [14]. These connections are designed to account for shear forces alone, however they carry some of the end reactions from the floor beams, so they are prone to fatigue cracking. An example can be seen in Figure 2.1 [17]. The cracks usually start at the outstanding leg of the connection angle, which in this case is the stringer beam, and grow along the fillet of the angle.

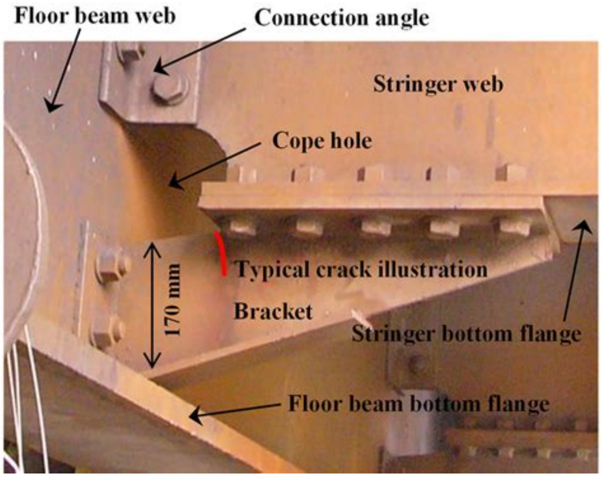

Figure 2.1: Typical Floor-to-Stringer beam connection found in a steel bridge.

Rivet failures are also very common, where cracking starts at the junction between the rivet head and shank. In this case, the rivet heat may come off due to prying and rivet bending. Both cases can be seen in Figure 2.2 [15].

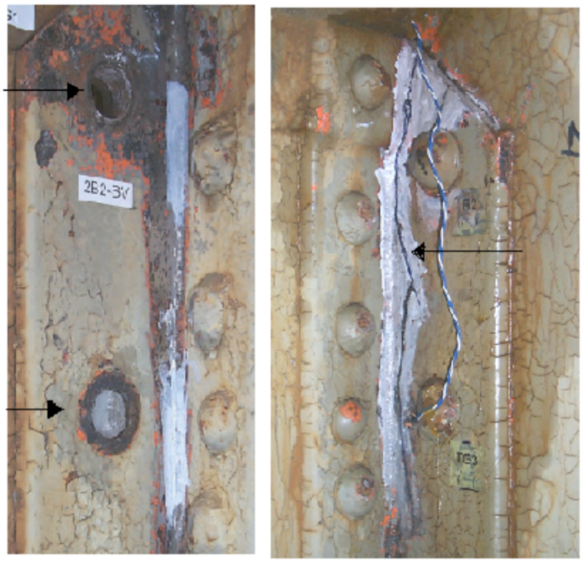

Figure 2.2: Fatigue damage in a stringer-to-floor-beam connection: Cracking in the rivet (left) and cracking in the connection angle (right).

Figure 2.3 demonstrates the typical cracking patterns observed in the case studies in the PhD Thesis by Rosemarie Helmerich [18]. The cracking orientations depend in the location of the rivets along the beam, the connection type, and the loading configuration. The structural performance of Figure A will be explored in this research project, as seen in figure 2.3, as it resembles the most structurally vulnerable crack orientation under axial tensile loading. For the LCA, figure D will be selected, as it most closely resembles the cracking pattern of a stringer-to-floor-beam connection, one of the most common cases of fatigue cracking.

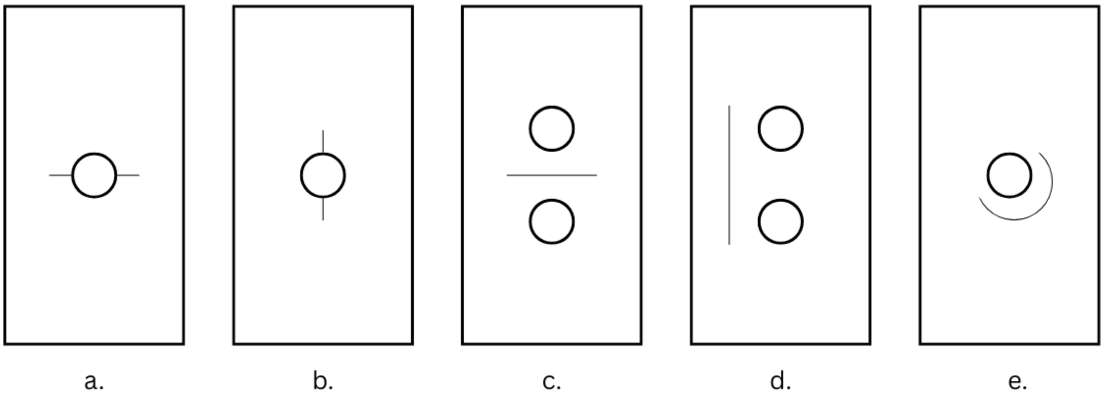

Figure 2.3: Typical Cracking Patterns

Stress Intensity Factor, K

In fracture mechanics, the stress intensity factor, denoted by K, is used to describe the state of stress near the tip of a crack or notch. It provides a useful criterion for predicting failure in brittle materials as well as for assessing fatigue crack propagation [19].

The general expression for K [19] is given by:

$$K = Y\,\sigma\,\sqrt{\pi a} \tag{2.1}$$

where:

- a is the crack length (mm),
- σ is the applied stress (MPa),
- Y is a geometry factor that accounts for the shape and loading configuration (Dimensionless).

This equation is used to represent a Linear-Elastic Fracture Mechanics (LEFM) model, so it must not be applied to a non-linear situation. For non-linear cases, J-integrals must be utilized instead.

There are three distinct stress intensity factors, each corresponding to a different mode of fracture:

- K_I: Mode I (opening mode),
- K_{II}: Mode II (sliding mode), and
- K_{III}: Mode III (tearing mode).

Only mode I falls within the scope of this thesis.

Fracture Toughness, K_{IC}

The plane-strain fracture toughness, denoted as K_{IC}, is a material property that quantifies the resistance to crack propagation under plane-strain conditions. Once the stress intensity factor K exceeds K_{IC}, unstable crack growth occurs, leading to brittle fracture [19][20]. This is referred to as fast fracture.

At the initiation of unstable crack propagation, $K = K_{IC}$, rearranging Equation (2.1) provides the critical crack length a_c:

$$a_c = \frac{1}{\pi}\left(\frac{K_{IC}}{Y\,\sigma}\right)^2 \tag{2.2}$$

Equation (2.2) is useful for predicting failure in structures containing cracks under a given applied stress.

Geometry Factor, Y

The geometry correction factor Y is obtained from the following empirical relation [19]:

$$Y = \frac{1}{1-\frac{a}{d}} \cdot \sqrt{\frac{A + B\cdot\frac{a}{d-a}}{1 + C\cdot\frac{a}{d-a} + D\cdot\left(\frac{a}{d-a}\right)^2}} \tag{2.3}$$

where A, B, C, and D are constants for an external crack in a two-dimensional tensile bar [19].

2.3 Retrofitting Techniques

Several retrofitting methods for steel have been investigated in previous research, including fiber-reinforced polymer (FRP) strips, stop-hole drilling, stiffener rings, shot peening, welding, and thermal spray. These techniques target improved fatigue resistance, corrosion protection, hole strengthening, or overall fatigue performance. cold spray additive manufacturing has been applied in automotive repair and is now being examined for infrastructure applications. This thesis contributes to this emerging research by evaluating CSAM for strengthening corrosion-prone structural steel elements.

2.4 Cold Spray Additive Manufacturing (CSAM)

CSAM differs from thermal spray and welding in that it relies solely on kinetic energy for coating formation, with process temperatures remaining below the particle recrystallization temperature [21]. The feedstock thus remains solid, while elevated gas temperatures soften particles to promote plastic deformation upon impact. A schematic process of CSAM is shown in Figure 2.4 [22].

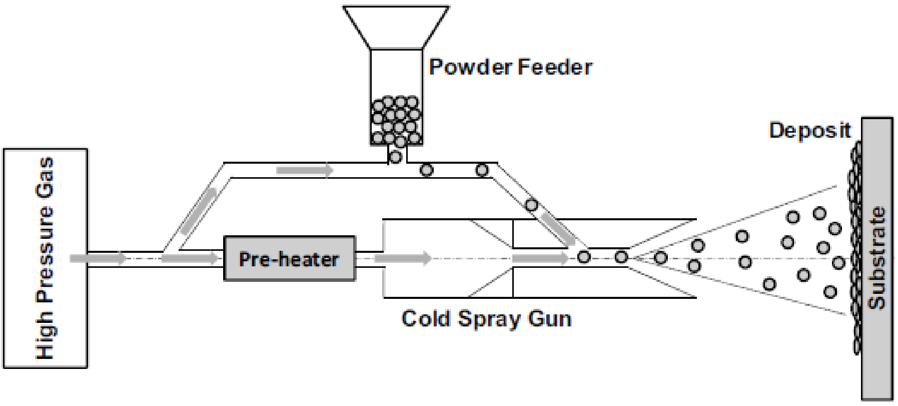

Figure 2.4: Typical Cold Spray applicator.

The CSAM deposit quality depends on the deposition efficiency [10], which is obtained through high impact velocity of the feedstock powder onto the substrate. It characterizes a deposit that has high tensile strength, high hardness, and low porosity. Efficient deposition is defined by the categories shown in figure 2.5 [23].

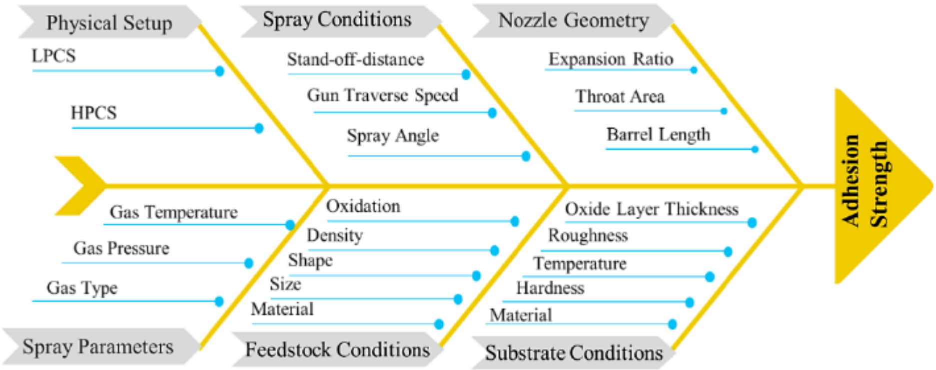

Figure 2.5: Parameter categories influencing adhesion properties of CSAM deposit.

Each plays a significant role in the impact velocity of the powder and thus directly affects the mechanical properties of the deposit. A table summarizing some typical parameters and their influence on the deposit is found in Table 2.2.

2.4.1 Physical Setup

Cold spray coatings can be produced through two main setups: low-pressure cold spray (LPCS) and high-pressure cold spray (HPCS). These two primarily differ in particle velocity and resulting kinetic energy. HPCS achieves higher velocities to the particles, producing adiabatic shear bands upon impact, which enhances interfacial bonding, thus resulting in dense coatings with low porosity [23]. LPCS particles have lower velocities, leading to more uniformly flattened splats, weaker inter-particle cohesion, and lower deposition efficiency. Additionally, LPCS particles may rebound or induce a shot-peening effect in the upper layers, which increases porosity and reduces density, whereas HPCS coatings do not exhibit this effect because particle velocities exceed the critical velocity, allowing efficient interaction with the substrate and previously deposited layers. These differences can be observed through micro structural analysis, with HPCS coatings achieving higher deposition efficiency and more ideal interface properties compared to LPCS [23].

2.4.2 Spray Parameters

Cold spray uses nitrogen, air, or helium to accelerate powder feedstock to a high-velocity (over 300 m/s), which induces deposition when impacted onto a substrate. This feedstock remains solid during the entire deposition process. Higher gas pressure, higher gas temperature, and lower gas molecular weight can increase particle impact velocity. While this leads to improved deposit quality, it can also increase the residual stresses in final product unless gas temperature is elevated [10]. According to a research study, the particle impact velocity heavily depends on the gas properties selected, which can be seen in Figure 2.6 [24]. In this figure, helium is shown to achieve a 1000 m/s particle impact velocity at 200 °C and 2 MPa of pressure, as compared to nitrogen's 550 m/s at the same temperature and 3 MPa of pressure.

For nitrogen to be used for successful deposition, several conditions must be met according to the particle type and size, which can be picked based on the software Kinetic Spray Solutions [25]. Some studies showed that heating the powder to match the temperature of the Nitrogen gas limits the temperature losses during the deposition process, thus maintaining high impact velocity and acceleration. This helps achieve dense deposits and efficient deposit material properties [22]. High ultimate tensile strengths (UTS) and low porosity percentages were recorded when using high gas temperature for N2-based cold spray systems [22][26]. Heating nitrogen gas can increase its pressure, which then accelerates the particles to the required critical velocity to ensure bonding and proper deposition. As seen in figure 2.6, using a 1000 °C gas temperature for the N2 CSAM system while increasing the pressure to 4 MPa, the particle velocity can increase to 800 m/s, a significant improvement from 550 m/s.

It is shown that CS parameters can be optimized for nitrogen-based deposit to yield similar stiffnesses and yield strengths as a helium-based deposit [25], however the He-based system will yield significantly more ductile deposits [22]. In addition, the fracture morphology is dominated by different failure mechanisms for each system. While He-based fails due to particle fracture, N2-based fracture morphology fails due to particle interface debonding [22]. It can be deducted that while the particles may bond to the substrate with both systems, the particles do not bond with each other in the N2-based CS system, while in the He-based system they act more uniform. Figure 2.7 displays the stress vs strain curve of two cold sprayed specimens, one for each gas type [22]. The He-based deposit reaches a fracture strain of 0.035, while the as-sprayed N2-based deposit fractures before reaching 0.01.

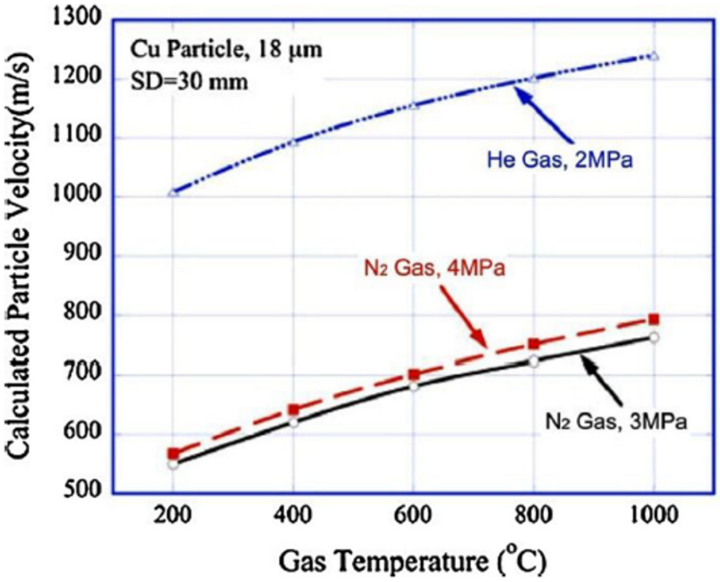

Figure 2.6: Particle impact velocity depending on different gas types, gas pressures, and gas temperatures.

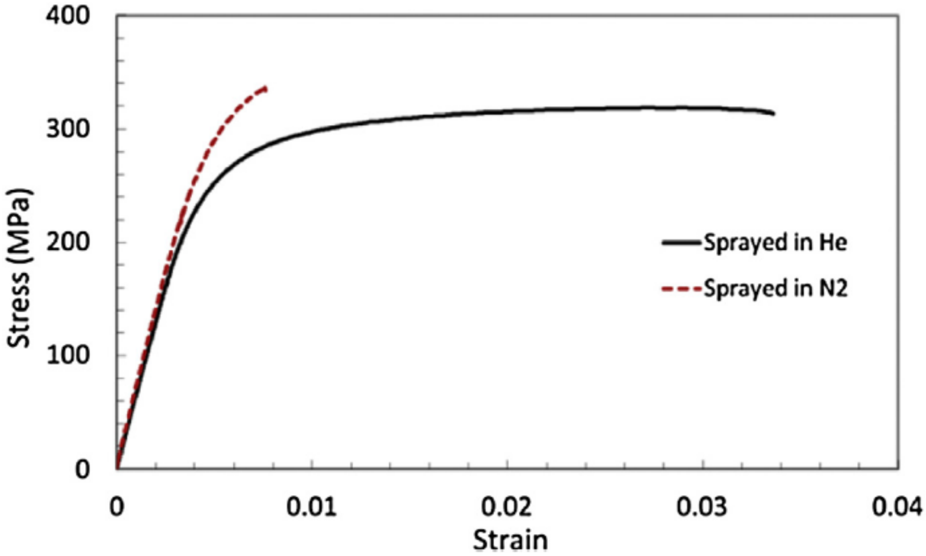

Figure 2.7: Stress vs Strain curves of deposits sprayed in He and N2.

2.4.3 Feedstock Conditions

The powder feeder rate is the quantity of powder introduced into the nozzle per unit time, documented in rotations per minute (RPM). Particle velocity decreases as powder feed rate increases. Higher feed rates reduce deposition efficiency, hardness, and tensile strength, and increase porosity while maintaining a constant gas flow. High feed rates result in thicker deposits with sharper track profiles. Avoid high powder feed rates for CSAM. This variable can be affected by powder feed shape, size, and material type. When determining how the feed rate influences impact velocity, it is important to also consider nozzle traverse speed.

Typical particle materials used for cold spray are materials with "smaller heat capacities, such as copper, aluminum, and titanium" as they are softer and better able to avoid the formation of heat-affected zones and thermal residual stresses, protect against oxidation, and perform better as coating material [21]. These feedstock materials can be good for preventing corrosion buildup on existing elements. In another study, an alumina and zinc mix, which when sprayed under the optimum CSAM parameters, it can perform well for anti-corrosion applications [27]. A study by Spencer and Zhang showed that mixed sizes of particles resulted in low porosity.

Different sphericity levels are one of the parameters influencing the powder feed rate and particle velocity. A study by Sinnwell explores different particle sphericities, varying from 0.76 to 0.96. In this study, the results revealed that "irregular particles experienced greater acceleration and produced a more focused spray pattern" in contrast to the spherical particles, which "attained lower maximum velocities and exhibited broader dispersion within the jet" [28]. How this parameter influences the deposition quality can be further explored.

2.4.4 Spray Conditions

The deposit quality is influenced by the CSAM standoff distance, spray angle, and nozzle trajectory. Stand-off distance is citical for ensuring that uniform coatings of optimal quality are achieved, which studies have shown is achievable at shorter distances [23]. The spray angle significantly affects particle deformation, adhesion, and coating properties. While perpendicular spraying is generally considered ideal, studies indicate that slightly inclined angles (e.g., 60°) can enhance adhesion strength through residual compressive stresses, although the relationship is not fully resolved [23]. Tables 2.3 and 2.4 show some typical CSAMN parameters and deposit mechanical properties.

2.4.5 Nozzle Geometry

The design of the cold spray nozzle plays a significant role in determining particle velocity and adhesion strength at the interface between the substrate and deposit. Increasing the nozzle barrel length generally increases particle velocity, while the nozzle outlet diameter must be optimized to achieve the best expansion ratio. For example, a diameter that is too large may reduce velocity. Other design parameters, such as the section length, throat size, particle size, and process gas, also affect the particle acceleration. Circular nozzles typically produce higher particle velocities compared to elliptical or square designs. Nozzle geometry and dimensions are thus critical for optimizing particle impact velocity and ensuring strong bonding at the substrate.

2.4.6 Substrate Condition

The cold spray parameters play a major role in the adhesion between substrate and deposit, but the substrate conditions also influence the adhesion between the two. Some of the substrate characteristics that are critical are surface roughness, material, hardness, pre-heating, and oxide layer thickness. Surface roughness affects particle interfacial bonding, with smoother or mirror-finished substrates generally providing higher adhesion, as they have reduced gaps and improved particle-substrate contact [23]. The substrate's thermal properties also play a role, since they allow for soft-on-hard contact between the two materials. In this case, the soft material deforms during deposition, leading to adiabatic shear instability and stronger metallurgical bonding. Pre-heating can support this by softening the substrate surface. Finally, oxide layers play a major role in the bonding, as thicker layers reduce deposition efficiency by preventing particle penetration. By removing these layers, direct contact between the deposit and substrate is possible, thus improving the adhesion between the two metals [23].

2.4.7 Critical Velocity

Cold spray bonding initiates when the first particle layer adheres to the substrate, followed by continued build-up of particle layers. Both bonding and growth stages depend on achieving a material-specific critical velocity v_{crit}, which increases with particle strength, size, and temperature [10]. Typical particle diameters range from 20–60 μm. Increasing particle impact velocity enhances deposition efficiency, reduces porosity, and improves mechanical properties due to more effective metallic bonding.

If impact velocity is too high, local melting may occur and compromise coating integrity; if too low, particles rebound or erode the substrate [12]. The ratio $\eta = v_{\text{imp}}/v_{\text{crit}}$ is commonly used to assess the effectiveness of deposition, with deposit quality improving rapidly when $1.0 < \eta < 1.5$ [26]. Representative η values and behaviors are summarized in Table 2.1. The manufacturing parameters used in this study follow established guidelines for optimizing deposition efficiency (DE). In figure 2.8, the relationship between DE and impact velocity is shown, according to a study by Assadi [29].

η	**Correlated System Behavior**
< 1.0	Bonding does not occur
≈ 1.0	Bonding occurs. Low deposition efficiency and limited deposit performance
1.0–1.5	Steep linear increase in tensile strength and deposition efficiency as η increases.
≈ 1.5	Good deposit quality in terms of strength
> 1.5	Work hardening effects, decrease in strength

Table 2.1: Typical values and interpretation of η in cold spray impact models.

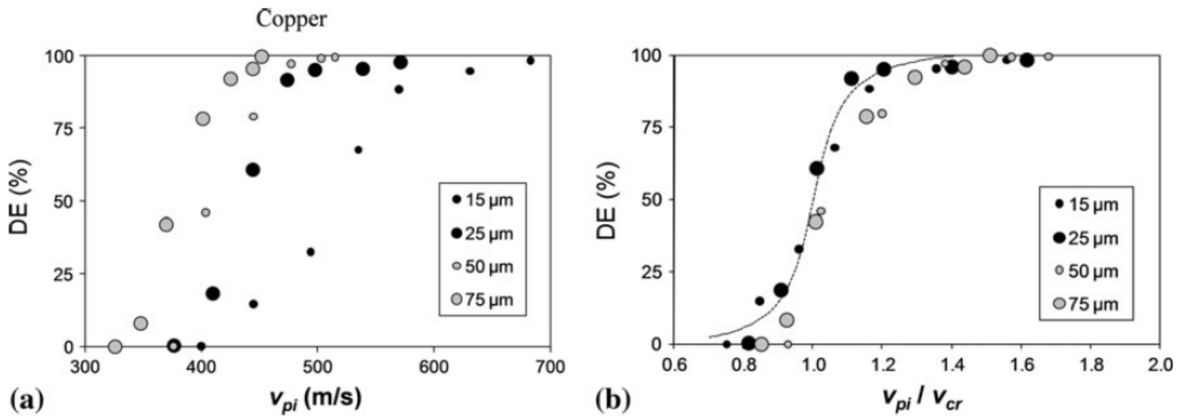

Figure 2.8: Relationship between (a) particle impact velocity v_{pi} and (b) η and the deposit efficiency DE for copper particles of different sizes.

2.4.8 As-Sprayed CSAM

As-sprayed deposits exhibit high strength but reduced ductility due to severe plastic deformation and residual stress accumulation during impact [30, 31]. Residual stresses vary across the interface: the substrate typically develops beneficial compressive stresses from shot-peening effects, whereas tensile stresses may appear within the deposited layer and at the interface [32]. These stresses become more significant for thicker coatings.

Insufficient particle deformation or suboptimal parameters lead to porosity, weak interparticle bonding, and susceptibility to cracking under tensile loads [30]. Although adhesion to the substrate generally occurs, particle–particle bonding is often the limiting factor for mechanical performance [31]. Previous work using 316L stainless steel demonstrated that optimized N_2-based cold spray can achieve low porosity and high strength despite low ductility [25], which aligns with the intended in-situ conditions of this thesis.

Residual stresses and shot peening effects are neglected when CSAM is used in a coating-only setting and the deposit layer is approximately 2 mm. For deposit layers thicker than this, stresses in the substrate may pose a risk.

2.4.9 Heat-Treated CSAM

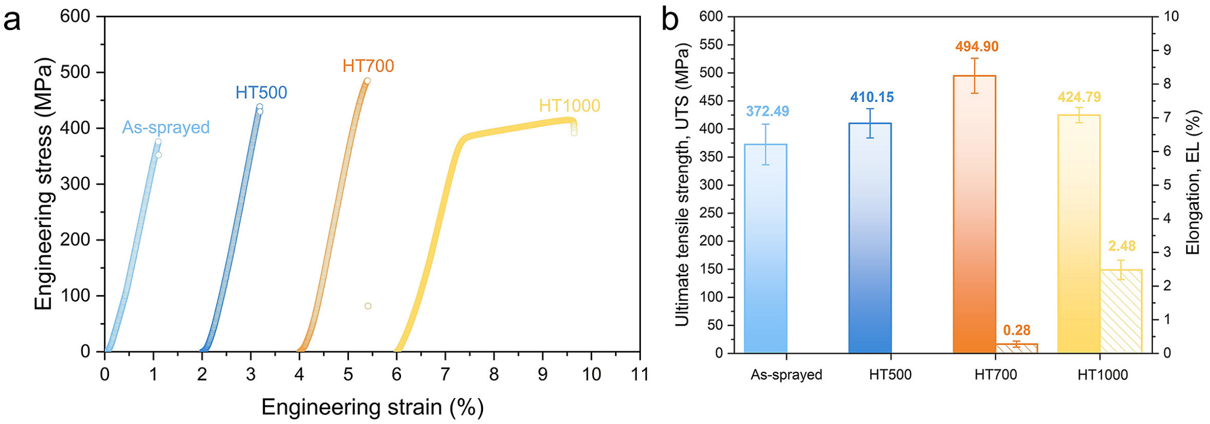

Figure 2.9: Effects of different annealing temperatures on strain and UTS of CoCrFeNi deposit.

Heat treatment significantly improves the mechanical performance of cold-sprayed deposits by promoting atomic diffusion, metallurgical bonding, and grain growth [33]. Post-process treatments, particularly annealing, enhance ductility and reduce hardness by eliminating pores and improving particle interlocking [30, 31]. Studies show that temperatures near 1000°C are often required to achieve substantial ductility improvements in alloys such as CoCrFeNi.

Hot rolling can also enhance strength and plasticity but is not suitable for in-situ applications [31]. Although heat treatment provides clear benefits, its application to full-scale infrastructure elements remains as a limitation. For this thesis, annealing heat treatment is included, assuming that it is possible during the application process.

The pre and post heat treatment effects can be seen in figure 2.9 [30], which displays the tensile properties of different deposits at different annealing temperatures. On the right, it is shown that after a temperature of 700 °C, some ductility appears in the specimen. The stress-strain curves for each specimen is shown on the left, which are shifted horizontally for visual clarity. Interpretation of results shall be based off of relative strain rather than the actual strain shown.

2.4.10 CSAM for anti-corrosion resistance

Geometrically complex components such as bolted connections often retain residual rust even after treatment, making them prone to renewed corrosion [27], pictured in figure 2.10a [27]. Cold spray offers potential as an anti-corrosion strategy because dense, low-porosity deposits (e.g., aluminum, alumina, zinc) can block oxygen and moisture ingress [12].

Effective bonding to rusted substrates requires the rust layer to possess sufficient hardness to withstand particle impact, while the sprayed material must be softer to allow plastic deformation and mechanical anchoring [27]. This mechanism aligns with the “anchoring” bonding mode described by Raoelison [34]. Alternative approaches use an intermediate soft layer (e.g., WIP-BC1) to promote anchoring when both substrate and particles are hard [13], which is captured in figure 2.10b [13]. For the purpose of this thesis, full bonding between CSAM particles and the corrosion layer is assumed.

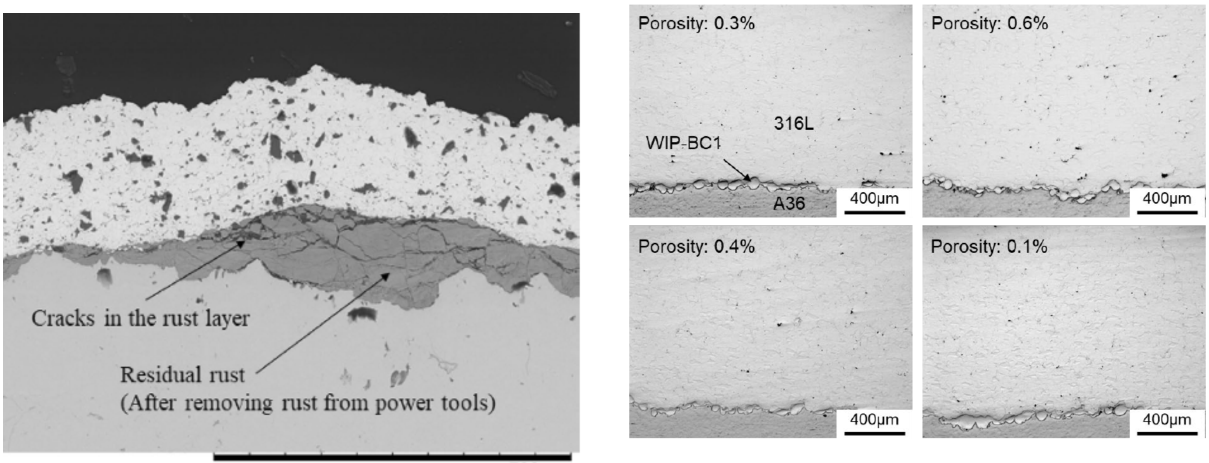

(a) Cracking in rust layer, below CS deposit.

(b) Micrographs of the deposited WIP-BC1 layer and 316L powder.

2.4.11 CSAM for structural steel strength reinforcement

The structural contribution of CSAM depends strongly on deposit microstructure and material type. As-sprayed layers often show reduced tensile strength due to porosity and incomplete interparticle bonding [26, 31]. After heat treatment, however, significant increases in strength and ductility have been documented for various alloys, including Ti and CoCrFeNi [24, 30, 31].

Research shows that the deposit material plays a major influence on the strength added to the substrate, and at times it may reduce the strength without heat treatment. Instead, the CSAM parameters will be optimized to minimize porosity and increase deposit efficiency. This way, the strength and bonding of the deposit may be sufficient to prevent corrosion buildup and existing fatigue-crack propagation.

Utilizing 316L steel addresses both preventing further corrosion and strengthening the cracked elements. Stainless steel resists corrosion formation, and the optimized parameters in the Bagherifard study [25] provide ample structural capacity of the deposit material. Including the assumption that annealing is possible, the deposit is expected to perform well under tensile load.

Parameter	**Influence**
Feedstock Conditions	
Size	Small size → higher V_{crit} required [35]; Small size → higher V_{impact} [35]; Size range → lower porosity of deposit [35]
Shape	Sphericity → lower has higher particle impact velocity [28]
Powder feed rate	Lower → higher particle impact velocity [10]
Spray Parameters	
Gas type	Molecular weight (high → inefficient deposit)
Temperature	High → Impact velocity [1]**
Pressure	High → Impact velocity**
Spray Conditiong & Nozzle Geometry	
Standoff distance	Ideal range: 30–90 mm → highest DE [10]
Spray angle	90° → best deposition efficiency [10] & adhesion [23]
Nozzle dimensions	Can impact particle impact velocity, gas consumption, and particle flow
V_{imp}	High → efficient deposit [10]
Eta (η): $\eta = v_{\mathbf{imp}}/v_{\mathbf{crit}}$	≈ 1.5 → efficient deposit, bonding [26]; <1.0 → no bonding, erosion of substrate [1]; >1.5 → melting of particles/erosion of substrate [29]
Porosity	Low → less corrosion formation, more ductility [27]
Microhardness	High particle hardness → bonding to substrate through embedment/anchoring [34]
Flattening ratio: $1 - \frac{h_p}{d_p}$	Higher particle deformation → less porosity, higher bonded area, high cohesive strength [29]

Table 2.2: Summary of process and material parameters influencing deposition and bonding quality. **Both gas temperature and pressure influence the particle velocity, however, if the temperature is too low, the particles will not deform plastically (affects bonding and porosity). If the pressure increases too much, the particles risk eroding the substrate, which may lead to a porous deposit. This being said, increasing temperature should be prioritized as a form of increasing V_{imp} [1].

Parameter	**Influence of Ductility on Fracture...[26]**	**Microstructural evolutions and mechanical...[31]**	**Microstructure evolution and mechanical behavior of...[30]**	**Microstructure optimization of cold sprayed Ti-6Al-4V...[24]**	**Analysis of the residual stress and bonding...[32]**	**Feasibility of 3D Printing Applications... [13]**
Gas Parameters						
Gas Type	N2	N2	N2	N2, He	He	N2
Gas Pressure	5.0 MPa	4.0 MPa	5.0 MPa	N2: 5.0 MPa He: 2.0 MPa	0.62 MPa	6.21 MPa
Gas Temperature	700°C, 850°C, 1000°C	800°C	900°C	1000°C	140°C 132°C	650°C
Powder Feeder Parameters						
Particle Shape	Spherical	Spherical	Spherical	Spherical	Spherical	Spherical
Particle Material	Ti, Cu	Ti	CoCrFeNi	Ti-6Al-4V	AA6061-T6/AA-6061 Pure Al/Mg	SS08 Si: 0–1%; Cr: 39–43%; Fe: BAL; Mn: 0–1%; C: 4–5%
Particle size	–	–	15–90 μm	45 +15 μm	15 μm	15.09–47.33 μm
Powder Feed Rate	–	–	–	5 g/min	–	4 RPM for WIP 8 RPM for SS08
Substrate	AlMg3	Q235 steel plates	Cu	Stainless Steel	AA-6061-T6	NA
Nozzle Parameters						
Nozzle Traverse Speed	250 mm/s	5 mm/s	–	–	1025 m/s	200 mm/s
Standoff Distance	60 mm	20 mm	40 mm	20 mm		10 mm
Spray Angle	–	90°	90°	90°		90°
Nozzle Diameter/Length	Nozzle type: Out 1	2–8 mm / 130 mm	–	Out 1		–
Impact Speed:					585 m/s	NZZL0060, 200 mm barrel length 2 mm throat diameter
As-Sprayed Tensile Strength Parameters						
UTS (MPa) (respective according to temperature)	**Ti:** 279, 326, 442 **Cu:** 174, 289, 282	306	–	≈ 300		211 ± 18 (tension)
YS (MPa)	–	≈ 290	≈ 380	–		211 ± 18 (tension)
Elongation %	**Ti:** 0.2, 0.2, 0.3 **Cu:** 0.1, 5.3, 17.5	2.5	1.0	0.1		0.18
Porosity %	**Ti:** 7.0, 1.5, 0.7 **Cu:** 0.1, 0.1, 0.0	–	–	2.6%		–
Elastic Modulus (GPa)	–	–	–	–	–	163 ± 76 (tension)

Table 2.3: CSAM parameters and mechanical properties for studies excluding 316L powder.

Parameter	**Tailoring cold spray additive manufacturing of steel 316 L for static and cyclic load-bearing applications[25]**	**Optimisation of stainless steel cold spray coatings using mixed particle size distributions[35]**	**Feasibility of 3D printing applications for highway infrastructure [13]**
Gas Parameters			
Gas Type	N2	He	N2
Gas Pressure	5.0 – 6.0 MPa	0.62 MPa	6.21 MPa
Gas Temperature	1000 – 1100°C	320°C	650°C
Powder Feeder Parameters			
Particle Shape	Spherical	Spherical	Spherical
Particle Material	Steel 316L	316L	316L
Particle size	19 – 45 (coarse) 12 – 29 (fine)μm	5 μm, 10 μm, 22 μm	15.09–47.33 μm
Powder Feed Rate	–	10 g/min	4 RPM for WIP 8 RPM for SS08
Substrate	NA	AZ91E	A36 steel
Nozzle Parameters			
Nozzle Traverse Speed	500 mm/s	50 mm/s	200 mm/s
Standoff Distance	30 mm	12 mm	25 mm
Spray Angle	90°	90°	90°
Nozzle Diameter/Length	Out 1; 160 mm length	Convergent barrel nozzle Mach 1 choked flow	NZZL0060, 200 mm barrel length 2 mm throat diameter
Impact Speed	–	Gas speed: 1245 m/s Particle speed: inversely proportional to particle size	–
As-Sprayed Tensile Strength Parameters			
UTS (MPa)	600 – 750	–	140 – 240
YS (MPa)	–	–	140 – 240
Elongation %	≈ 0.47	–	≈ 0.1
Porosity %	≈ 0.75%	22 μm: 4% 5 & 10 μm mix: < 1%	–
Elastic Modulus (GPa)	–	–	–

Table 2.4: Parameters and properties of cold spray processes using 316L stainless steel powders.

Chapter 3

Material Properties Selection

3.1 Substrate Material

In this research study, S235 steel is assumed. This choice reflects the typical steel grade historically adopted in European standards for riveted steel connections [36], while also offering a close similarity in structural properties to ASTM A36 steel commonly used in the United States [13]. Therefore, selecting S235 is both consistent with historical European structures and relevant to present-day American research using A36.

The material properties can be seen in table 3.1. The fracture toughness of S235 steel was taken from an experimental study by Seitl [37]. The plotted results from this study are shown in figure 3.1a.

Material Property	Value
UTS	370 MPa
YS	235 MPa
Elongation	0.22
Young's modulus	210 GPa
Fracture toughness	22.5 $MPa\sqrt{m}$

Table 3.1: Material properties of S235 steel.

3.2 CSAM Parameters

The selected parameters for the cold spray system in tension were selected based on the study by Bagherifard [25], which can be seen in table 3.2. The reason that this study was used is because it offered experimental data for both tensile and fatigue tests of high-strength CSAM deposit. This way, the structural behavior of a high-strength deposit was able to be analyzed through FEA modeling without requiring CSAM equipment, which was a major limitation in this thesis.

In addition to this, it provided data for as-sprayed deposits and different heat-treatments. In this thesis, the annealed properties will be applied in the ABAQUS models to test whether 316L CSAM deposit is adequate for retrofitting elements undergoing tensile loads. Since the as-sprayed deposit is brittle, it is not ideal for tensile loading.

The annealed data can be utilized assuming that annealing can be applied in-situ. The annealing temperature and time duration must be greater than 1000 °C for one hour for uniform recrystallization to occur in the 316L deposit particles [25]. The properties of the as-sprayed and heat treated deposit can be seen in table 3.3.

The breadth of data that is available from the Bagherifard study allows for a parametric study of different post-processed deposits and their potential to retrofit fatigue-cracked riveted connections. This can be done in a subsequent study.

Parameter Type	**Value**
Powder	316L stainless steel
Size	19–45 μm (Coarse)
Shape	Spherical
Powder feed rate	–
Gas type	N_2
Temperature	1100°C
Pressure	5 MPa
Standoff distance	30 mm
Spray angle	90°
Nozzle dimensions	Convergent-divergent SiC-Out 1
Gun travel speed	500 m/s
$V_{\mathbf{imp}}$	709 m/s
η **(efficiency)**	1.59
Porosity	0.75%
Microhardness	390–400 Hv
Fatigue Strength	130 ± 6 MPa
Poisson's ratio	0.25
Density	7.9 g/cm^3

Table 3.2: Summary of process and material parameters for as-sprayed 316L stainless steel powder influencing deposition and bonding quality.

Given that the CSAM parameters from table 3.2 are implemented, the 316L deposit mechanical properties before and after heat-treatment are summarized in table 3.3. The as-sprayed deposit is not isotropic, therefore the fracture toughness values differ in each direction. After annealing, the material becomes isotropic and the fracture toughness is constant in both directions. The plotted results from this study are displayed in figure 3.1b.

Material Property	**As-Sprayed**	**Annealed**
UTS	723 ± 33 MPa	696 ± 6 MPa
YS	687 ± 52 MPa	418 ± 3 MPa
Elongation	0.47 ± 0.02 %	49 ± 2 %
Young's modulus	173.9 ± 3 GPa	190 ± 10 GPa
Fracture toughness	$\approx 19.5 - 28MPa\sqrt{m}$	$\approx 18MPa\sqrt{m}$

Table 3.3: Material Property comparison of 316L Stainless Steel Deposit before and after heat-treatment

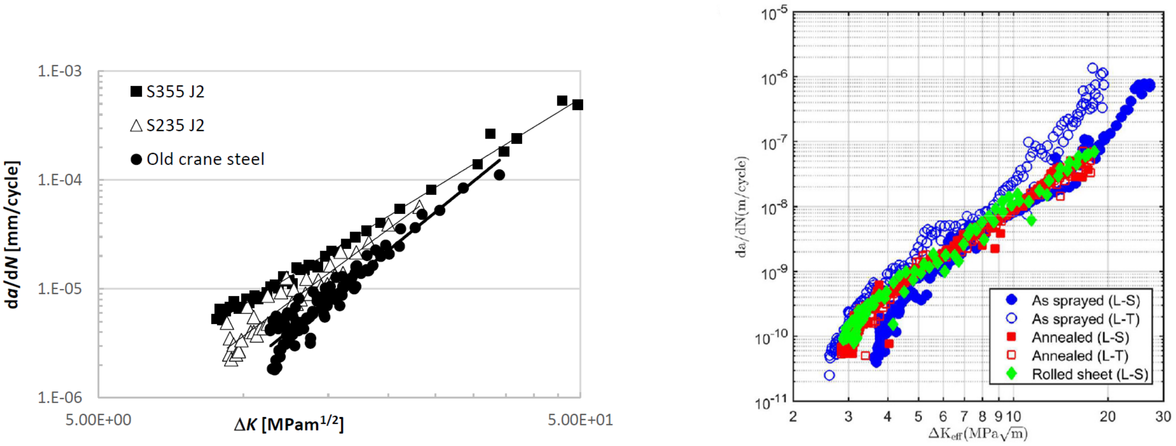

(a) Experimental results of fatigue testing for S235 [37].

(b) Experimental results of fatigue testing for all 316L deposits [25].

Figure 3.1: Fatigue testing results for S235 and 316L.

3.2.1 Discussion

As mentioned earlier in the chapter, the reason the 316L powder was selected for the deposit is because of limited experimental data on CSAM used for structural purposes. Utilizing an existing study that provided data for both tensile and fatigue performance was the best way to apply realistic results of CSAM behavior.

It is best to use material with a high fracture toughness when designing for fatigue, since it provides greater resistance to crack propagation [38]. When retrofitting fatigue cracks, applying a deposit material with higher fracture toughness than the base material may be more suitable. The annealed fracture toughness is lower than the S235 K_{IC} value, however the as-sprayed in the L-S direction deposit (defined in the paper [25]) shows significantly higher fracture toughness. This anisotropic behavior can be explored in a future study where annealing is skipped and as-sprayed deposit is utilized instead.

Chapter 4

Research Methodology

This thesis was inspired by EoL beams donated by Vic Obdam. Although the beams did not display the damage types selected in the research scope, other than bolts, they served as a valuable reference for real-life structural damages or imperfections in steel beams. Their exact dimensions were not utilized in the modeling process, but the site visit provided a broader understanding of various damage types. This research follows the following methodology, starting from a site visit and ending with a detailed analysis of a series of FEM models. These models consist of reclaimed and retrofitted steel structural elements. A figure visualizing the main methodology process is found in Figure 4.1.

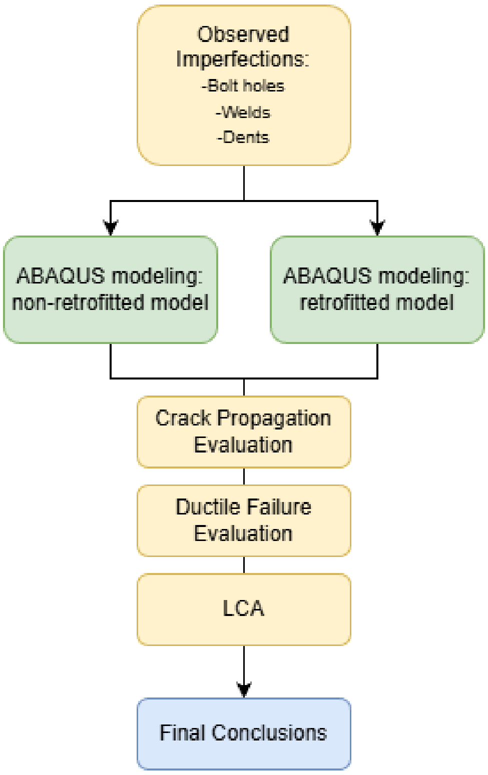

Figure 4.1: Methodology Overview

4.1 Finite Element Modeling

4.1.1 Tensile Coupons - Composite Material Behavior

The modeling was divided into several stages, the first one being a parametric study on a simple tensile coupon simulation in ABAQUS. The goal of this parametric study was to output the overall tensile strength and yield behavior between the deposit and substrate. Different cross-sections were explored, as well as different substrate materials, and also different retrofit geometries. The tensile coupons were dimensioned according to the ISO 6892-1 standard. The coupons consisted of a necked central section with a gross thickness of 3 mm, subdivided into substrate and deposit layers.

Variant A.1 compares the original S235 substrate to a stronger substrate material, S355. This is done to study the behavior of the two materials when they have comparable mechanical properties. Ideally, the strength of the deposit would be lowered to match that of S235 powder, but since that experimental research is not available at this time, a stronger base material was utilized instead.

Variant A.2 provides an upper and lower bound tensile capacity of the coupon variants to represent the range of tensile capacity of the coupons depending on the bonding properties. They will be utilized as guiding plots during future experiments to understand the bonding behavior of the deposit onto the substrate.

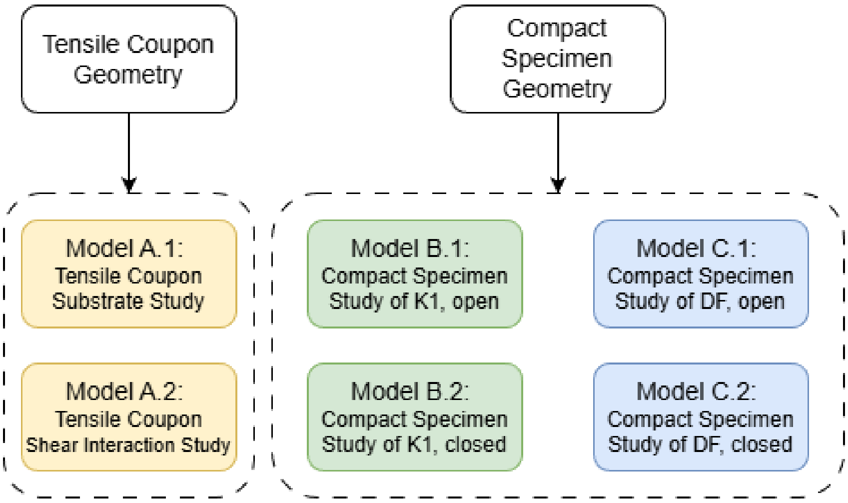

Figure 4.2: Compact Specimen model variants and desired outputs summary

4.1.2 Tensile Coupons - Parametric Study

Figure 4.3 displays the main model plus its purpose and desired outputs.

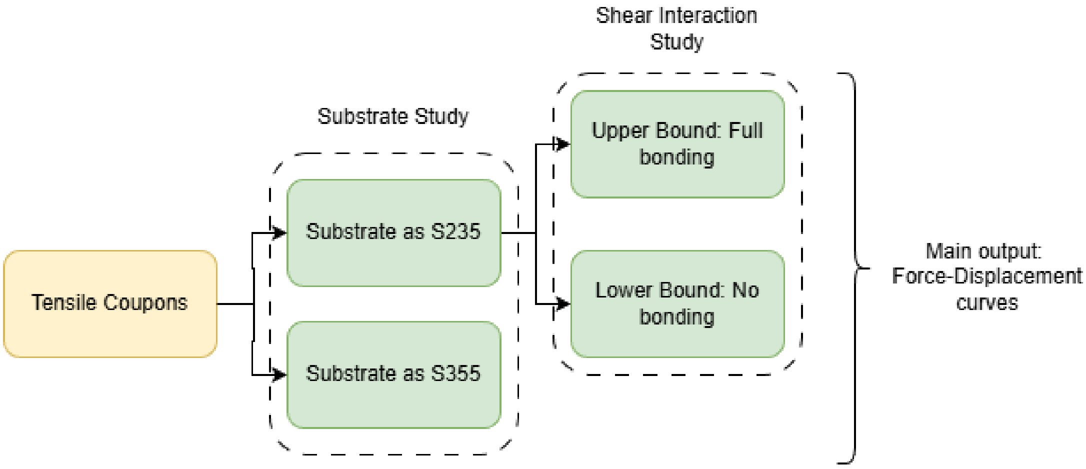

Figure 4.3: Modeling process of tensile coupons

4.1.3 Compact Specimen - Modeling Damages

The second stage of the modeling focuses on the behavior of a cracked specimen, specifically from a crack extending from a bolt hole. These damages were incorporated into the models to represent a riveted connection EoL steel element compatible with the research objective of the thesis.

Crack behavior is typically studied with a compact specimen, whose dimensions are set by the standards ASTM 1820 [39] and ASTM 647 [40].

Two model variations were created using the same compact specimen geometry:

- The "Open Notch Model," representing the non-retrofitted specimen
- The "Closed Notch Model," representing the retrofitted specimen

Based on these model variants, two main failure mechanisms were explored:

- Crack propagation from a bolt-hole-induced notch
- Debonding behavior at the deposit–substrate interface

The crack propagation behavior was explored for both the open and closed models. The closed model was explored further with the second failure mechanism, to determine whether the crack fast fracture or interface debonding governed during loading.

A flowchart documenting each sub-model and its desired outputs is showcased in Figure 4.4.

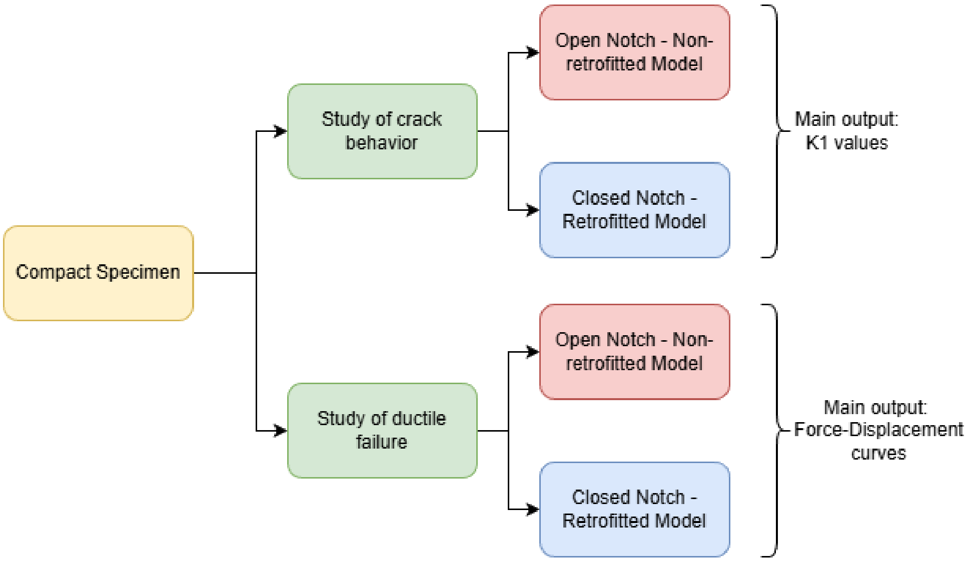

Figure 4.4: Compact Specimen model variants and desired outputs summary

The retrofitting process is modeled by applying 316L cold spray deposits onto existing cracked S235 geometries. The crack was embedded within the substrate, and the cold spray was deposited across the crack face to replicate the intended filling of the damage zone. The finite element model assumed that the WIP layer technique had been applied, ensuring full bonding between deposit and substrate.

The deposit is modeled as an elastic–plastic material, calibrated from tensile coupon results and aligned with the annealed experimental properties reported by Bagherifard [25]. The substrate is modeled as S235 low-carbon structural steel with its respective yield stress and elastic modulus.

4.2 Life Cycle Assessment (LCA)

A preliminary life cycle assessment (LCA) was conducted according to the ISO 14040/44. The goal of this was to contextualize the environmental impact of CSAM retrofitting compared to traditional repair strategies. The system boundary considered material inputs (316L feedstock powder, carrier gases, and energy consumption for spraying), as well as avoided impacts from replacing the entire steel element.

4.3 Research Assumptions

The finite element analysis and subsequent hand calculations were conducted under the following assumptions:

- The fatigue cracking location is at a floor-to-beam stringer connection.
- Rust is minimal and does not significantly affect the substrate's mechanical properties.
- Annealing heat treatment is possible at large-scale in-situ applications, with mechanical properties equivalent to those reported by Bagherifard [25].
- No residual stresses or internal forces are present in the steel elements due to prior fatigue or thermal loading.

- Crack dimensions are modeled according to representative values found in the literature.
- Cold spray data for S235 steel is not available, so 316L data from Bagherifard's experimental study [25] is utilized to study the disimilar material interaction of the deposit (316L) and substrate (S235).
- Bagheridard's study was the only extensive study showing experimental results for both the tensile and fatigue behavior of cold spray deposit used for structural purposes [25]. The same CSAM parameters and structural properties were thus utilized for this thesis.
- Full bonding is assumed between the deposit and substrate due to the use of the WIP layer technique.
- Deposit and substrate are modeled with "tie" interactions to represent full bonding between the two materials.

Chapter 5

FEA Models and Setup

To investigate steel bolt retrofitting with CSAM material and understand the interaction between the two materials, Finite Element Analysis was selected as the primary approach. Experimental data from Bagherifard [25] were utilized to define the CSAM material parameters in the models. When the necessary CSAM technology becomes available in the Netherlands, experimental testing can complement the modeling.

5.1 Model A: Tensile Coupons

5.1.1 Geometry

For the first-stage modeling, a simple tensile test was conducted on steel coupons of 3 mm thickness. The coupon dimensions were calculated according to the ISO 6892 standard [41]. The equations used can be seen below.

For proportional test pieces (other than cylindrical), the parallel length L_c shall be at least:

$$L_c \geq L_0 + 1.5\sqrt{S_0} \tag{5.1}$$

The original gauge length for proportional test pieces is defined as:

$$L_0 = k\sqrt{S_0} \tag{5.2}$$

where S_0 is the original cross-sectional area, and k is a constant.

$$k = 5.65 \quad \text{(standard value)}$$

$$k = 11.3 \quad \text{(alternative value)}$$

The original gauge length L_0 shall not be less than 15 mm. In the case that this limit fails, the alternative k value is used.

For parallel side test pieces with width less than 20 mm:

$$L_0 = 50\,\text{mm}$$

The free length between the grips shall be:

$$L_c = L_0 + 3b_0 \tag{5.3}$$

As for requirements for the gripped ends, they can be summaried as the following:

- Test pieces shall have gripped ends wider than the parallel length.

- The parallel length L_c shall be connected to the ends by means of transition curves.
- The radius of the transition curves shall be:
  - $0.75d_0$, where d_0 is the diameter of the parallel length, for cylindrical test pieces.
  - 12 mm for other test pieces.
- The width of the gripped ends shall be at least $1.2b_0$, where b_0 is the original width.

The final results of the dimensions are listed in Table 5.1 and visually displayed in Figure 5.1. The full calculations can be seen in Appendix A.

Parameter	**Value**
t	3 mm
$L_o^{\min}$	50 mm
$L_c^{\min}$	70 mm
b_o (per side)	24 mm
d_0	0

Table 5.1: Geometrical parameters of the specimen for Stage 1 model.

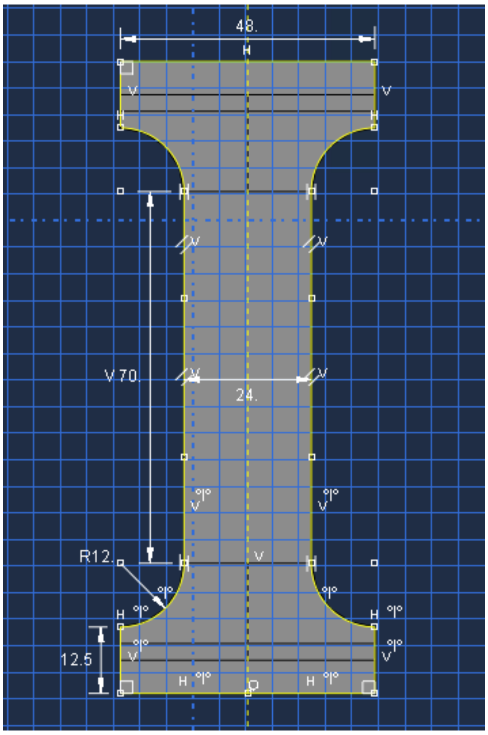

Figure 5.1: Final tensile coupon dimensions inserted into ABAQUS model.

5.1.2 Material Properties

The stress and strain properties of the 316L deposit were taken from the Bagherifard study [25]. The engineering values were provided by material coupon tensile tests, and they were converted to true stress and strain values using equations 5.4 and 5.5, respectively. These true values were input into ABAQUS. The equations for computing these values can be seen in equations 5.4 and 5.5. The final values are shown in both table format and plotted format in Table 5.2 and Figure 5.2.

$$\sigma_{\text{true}} = \sigma_{\text{engineering}} \left(1 + \varepsilon_{\text{engineering}}\right) \tag{5.4}$$

$$\varepsilon_{\text{true}} = \ln \left(1 + \varepsilon_{\text{engineering}}\right) \tag{5.5}$$

The original data found in the Bagherifard [25] study for the 316L steel deposit can be found in table 5.2, along with the true stress strain values. The same applies for the S235 material [42].

Material	σ [MPa]	ε	σ_t [MPa]	ε_t
316L powder [25]	418	0	418	0
	560	0.10	616	0.0953
	640	0.20	768	0.1823
	690	0.30	897	0.2624
	696	0.40	974.4	0.3365
S235 [42]	235	0	235	0
	260	0.01	262.6	0.00995
	345	0.05	362.25	0.04879
	370	0.15	425.5	0.13976
S355	355	0	355	0
	360	0.01	363.6	0.00995
	400	0.05	420	0.04879
	510	0.15	586.5	0.13976

Table 5.2: Engineering stress–strain and converted true stress–strain data for 316L powder and S235 steel.

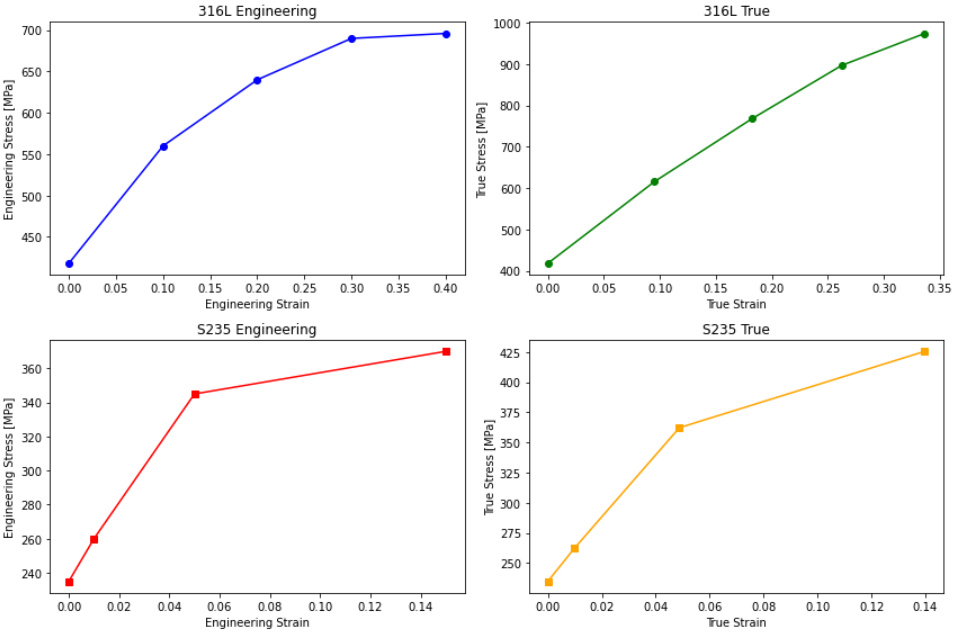

Figure 5.2: Plotted stress and strain values of both engineering and true values for materials S235 and 316L

5.1.3 Assembly and Interaction Properties

Retrofitted Specimen - Full Shear Interaction

The parts of the tensile coupons were assembled as dependent parts. Due to the lack of available experimental data regarding the interaction properties of the selected deposit parameters for 316L powder, full shear interaction was assumed between the ABAQUS modeling. The results of these models will act as an upper bound for the stress and strain experimental results. This upper bound represents a scenario where the deposit and annealing processes are executed perfectly. Three different geometries of retrofitted coupons were explored in the modeling, as seen in Figure 5.3. Each geometry had a different width of base versus retrofit material, which was categorized into percentages. These percentages represent the volume of the original coupon that was replaced by deposit material. In Figure 5.3, the substrate material is shown in green and the deposit in white. The listed dimensions in the figure correspond with 16%, 33%, and 50% volume of retrofitted material in the coupon, respectively.

Since full shear interaction was assumed to act between the deposit and substrate, the two parts were merged into one part. This was done under the Assembly tab when selecting Instances, Merge/Cut, and specifying the properties Merge, Suppress, and Retain. This process combines the instances in the assembly into one part, which is an alternative to placing tie constraints between all the part surfaces.

The deposit material was modeled to extend past the necked portion. Originally, it had been modeled as seen in Figure 5.4, however this meant that the weakest cross-section was at the top and bottom parts of the neck, where the retrofit material met the substrate material. While this may be the critical cross-section for the experiments, these results did not represent the combined strength of the two materials acting in shear interaction, which was the purpose of this study. This geometry layout was thus disregarded due to undesirable critical cross section location.

The top and bottom segments (12.5 mm of height for each) of the coupon grip were modeled as rigid bodies, as it is expected that those areas will be clamped during experimental testing. Those areas were thus excluded from the model outputs. Each rigid body corresponded to its own reference point, each at the center of the top and bottom surface. These reference points are important for applying boundary conditions and postprocessing results, which is discussed later.

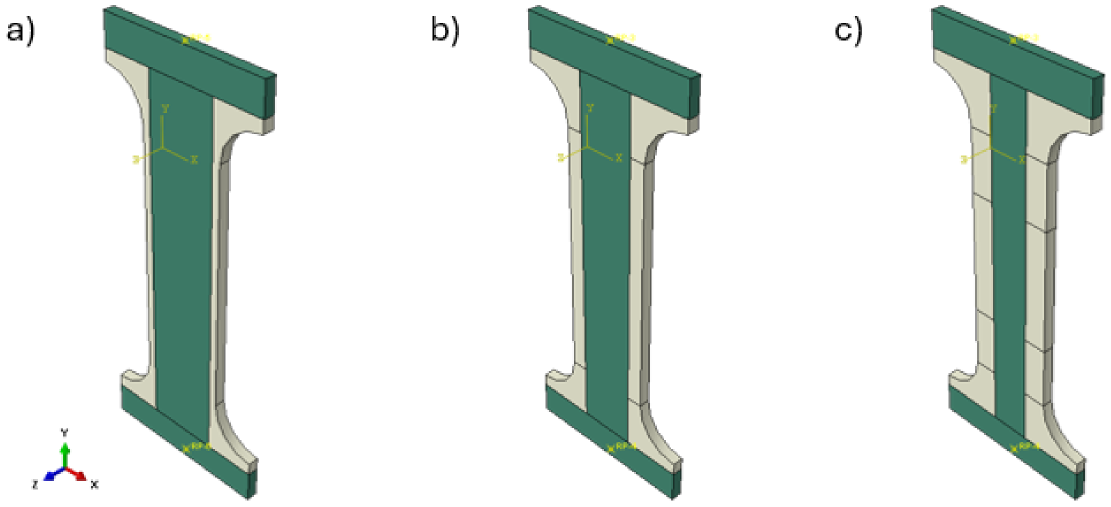

Figure 5.3: All Variants of retrofitted coupons modeled with full shear interaction properties, representing the following dimensions: a) S235: 19.7 mm & 316L: 2.15 mm/side, b) S235: 15.5 mm & 316L: 4.25 mm/side, c) S235: 11 mm & 316L: 6.5 mm/side.

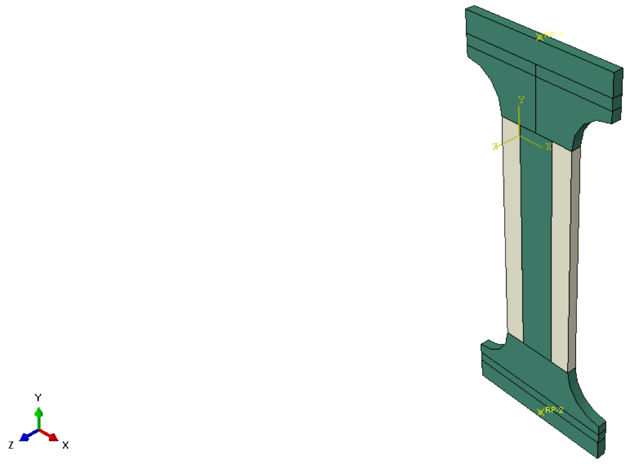

Figure 5.4: Original geometry of a retrofitted coupon, more closely resembling the geometry that will be utilized during experimental testing.

Retrofitted Specimen - Only Base Material

One of the possible outcomes of this retrofitting process is that weak bonding between the deposit and substrate occurs. This could be due to several factors, such as inadequate impact velocity, incompatible hardness between the two materials, or inability to perform

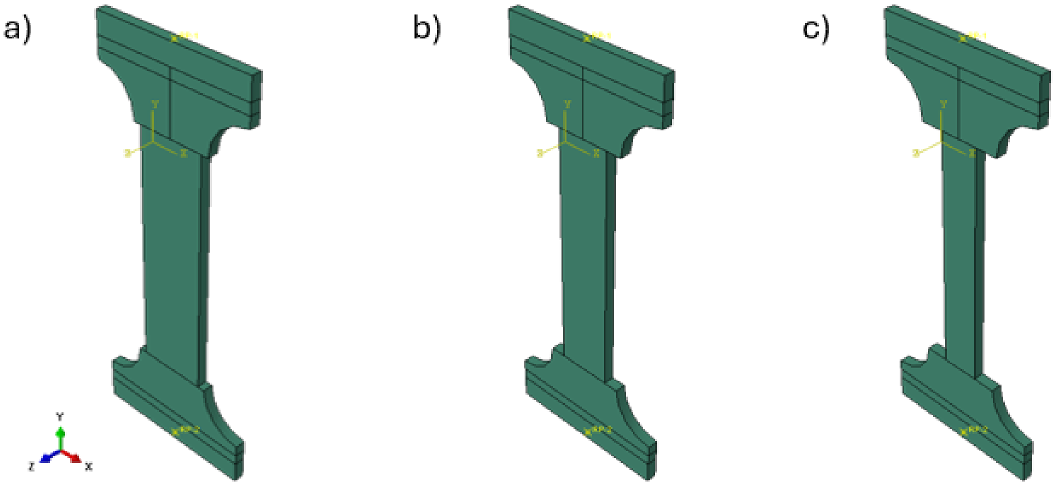

Figure 5.5: All Variants of retrofitted coupons modeled with no shear interaction properties, representing the following dimensions: a) S235: 19.7 mm & 316L: NA, b) S235: 15.5 mm & 316L: NA, c) S235: 11 mm & 316L: NA

heat treatment. In the case that the bonding fails are the preliminary loading of the samples, two variants of the tensile coupons were modeled. Three different geometries of retrofitted coupons were explored in the modeling, as seen in Figure 5.5. These geometries correspond with the geometries seen in 5.3, however the deposit material was removed to represent no shear interaction.

Similar to the upper-bound model, the top and bottom sections of the grip (12.5 mm height) were modeled as rigid bodies and excluded from the final outputs.

5.1.4 Step and Outputs

Non-linear geometry was turned on for this model, since the plastic behavior of both materials was the main focus of the study. The desired outputs were the vertical displacement, U2, and the reaction force, R2, both from the top reference point.

5.1.5 Loading and Boundary Conditions

For the first stage of the modelling, a 20 mm displacement was applied onto the top of the steel coupons, more specifically to a reference point coupled to the top surface. This was done so the load would be applied onto the center of the coupon and distributed evenly among the material. The bottom of the plate was constrained in all degrees of freedom.

5.1.6 Meshing and Job

A sensitivity analysis for different mesh sizes was conducted to determine the acceptable mesh sizes. A mesh of size 1 mm was selected for both the deposit and substrate material. The types of mesh selected were a hex sweep mesh and a hex structural mesh for the deposit and substrate, respectively.

5.2 Model B: Compact Specimen - K1 study

5.2.1 Geometry

Specimen Dimensional Requirements

Compact specimen dimensions are set by the standards ASTM 1820 [39] and ASTM 647 [40]. The same width as the tensile coupons, 24 mm, was taken as the baseline for dimensioning. The full numerical calculations can be found in Appendix B.

All specimen dimensions are expressed as fractions of the specimen width W. Dimensional tolerances shall be within $\pm 0.013\,W$. The crack-starter notch shall be centered between the top and bottom specimen edges within $0.005\,W$.

The main specimen dimensions are defined in Table 5.3, as seen from Figure 5.6 [39].

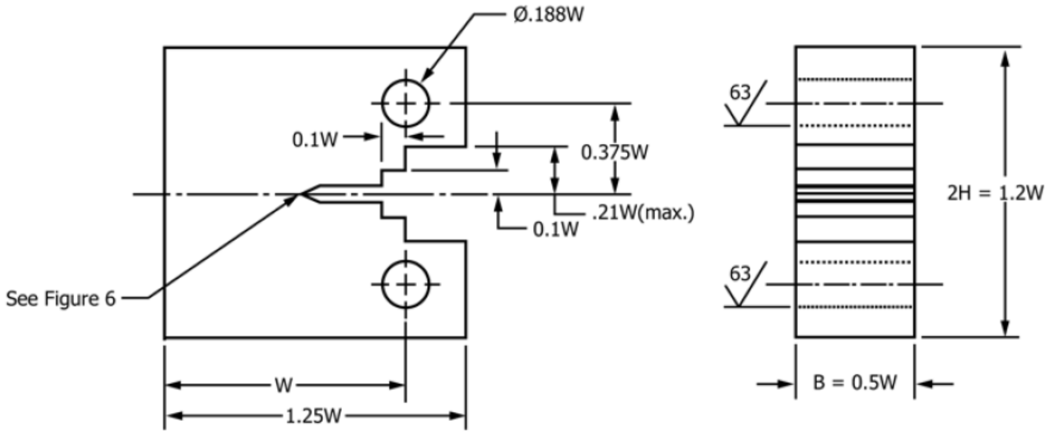

Notes:
1. Tolerance on all dimensions ±0.013W
2. Pin shall be sized so that maximum clearance with hole is 0.01W

Figure 5.6: Compact specimen dimension requirements, as per the ASTM E1820.

Parameter	Symbol	Expression	Value (mm)
Distance to load	W	W	19.20
Hole diameter	d	$0.188\,W$	3.61
Base width	b_{base}	$1.25\,W$	24.00
Specimen height	H	$1.20\,W$	23.04
Specimen thickness	B	$0.50\,W$	9.60

Table 5.3: Main specimen dimension relationships and resulting values for $W = 19.2$ mm (calculated from $1.25W = 24$).

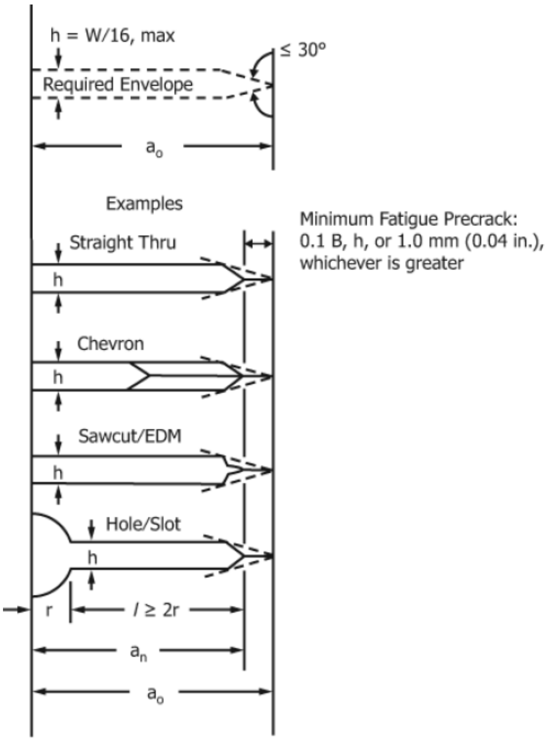

Figure 5.7: Radial notch dimension requirements, as per ASTM E647.

Notch Geometry and Precrack Requirements

B.1 Model: Open Notch - Non retrofitted

According to Figure 5.7, which is taken from the ASTM E647 [40], there are several various types of notch dimension limits. The last one in the figure displays a notch stemming from a radius, which was selected for this thesis due to its geometry resembling that of a cracked bolt hole. The corresponding dimensioning requirements and results are listed below in Table 5.4 [40]. The notch sharpened edge, a_s, was calculated through trigonometric functions according to the limits seen in Figure 5.7. The final dimensions input into the model are displayed in the ABAQUS model in Figure 5.8.

Parameter	**Symbol**	**Expression**	**Value (mm)**
Notch radius	r	set by user	2.50
Notch max height	h	$\leq \frac{W}{16}$	1.20
Notch length	L	$\geq 2\,r$	5.00
Sharpened notch	a_s	$\frac{h/2}{\tan(45^\circ)}$	0.60
Minimum precrack extension	a_p	$\geq \max(0.1\,B,\ h,\ 1)$	1.20
Total notch length	a_n	$r + L + a_s$	8.10
Total notch + precrack length	a_0	$a_n + a_p$	9.30

Table 5.4: Notch and precrack dimensional requirements and resulting geometrical parameters for the compact specimen according to ASTM E647.

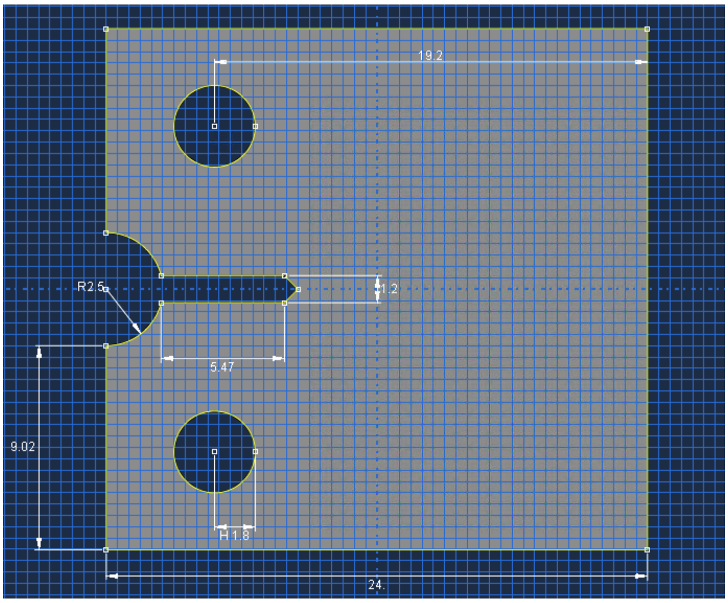

Figure 5.8: Final compact specimen dimensions utilized for the ABAQUS model.

B.2 Model: Closed Notch - Retrofitted

The same dimensioning standards apply for the retrofitted model, however when looking at crack propagation, the notch was flattened into a square. This was done so that the output from the crack tip that is located at the interface of the two materials will equally account for each material across all its contour lines, which are displayed in Figure 5.10. This adjustment was only applied to the study of stress intensity values. The ductile-failure study was completed using the original geometry.

5.2.2 Material Properties

The study of stress intensity values $K1$ is only valid under Linear Elastic Fracture Mechanics (LEFM) assumptions, thus the plastic behavior of the steel material is neglected [19]. Only the elastic properties listed in table 5.2 were input in this model.

5.2.3 Assembly and Interaction Properties

B.1 Model: Open Notch - Non retrofitted

For compact specimen, crack behavior is studied, specifically the loading point at which the crack will propagate. First, the original notched specimen was studied, acting as a control point for analyzing the behavior of the retrofitted model.

The compact specimen parts were inserted as independent parts. For both models, the bolt holes were modeled as rigid bodies and coupled to two reference points, one at each hole center. These reference points can be seen in orange in Figure 5.9. These reference points played a role in defining boundary conditions and postprocessing results, which will be discussed in later sections.

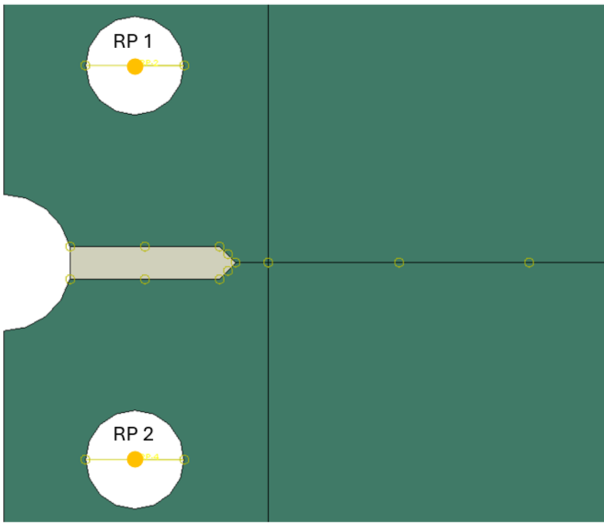

Figure 5.9: Ties between the elements used to assemble the final model, depicted by yellow circles.

Under the "Special" settings of the Interaction properties tab, a seam was added to represent a lack of connectivity in the material, defined through a surface selection. This surface represents the fatigue pre-cracking and is typically used to initiate cracking propagation. Since the seam is an infinitely small thickness, it leads to a stress singularity at the edge, especially in FEM modeling. It is important to take it into account for more precise stress and strain calculations [43]. Figure 5.10a showcases the crack locations, the mesh partitions and contour lines surrounding the crack, and the crack propagation directions. The image on the far left shows the open model where the notch remains sharp and no retrofitting is applied. The middle image shows the retrofitted model with the flattened notch spanning throughout all the contour lines of the second crack. The far right image shows the specified settings to account for the singularity at each crack. The crack seam is showcased in bold, and the crack tip as the green x symbol. The crack propagation direction is shown in pink and the contour lines and element partitions in orange.

B.2 Model: Closed Notch - Retrofitted

The retrofitted model had 316L material fill the entire notch dimensions except for the radius in the beginning and the fatigue pre-cracking at the end. An important distinction between this and the open model is the notch edge. It was flattened, thus the first ring surrounding the second crack consisted of equal parts deposit and substrate material. This was done to better capture the effect the retrofit material has on the stress intensity factors. The flattened edge of the notch spanned the entire first contour line, and both the seam and notch lengths remained the same. The deposit was bonded around its perimeter to the substrate with a tie constraint to represent full shear interaction. A zoom in of the notch geometry and crack properties can be seen in 5.10b. It showcases the contour and partition lines in orange, the final mesh and seam in black, the crack location in green and the propagation direction in pink. The singularity properties that were defined for each crack are shown in Figure 5.11.

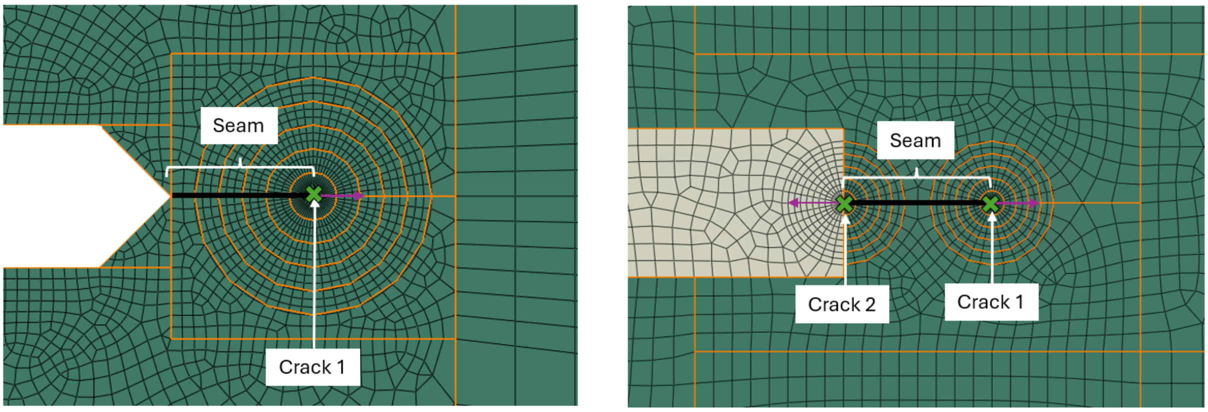

(a) Open Model (b) Closed Model

Figure 5.10: Zoom-in of the notch edge for each model, displaying the crack location and propagation direction, contour lines, and meshing.

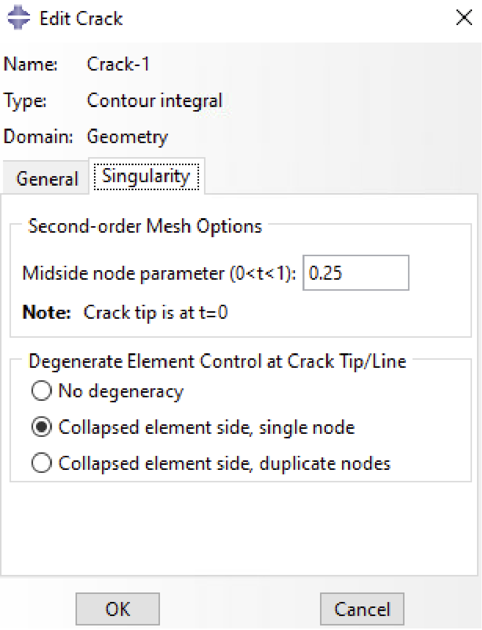
Edit Crack

Name: Crack-1

Type: Contour integral

Domain: Geometry

Second-order Mesh Options

Midside node parameter (0<t<1): 0.25

Note: Crack tip is at t=0

Degenerate Element Control at Crack Tip/Line

○ No degeneracy

● Collapsed element side, single node

○ Collapsed element side, duplicate nodes

Figure 5.11: Settings defined for each crack due to the singularity that forms at the seam tip.

5.2.4 Loading and Boundary Conditions

The bottom reference point was constrained in all degrees of freedom except for U2, the vertical displacement, and UR3, the rotation around the z-axis. The top reference point had a displacement applied at U2 and the UR3 unconstrained.

A vertical displacement of 0.1 mm was applied at the top reference point for the non-retrofitted part. The reason for this was so that the same displacement could be applied to the retrofitted models, which is preferable for comparing the outputs of both models. Preliminary hand calculations to predict an estimated required minimum displacement to exceed the K_{IC} value can be seen in Appendix D.

5.2.5 Meshing and Job

As mentioned previously, a singularity occurs at the edge of the crack seam, which must be accounted for in the model to ensure accurate results. One way to account for this singularity is through proper meshing. This is achieved through contour lines, as seen in Figures 5.10a and 5.10b for the non-retrofitted and retrofitted models, respectively. These allow for a refined structural mesh. The ideal mesh around the crack resembles a "spider-web" shape, radiating from the center of the circle. The inner-most contour line has triangular meshing, while the outer contours consist of quadratic quadrilateral elements [43]. The triangular meshing occurs due to the elements being collapsed, meaning that an edge collapses into a single node, thus becoming a triangle. This does not mean that the nodes are deleted. Instead, they share the same coordinates, and are treated as separate nodes. This meshing is necessary for crack-tip nodes to converge smoothly without geometric distortion. To accomplish this, second-order elements are utilized when defining the crack, with the settings seen in Figure 5.11. The midside node parameter is changed to 0.25 from 0.5 so it is placed closer to the crack tip, which allows the element shape functions to replicate the analytical crack-tip field better, a common trick in fracture mechanics [43].

Five contour lines were defined surrounding the crack to allow for sufficient data to ensure convergence of results. The contour lines were spaced at 0.2 mm distance, each partitioned into 16 - 20 seeds along the perimeter to allow for appropriate meshing. The sections around the notch geometry and crack geometry were assigned a mesh size between 0.1 and 0.2 mm, varying depending on the seed amount, with the remaining model having a coarser mesh size of 0.5 mm. These values were selected based on a sensitivity analysis exploring various mesh sizes around the critical failure points. A square mesh is preferable, thus a quad-dominant mesh was selected for the notch geometry and rectangle partition surrounding the crack geometries. The contour lines were assigned a quad-dominant sweep mesh to achieve the desired spider-web mesh shape. The remaining model was assigned a quad-dominant structured mesh.

5.3 Model C: Compact Specimen - Ductile Failure study

The same process as for model B was followed, except for the following ABAQUS steps:

5.3.1 Material Properties

Ductile damage criteria, in addition to the elastic and plastic properties from table 5.2, was defined for this model. The goal is to observe the failure evolution at the interface between the two materials, and determine whether the debonding or the crack fast-fracture failure mechanisms govern for the retrofitted model.

Tables 5.5a and 5.5b display the defined failure parameters for both substrate and deposit materials, respectively. The displacement at failure is dependent on the mesh size, the equation of which is shown in equation 5.6 [44].

$$u_f = L_c \cdot \varepsilon_f \tag{5.6}$$

With a mesh size of 0.2 mm, the finest mesh in each material was selected, and the height and width were taken. For the retrofitted model, each material was calculated seperately depending on the respective fracture strain and mesh size. For the non-retrofitted material, the following calculations were completed to compute fracture strain:

S235:

$$\begin{aligned}
H &= 1.54 \times 10^{-1} \text{ mm}, \\
W &= 1.12 \times 10^{-1} \text{ mm}, \\
L_c &= \sqrt{HW} = 1.31 \times 10^{-1} \text{ mm} \\
\varepsilon_{S235} &= 0.22 \\
u_f &= \varepsilon_{S235} L_c = 0.22 \cdot 1.31 \times 10^{-1} = 2.89 \times 10^{-2}
\end{aligned}$$

Triaxiality was taken as 0.33 for all models due to the uniaxial load applied onto the specimen. This value was computed with the following process [44]:

$$\eta = \frac{\sigma_p}{\sigma_v} \tag{5.7}$$

$$\sigma_p = \frac{\sigma_{11} + \sigma_{22} + \sigma_{33}}{3} \tag{5.8}$$

$$\sigma_v = \sqrt{\frac{1}{2}\left[(\sigma_{11} - \sigma_{22})^2 + (\sigma_{22} - \sigma_{33})^2 + (\sigma_{33} - \sigma_{11})^2 + 6(\sigma_{23}^2 + \sigma_{31}^2 + \sigma_{12}^2)\right]} \tag{5.9}$$

Under uniaxial loading, two out of the three stresses in equation 5.8 are equal to zero. We thus get the following:

$$\sigma_p = \frac{\sigma_{11} + 0 + 0}{3} \tag{5.10}$$

$$\sigma_v = \sqrt{\sigma_{11}^2} \tag{5.11}$$

$$\eta = \frac{\sigma_{11}/3}{\sqrt{\sigma_{11}^2}} = 0.33 \tag{5.12}$$

For the retrofit material, the following calculations were done to find ε_f:

316L:

$$\begin{aligned}
H &= 7.99 \times 10^{-2} \text{ mm} \\
W &= 2.00 \times 10^{-1} \text{ mm} \\
L_c &= \sqrt{HW} = 1.26 \times 10^{-1} \text{ mm} \\
\varepsilon_{316L} &= 0.48 \\
u_f &= \varepsilon_{316L} L_c = 0.48 \cdot 1.26 \times 10^{-1} = 6.07 \times 10^{-2}
\end{aligned}$$

For the substrate material, ε_f remained the same as before. This process was repeated each time a different mesh was applied, for example in the mesh sensitivity analysis.

S235 Material	**Value**
Ductile Damage	
Fracture Strain	0.22 [37]
Stress Triaxiality	0.33
Strain Rate	0
Damage Evolution	
Type	Displacement
Softening	Linear
Displacement at Failure	0.0289

(a) S235

316L Material	**Value**
Ductile Damage	
Fracture Strain	0.48 [25]
Stress Triaxiality	0.33
Strain Rate	0
Damage Evolution	
Type	Displacement
Softening	Linear
Displacement at Failure	0.0607

(b) 316L

Table 5.5: Ductile Failure properties and damage criteria specified in the material properties of S235 and 316L.

5.3.2 Assembly and Interaction Properties

For the interface bonding behavior, since ductile damage parameters are included, the explicit solver is used. For the explicit solver, the seam geometry is incompatible and thus removed. Instead, the compact specimen geometry was split in half and tied in the middle, leaving a length of 1.2 mm untied to represent the crack. A visual of this model setup is shown in Figure 5.12. The tie constraints can be seen in figure 5.9. An additional constraint for this model was that the bolt holes at the top and bottom were modeled as rigid bodies before any loading was applied, to resemble the behavior as if a bolt is present in the hole.

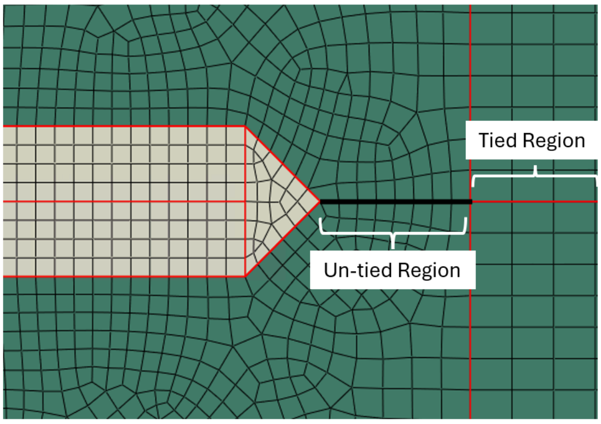

Figure 5.12: Zoom-in of the notch edge for the debonding study, utilizing a different modeling approach of the crack geometry that is compatible with dynamic explicit.

5.3.3 Step and Outputs

For the ductile-failure study along the interface of the two materials, NLgeom was turned on again, as plastic deformation and material failure play a significant part in the results. The dynamic explicit solver was selected for the ductile damage outputs. Mass scaling was applied to reduce the computation time of the simulation, which required the calculation of the stable time increment, as seen in equation 5.13 [45]. This variable is the quotient of the characteristic element length and the element wave speed. The finest mesh element should be used for this characteristic length.

$$\Delta t = \frac{L_e}{\sqrt{E/\rho}} \tag{5.13}$$

A mesh size of 0.2 mm was utilized for the following calculation.

$$\Delta t = \frac{9.97E - 02}{\sqrt{210000 \cdot 8e^{-9}}}$$

$$\Delta t = 2.05e^{-08}\ seconds$$

When applying mass scaling, the whole model was scaled to target a time increment of $2.05e^{-06}$ in order to reduce computation time. When utilizing a value of $2.05e^{-08}$, or even $2.05e^{-07}$ the computation time for the model was over 24 hours. When comparing the results from a scaled model of e^{-07} versus e^{-06}, the results were sufficiently similar, thus the stable time increment was increased by two decimal points for all simulations.

5.3.4 Loading and Boundary Conditions

The bottom reference point was constrained in all degrees of freedom except for U2, the vertical displacement, and UR3, the rotation around the z-axis. The top reference point had a displacement applied at U2 and the UR3 unconstrained. The locations of the reference points are labeled by orange circles in figure 5.9.

For the model representing the ductile failure around the interface, a higher displacement was applied. After exploring simulations under different displacements, it was found that 1 mm was sufficient to induce full failure at the interface. Thus 1 mm was applied at the top reference point, allowing for rotation about the z-axis for both top and bottom points. An amplitude of increments 0.25 ranging from 0 to 1 was applied for smoother results.

5.3.5 Meshing and Job

The contour lines around the crack tips were removed, and a finer 0.2 mm mesh was focused at the interface between the deposit and substrate material, which was the primary region of interest. The remaining model was meshed at 0.5 mm. The element types in this area are quads to avoid mesh irregularities. It is important to keep a consistent mesh due to the mass scaling and damage evolution criteria that is applied to this simulation. Element deletion was activated with a max degradation of 0.95.

Chapter 6

FEA Results and Post-Processing

6.1 Model A: Tensile Coupons - Behavior and Analysis

A parametric study was performed on a tensile coupon element with varying widths of the deposit and substrate, where their gross width remained at 24 mm. The different deposit to substrate ratios, classified as percentages of the total deposit volume composing the coupon volume, are shown in figure 6.1

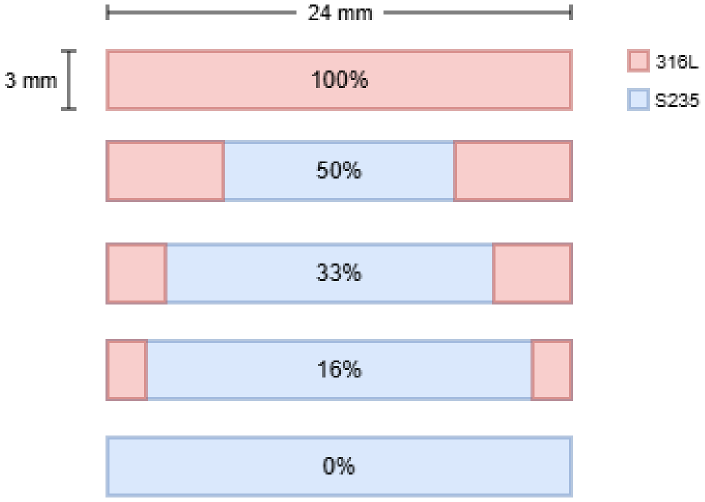

Figure 6.1: Different cross sections considered in the parametric study, where different percentages of the overal coupon volume were replaced by deposit material 316L.

First, two different orientations were modeled, one with the retrofit material along the thickness, and one along the width of the coupon. The orientation along the width of the coupon was selected due to its symmetrical layout. This geometry avoids eccentricity in the coupon, thus simplifying the analysis. The models and results for both orientations are shown in Appendix C.1. In the next step, a comparison between two different substrate materials, S235 and S355, was done. The substrate S235 was selected as the final model to perform two simulations, one with full shear interaction, and one with none. The final results will be utilized in future experimental studies to determine the bonding behavior between the deposit and substrate.

6.1.1 A.1: Base Material Comparison

The two models are referred to as the following in this section for simplicity:

- Model A - S235/316L
- Model B - S355/316L

The coupons were run using ductile failure criteria under the explicit solver to compare damage evolution and assess how localized failure in each material influences the overall tensile capacity. The resulting curves are presented in Figures 6.2 and 6.3, with the corresponding yield and peak load values listed in Tables 6.1 and 6.2. These values are plotted in Figure 6.4, which illustrates the relationship between retrofit percentage and the force-displacement values at peak load.

Retrofit (%)	Stage	U2 (mm)	P (N)
0	Yield	0.50	17805
	Peak Load	10.5	26481.9
16	Yield	0.50	20105.2
	Peak Load	11.5	29366.7
33	Yield	0.50	22665
	Peak Load	12.5	32530
50	Yield	0.50	24797.3
	Peak Load	15.5	36575

Table 6.1: Yield and Peak Load values for Model A at different retrofit percentages.

Retrofit (%)	Stage	U2 (mm)	P (N)
0	Yield	0.50	25867
	Peak Load	12.5	36552.1
16	Yield	0.50	26719.6
	Peak Load	12.5	37595.2
33	Yield	0.50	27654.3
	Peak Load	13.5	38876.6
50	Yield	0.50	28504.7
	Peak Load	15.5	40918.8

Table 6.2: Yield and Peak Load values for Model A at different retrofit percentages.

Effect of retrofit percentage on coupon ductility and strength

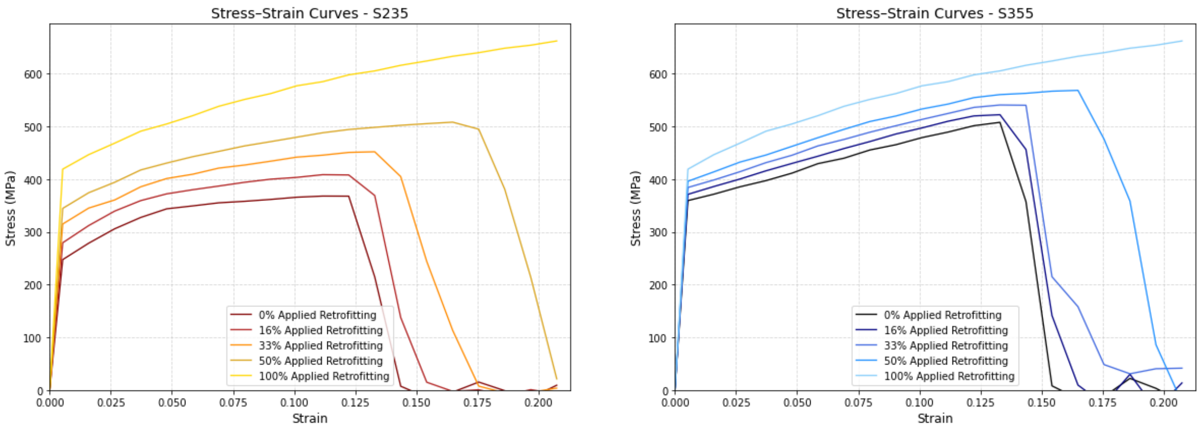

(a) Substrate S235.

(b) Substrate S355.

Figure 6.2: Model A and B stress-strain curves under different retrofitting dimensions

S355 steel resembles the yield stress and strain of the 316L deposit. When utilized as the substrate, the yield parameters between the composite variations are more consistent than those from the S235 substrate, since the yield stresses of the two are 63 MPa apart. The increase in force and displacement at the peak load between each retrofit variant for models A and B are shown in tables 6.3 and 6.4, respectively.

The numbers in table 6.4 demonstrate that since the S355 variant has a yield strength closer to that of the 316L deposit, the difference of capacity between each iteration is less significant for the load capacity values, the max increase being 5.3% from variants 33% to 50%. Ductility shows greater increase, increasing by a maximum of 14.8% between the same variants. This shows how the deposit percentage will influence the capacity of the axial load and the ductility. Since the deposit displays significant ductile behavior, the influence on the ductility is greater than the influence on the load.

The same applies for model A, however since S235 is significantly weaker than 316L, the increase between each retrofit variant is greater for both load capacity and ductility. Between variants 33% and 50%, the load capacity and ductility increase by 12.4% and 24 %, respectively. Thus it can be concluded that the deposit has a greater impact on model A's structural response due to the greater mismatch in mechanical properties of the two materials.

The stress-strain curves are plotted in figure 6.2, with model A on the left and model B on the right. The ABAQUS simulation results are documented in figure C.3.

% Retrofit	U2 (mm)	ΔU2 (%)	P (N)	ΔP (%)
0%	10.5	–	26481.9	–
16%	11.5	+9.5%	29366.7	+10.9%
33%	12.5	+8.7%	32530.0	+10.8%
50%	15.5	+24.0%	36575.0	+12.4%

Table 6.3: Displacement at peak load and peak load for S235 with relative differences between each variant. Represents influence on deposit on results.

% Retrofit	U2 (mm)	ΔU2 (%)	P (N)	ΔP (%)
0%	12.5	–	36552.1	–
16%	12.5	+0.0%	37595.2	+2.9%
33%	13.5	+8.0%	38876.6	+3.4%
50%	15.5	+14.8%	40918.8	+5.3%

Table 6.4: Displacement at peak load and peak load for S355 with relative differences between each variant. Represents influence on deposit on results.

Effect of substrate strength on coupon ductility and strength

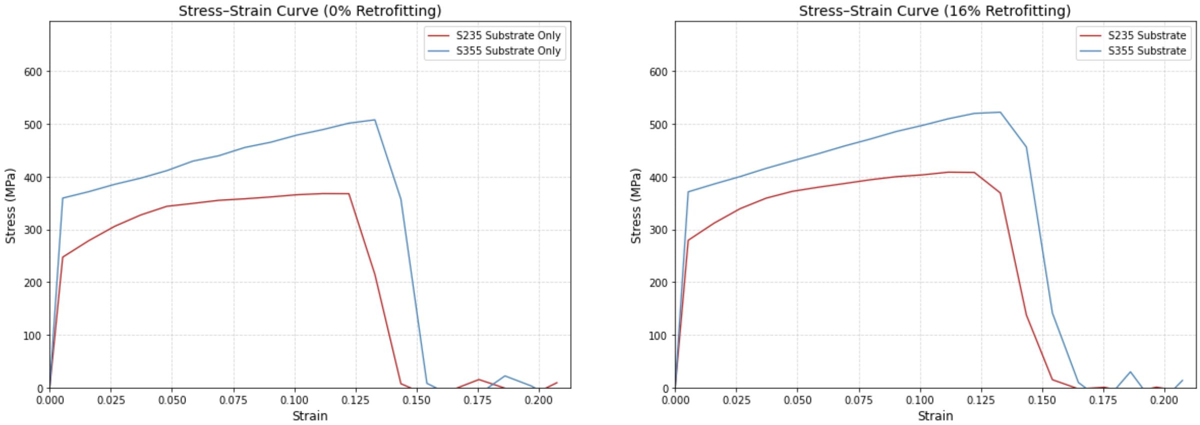

(a) 0% retrofitting (Substrate only)

(b) 16% retrofitting

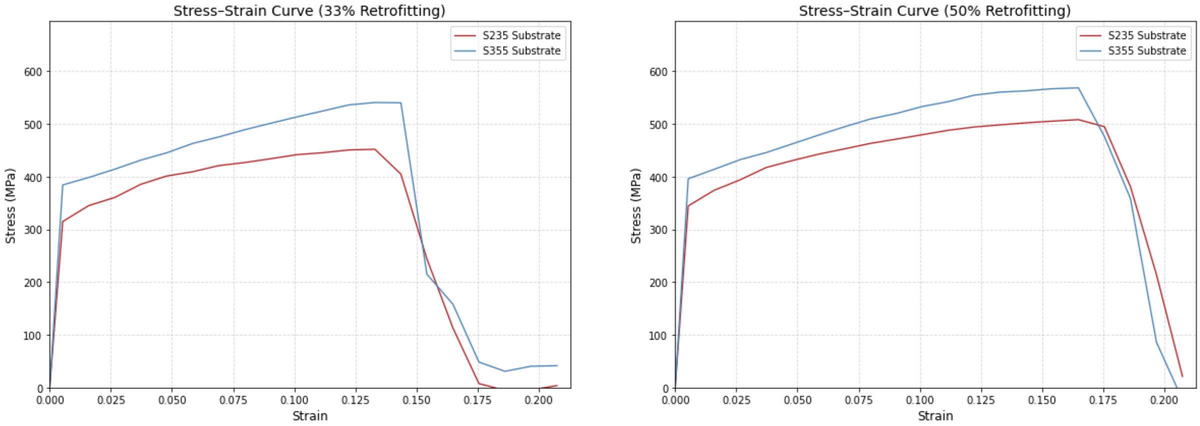

(c) 33% retrofitting

(d) 50% retrofitting

Figure 6.3: Comparison of substrates S235 and S355 with 0%, 16%, 33%, and 50% of retrofitting.

Figure 6.3 compares the stress–strain behaviour of models A and B, grouped by retrofitting percentage. As discussed previously, model B exhibits a higher tensile capacity than model A for all variants, however the overall shape of the stress–strain curves remains similar between the two models at each retrofitting level. This similarity is expected, as identical damage evolution parameters were assigned to the S235 and S355 substrates, isolating the influence of substrate yield strength on damage initiation and evolution.

% Retrofit	ΔU2 (S355–S235)	ΔP (S355–S235)
0%	+19.0%	+27.6%
16%	+8.7%	+21.9%
33%	+8.0%	+16.3%
50%	+0.0%	+10.6%

Table 6.5: Relative difference S355 vs. S235 at each retrofit level. Represents influence of substrate on results.

Despite the identical damage parameters, the 0% retrofitting case shows a 19% increase in ductility when comparing the S355 substrate to S235, demonstrating that the higher strength of S355 directly increases its ductility and delays damage initiation, regardless of deposited material.

When combined with the 316L deposit, the ductility between models A and B increases for the 16% and 33% variants. For these coupons, damage initiation is delayed by up to 1 mm for the S355 substrate, corresponding to ductility increases of 8.6% and 8.0%, respectively, as summarized in Table 6.5. This reduced relative increase occurs because the contribution of the deposit material begins to govern the deformation response, reducing the influence of the substrate.

As the percentage of retrofitting increases, the mechanical response of the coupon gradually becomes less dependent on the substrate material. At the 50% retrofitting level, the substrate fails first, after which the deposited material governs the fracture process. This transition is confirmed in Figure C.3 (Appendix C). As a result, damage initiation occurs at the same displacement value (U2 = 15.5 mm) for both models A and B, as shown in Figure 6.4b. This explains why the relative ductility difference between the substrates converges to 0% for the 50% variant.

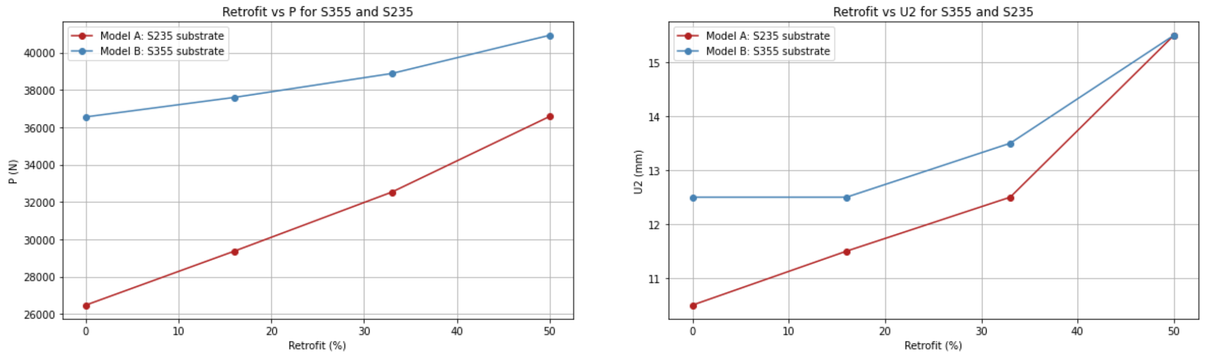

(a) Applied external force (P) at which ductile damage initiation occurs for two different substrate materials, evaluated at four retrofit percentages.

(b) Model displacement (U2) at which ductile damage initiation occurs for two different substrate materials, evaluated at four retrofit percentages.

Figure 6.4: Sensitivity analysis plots for different deposit-to-substrate widths.

Although ductility converges at higher retrofitting levels, differences in axial load capacity persist. At 0% retrofitting, S355 exhibits a 27.6% higher peak load than S235. This difference decreases with increasing deposit percentage because the deposited material substantially enhances the strength of model A, while providing a comparatively smaller incremental benefit to model B. Nevertheless, even at 50% retrofitting, model B is able to sustain 11.9% more axial load than model A despite identical fracture displacements, showing that the stronger substrate continues to improve load-carrying capacity.

In summary, both substrate strength and deposited material significantly influence the ductility and damage initiation behaviour of the composite coupon. The heat-treated 316L deposit exhibits high ductility, and increasing deposit volume increases deformation capacity regardless of substrate type. However, as the cross-section becomes deposit dominated, the influence of substrate strength on ductility diminishes and eventually vanishes. In contrast, substrate strength continues to affect axial load capacity even when fracture displacement is governed by the deposit. These results highlight the distinct and competing roles of substrate and deposited material in controlling ductility and strength.

Interpretation of results and modelling assumptions

In these coupon simulations, the deposited layer is oriented so that the interface is parallel to the applied load. As a result, the cross-section of the neck in the coupon is consistent throughout the entire gauge length. This geometry prevents a weakened cross-section from forming at the interface between the two materials, in contrast to model C.2 (the retrofitted C(T) case). Consequently, even a large mismatch in tensile strength between the deposit and substrate does not induce early failure through debonding. Therefore these results suggest that matching the substrate and deposit material properties will not prevent debonding at the interface. This interpretation relies on the assumptions that there is full shear interaction across the interface and that the critical section is not located within a heat-affected region (HAZ). Although these considerations lie beyond the scope of the present study, they could limit the applicability of this configuration in practice.

To conclude, these models show that matching the tensile yield strengths of the deposit and substrate does not provide any benefits when the deposit is applied parallel to the interface. It will not prevent debonding from taking place, as it does not create a weak point in the cross-section. Debonding is still possible if partial shear interaction or HAZ regions are considered, however those are outside of the scope of this thesis. For this orientation, increasing the substrate yield strength will simply increase the coupon's tensile capacity and fracture strain.

6.1.2 A.2 Upper and Lower Bound Comparison

The substrate material S235 was selected to continue onto the next modeling stage. The reason for this is due to the S235 material being more commonly used in riveted steel bridges, as mentioned in the literature [36]. Due to lack of experimental data and available resources, no bonding properties are available to describe and model the interaction between the 316L deposit and the S235 substrate. Therefore the same coupons as before were modeled with full shear interaction and no shear interaction, described as Upper and Lower bound results, respectively.

As expected, the upper bound results showed yield strengths of approximately 210 MPa, 225 MPa, and 240 MPa for variants 16% to 50%, respectively. The lower bound results are approximately 150 MPa, 110 MPa, and 90 MPa for variants 16% to 50%, respectively, displaying a downward trend as the percentage of retrofitting increases. This is because for the lower bound, the substrate acts alone, assuming that the deposit fails at the very early stages of loading.

As the variant percentage increases, the divergence between the upper- and lower-bound models also increases. The gap grows from approximately 60 MPa at 16% to roughly 150 MPa at 50%, which corresponds to a percent difference of 33.3%, 68.7%, and 90.0%, respectively. This increasing gap in performance between the two models indicates that higher retrofitting levels introduce significantly greater sensitivity to the modeling assumptions and boundary conditions. This indicates that experimental studies to define the interface bonding behavior between the two materials becomes incresingly critical as the retrofit percentage increases. Under ideal deposit conditions and post-heat treatment, efficient bonding is possible, but the results from experimental tests will likely fall between the two curves shown in the subfigures in figure 6.5.

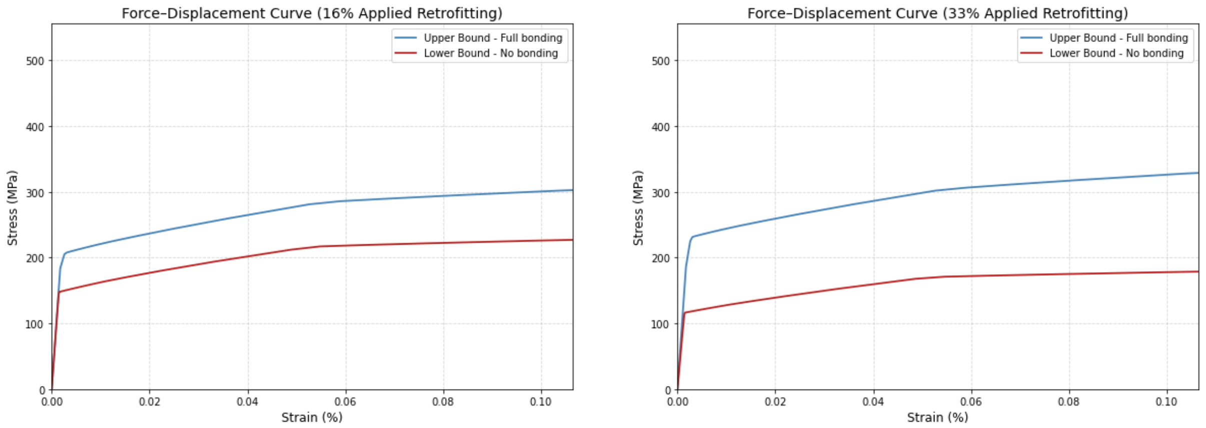

(a) 16% PD

(b) 33% PD

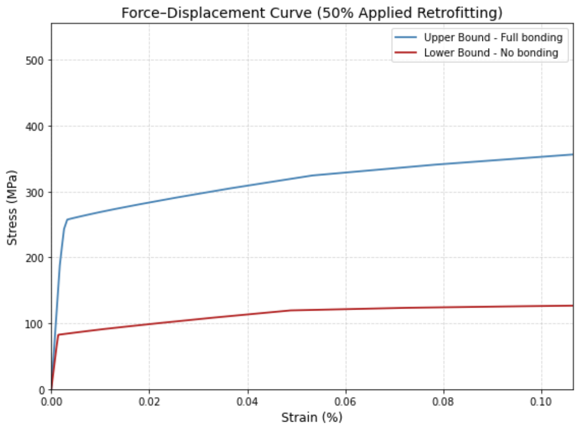

(c) 50% PD

Figure 6.5: 16%, 33%, and 50% PD comparisons.

6.2 Model B: Compact Specimen - Fracture Toughness Results and Interpretation

The K_{IC} values for both 316L and S235 materials were found from existing experiments in literature [37][25]. These values were used as reference points when interpreting the K1 outputs from the crack failure model.

6.2.1 Mesh Sensitivity Analysis

Four meshes were selected for this analysis, each specifying a different number of seeds along the countour line perimeter.

- Mesh 1: 16 seeds
- Mesh 2: 20 seeds
- Mesh 3: 28 seeds
- Mesh 4: 40 seeds

For the finer mesh, additional seeds were added between the contour lines to keep the mesh square rather than rectangular. The mesh was verified at each iteration to check the minimum tri mesh angle around the crack. The allowable range was between 20 - 30°. The first two meshes fall within this range.

Due to numerical inadequacies in the stress and strain values at the fracture tip, the first contour line is neglected from the analysis. It is thus preferable to select a contour line on the outer edge. For all results, contour line 4 was selected.

Figure 6.6 shows all selected meshes with all contour lines plotted in one figure. All K1 values converge, confirming the model's accuracy for the desired results. The first mesh of 16 seeds is sufficient for the desired results, so it was reselected for the second model.

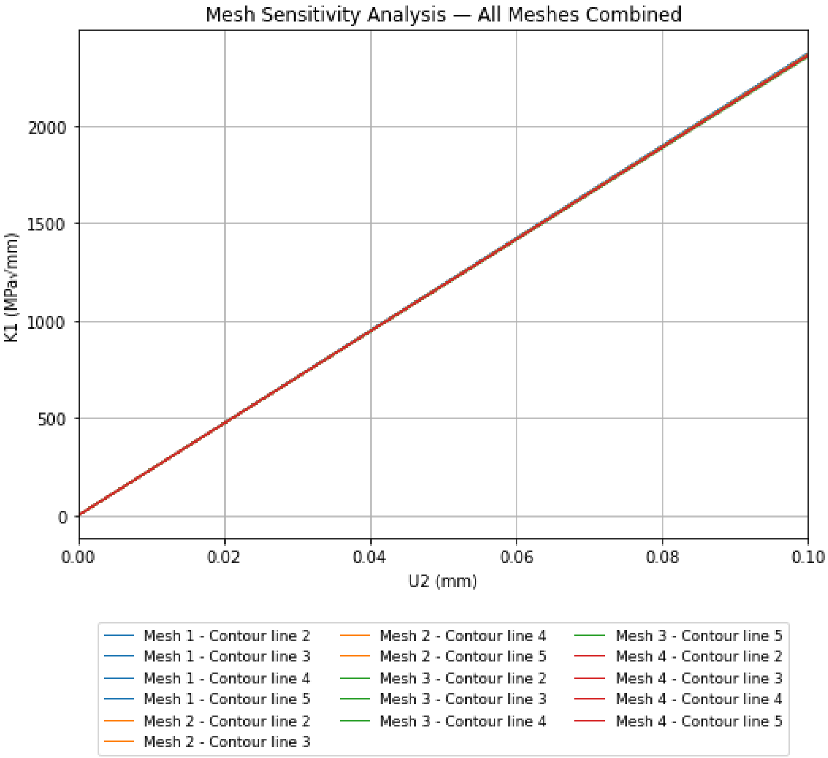

Figure 6.6: Mesh Sensitivity Analysis of Open Model

6.2.2 B.1: Non-retrofitted cracked specimen (Open Notch)

The K_{IC} value for S235 steel is 22.5 $MPa\sqrt{m}$ [37], which converts to 711.5 $MPa\sqrt{mm}$ when transforming the units to match the ABAQUS outputs. This value was plotted onto figure 6.7 as a horizontal line, with the equivalent displacement value extrapolated onto the x axis. This extrapolated value was calculated through linear interpolation, since the slope at that section of the plot is linear. The value at which the fracture toughness of S235 is exceeded came out as U2 = 0.03 mm. The applied load corresponding to the 0.03 mm point is 5,717 N. This was found by multiplying stiffness value k, shown in Appendix D.1.1, by 0.03. Since fracture mechanics modeling is typically load-controlled rather than displacement-controlled, the 5.7 kN load will be selected when comparing the capacity between the different models.

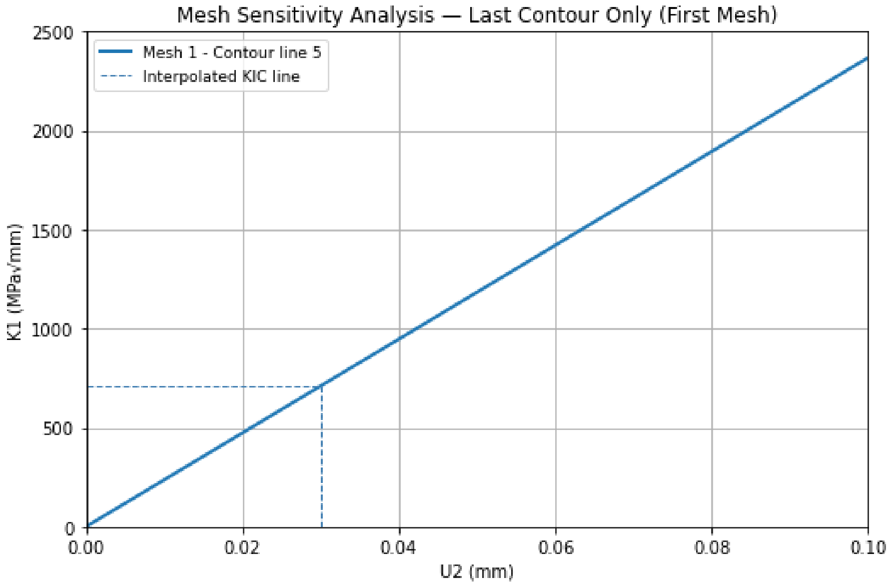

Figure 6.7

Regardless of the mismatch between the ABAQUS model and the available equations, the two were compared in Appendix D.

Comparison to Hand Calculation

For a compact specimen, the following equations can be utilized to calculate the stress intensity factor under various loads [40].

The main variables in this process are the following:

$$\begin{aligned}
\Delta P &= \text{load range (N)},\\
B &= \text{specimen thickness (mm)},\\
W &= \text{specimen width (mm)},\\
a &= \text{crack length (mm), starting from the point of load application},\\
\alpha &= \frac{a}{W} \quad \text{(dimensionless), must exceed 0.2 for the equations to apply},\\
\Delta L &= \text{applied displacement (mm)},\\
k &= \text{stiffness (N/mm) such that } \Delta P = k\,\Delta L.
\end{aligned}$$

The geometry funciton, also denoted as Y1, is the following:

$$F(\alpha) = \frac{2+\alpha}{(1-\alpha)^{3/2}} \Big(0.886 + 4.64\,\alpha - 13.32\,\alpha^3 - 5.6\,\alpha^4\Big), \qquad \alpha = \frac{a}{W}. \tag{6.1}$$

The equation for K is a direct function of this:

$$\Delta K \;=\; \frac{\Delta P}{B\sqrt{W}}\, F\Big(\frac{a}{W}\Big)\,. \tag{6.2}$$

Which can be rewritten as a displacement controlled equation, where k is the ratio of the linear force-displacement curve of the model. It was calculated by dividing the force by the displacement values seen in figure D.2 in Appendix D.

$$\Delta P = k\,\Delta L \quad\Longrightarrow\quad \Delta K(\Delta L) \;=\; \frac{k\,\Delta L}{B\sqrt{W}}\, F\Big(\frac{a}{W}\Big)\,. \tag{6.3}$$

$$\Delta K \;=\; \frac{k\,\Delta L}{B\,\sqrt{W}}\,\frac{2+\dfrac{a}{W}}{\left(1-\dfrac{a}{W}\right)^{3/2}}\left(0.886+4.64\,\frac{a}{W}-13.32\left(\frac{a}{W}\right)^{3}-5.6\left(\frac{a}{W}\right)^{4}\right) \tag{6.4}$$

The full hand calculations can be seen in Appendix D. Observing figure 6.8, one can see that the K1 values start at zero and slowly begin to diverge. When utilizing a crack length of 3.7 mm, which is the length between the load application and the notch edge, excluding the precrack length, the hand calculations nearly perfectly align with the ABAQUS model, as seen in figure 6.9. It is possible that the ABAQUS model excluded the seam as part of the K1 calculation, and only took the open notch as an input. In addition, the loading in ABAQUS is only applied at the top in the model, when in reality it should be placed symmetrically along the horizontal axis of the specimen. As a result, the top displaces in both the U2 and the U1 directions. The remaining misalignment between the 3.7 mm hand calculations and the ABAQUS model can thus be attributed to this imperfection.

If the K_{IC} value is taken as the threshold for the initiation of fast fracture, preceded by steady crack propagation, then the original hand calculations (including the precrack dimension) indicate that the crack exceeds its fracture toughness limit at an applied displacement of 0.0245 mm. The ABAQUS model reaches it at 0.030 mm, which yields a 22.4 % error. This is not within the allowable error range, thus the ABAQUS modeling should be further explored to match its behavior to the 4.9 mm crack length. The hand calculations for the 3.7 mm crack reach that point at deflection 0.0309 mm, yielding a 2.9 % error. This falls in the acceptable error range, but does not accurately represent the selected coupon geometry.

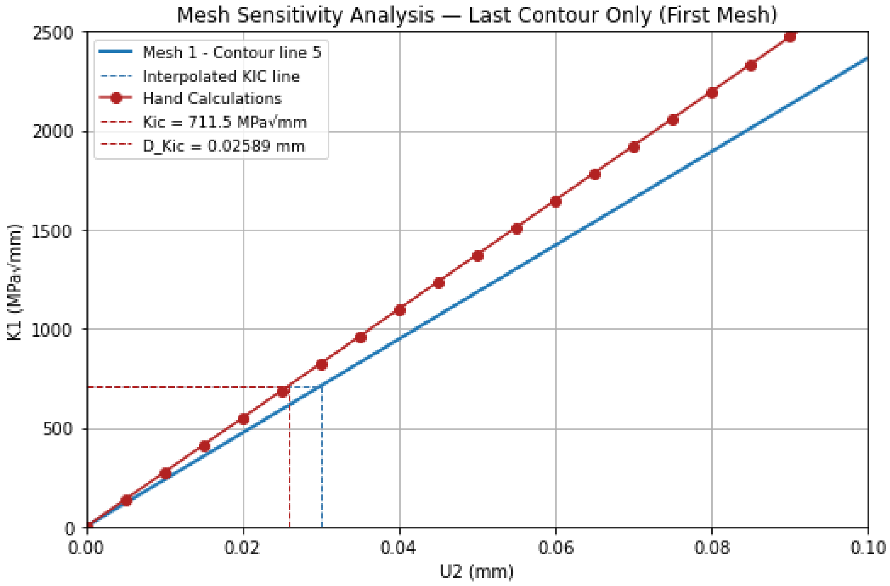

Figure 6.8: Hand Calculated K1 values plotted against ABAQUS K1 values for comparison, with a crack length of 4.9 mm.

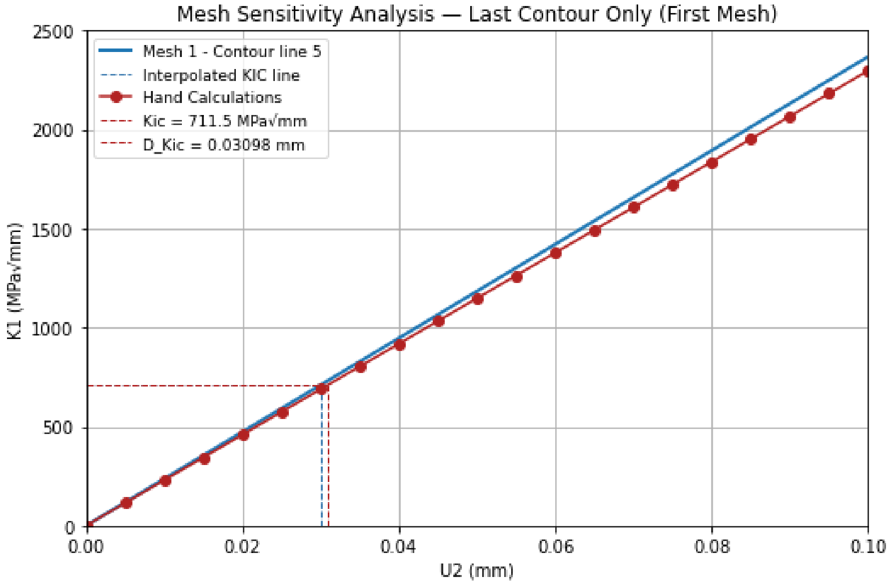

Figure 6.9: Hand Calculated K1 values plotted against ABAQUS K1 values for comparison, with a crack length of 3.7 mm.

6.2.3 B.2: Retrofitted cracked specimen (Closed Notch)

Both cracks from the retrofitted model were plotted for comparison, to determine which one surpasses its stress intensity threshold first. The same mesh was used as the previous model, so a mesh sensitivity analysis was not repeated. All contour lines converged, thus validating the K1 outputs of the model. The plotted results are displayed in figure 6.10.

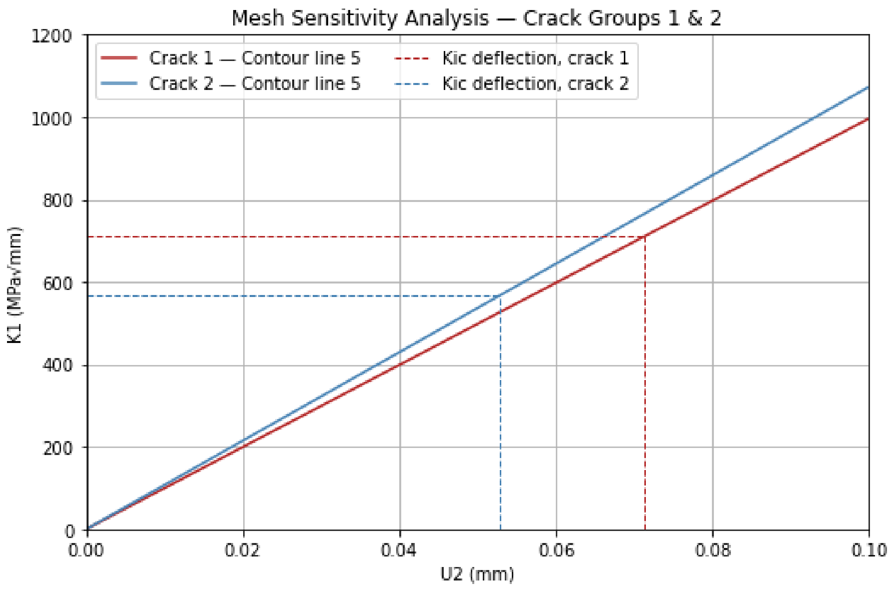

Figure 6.10: Both cracks of retrofitted specimen with both material K$_{IC}$ values plotted for comparison

Interpretation

In figure 6.10, both crack 1 and 2 K1 values are plotted for interpretation, along with their corresponding materials' K$_{IC}$ values, shown in horizontal lines. From those lines, the displacement point was extrapolated.

Crack 2 corresponds with the deposit material, and it has a lower K$_{IC}$ value. While it has a higher yield strength, this analysis can only be copmleted with LEFM assumptions, thus its higher strength does not influence the results.

The K$_{IC}$ value for the deposit material is 18 $MPa\sqrt{m}$ [25], which converts to 569.2 $MPa\sqrt{mm}$. The ABAQUS simulation surpasses this value at a displacement of U2 = 0.052 mm. For the substrate material, the K$_{IC}$ value is 711.5 $MPa\sqrt{mm}$, as mentioned previously. This value is surpassed at U2 = 0.071 mm. From this interpretation, one can conclude that the governing failure mechanism for this model is fast fracture throughout the retrofit material, since the stress concentration factors have a steeper increase in that area.

It should be noted that after applying the retrofit material, there is a notable increase in deflection capacity from 0.030 mm to 0.052 mm, a 73% increase, before the stress intensity limit of either material is surpassed. The axial load value corresponding to this point is 59,146 N (found with k from Appendix D.1.1) which is more than 10 times higher than the non-retrofitted specimen. This 935% increase is attributed to the stiffness value k of the retrofitted specimen being significantly higher, considering the added cross-sectional area. The high strength of the deposit likely contributed to this increase as well.

The notch failing first can be attributed to several reasons:

- Both materials are treated as linear elastic, in which case, the 316L has a slightly lower elastic modulus than the S235 steel. This plays a role because the elastic modulus is the only material property taken into account, besides K$_{IC}$.

- The retrofit material has a lower K$_{IC}$ value, so it is surpassed at an earlier point than if the two materials had the same fracture toughness threshold.

- The load is applied above the notch, which is where the cold spray material is used for the retrofitting. As a result, more load is taken by this area.

When retrofitting elements subject to fatigue loading, it is more effective to apply retrofit material with high fracture toughness [38], as discussed in the discussion of Chapter 3. This is because a higher K_{IC} value has higher resistance to crack propagation. Observing the results in figure 6.10, even if both materials had a fracture toughness of 22.5 $MPa\sqrt{m}$, the deposit material would still fail first, since its stress intensity factor values are higher. Therefore in this case, the deposit would have to have a K_{IC} value of at least 780 $MPa\sqrt{mm}$, or 24.7 $MPa\sqrt{m}$, for the substrate to fail first. This failure would occur at a load of approximately 80 kN, which increases the element's load capacity by an additional 36%.

6.3 Model C: Compact Specimen - Ductile Failure Results and Interpretation

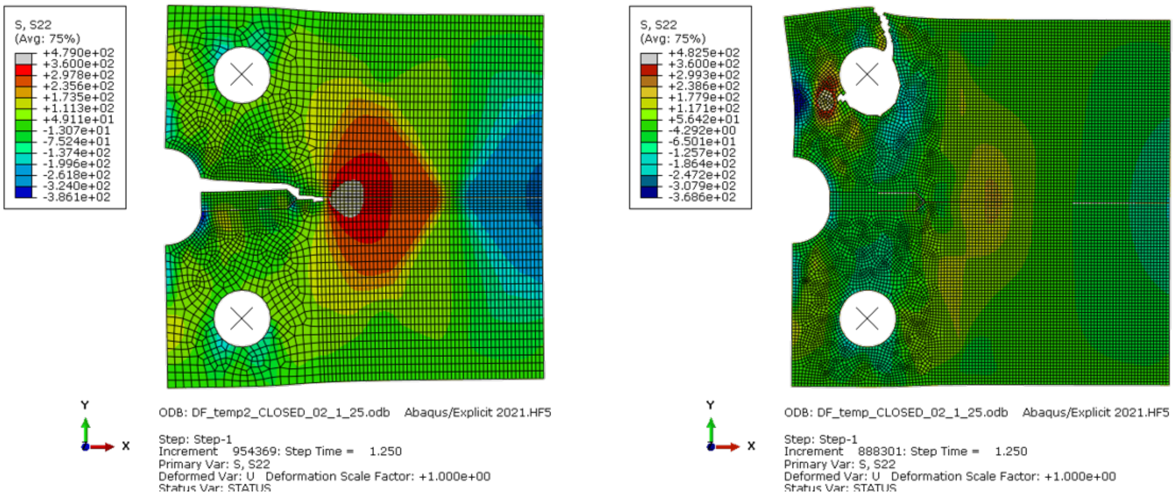

(a) Ductile failure at interface

(b) Ductile failure at connection

Figure 6.11: Two ductile failure mechanisms observed through different mesh distributions

During the sensitivity analysis, two ductile failure mechanisms were observed, as demonstrated in figure 6.11. The first one, in figure 6.11a, depicts the ductile failure at the interface between the deposit and substrate. The second one in figure 6.11b shows ductile failure around the top bolt, where the displacement is applied.

The only difference between the two models is the mesh distribution. The mesh around the notch and interface is 0.2 mm for both, however in figure 6.11a, a coarser mesh of 0.5 mm was applied in all other areas. For figure 6.11b, a 0.2 mm mesh was applied throughout the entire model.

This means that during experimentation, if perfect bonding is achieved between the cold spray and the substrate, the compact specimen may fail at the top bolt where the displacement is applied. This can be explained by the fact that the material in that area is weakest, as S235 has significantly weaker mechanical properties than the 316L steel, which is located along the same x coordinate of the applied load. The purpose of a C(T) specimen is to fail at the center of the element where the notch is. To achieve this, the capacity of the steel around the load-application bolts should be increased. This can be done by adding steel height and width around the bolt, thus making the specimen larger. A parametric study should be completed to design the new C(T) specimen dimensions to shift the weakest point of the specimen back to the notch, thus fulfilling the intended failure location of this specimen. This is necessary for the experimental simulations, since mesh refinement is not possible.

This is also structurally relevant in the real-life application of CSAM on bolted connections. Refilling fatigue cracks with 316L deposit will likely shift the weakest cross section to a different area of the connection, especially if a perfect bond is achieved. This means that the governing failure of the connection after retrofitting may occur at a nearby bolt, similar to the ABAQUS simulation in figure 6.11b. Upon CSAM application to an existing connection, the connection may need additional retrofitting at all potentially critical areas to prevent other failure modes from governing.

It should be noted that the chances of a perfect bond between the deposit and substrate are highly unlikely. While the modeling assumes perfect bond due to limited experimental data, debonding between the substrate and deposit is the expected failure mechanism during testing. It is therefore acceptable to proceed with the model in figure 6.11a, which applies a finer mesh only at the expected critical location to represent debonding at the interface.

6.3.1 Sensitivity Analysis - Variable Selection

Mesh Sensitivity Analysis

Four different mesh sizes were applied and ran at a time duration of 3 seconds. All results converged, except for after the damage initiation point, since the deflection at failure changes based on the mesh size, thus the damage criteria adjusts with the mesh. Since the results prior to the peak load converged, it was concluded that all selected meshes are appropriate for the simulation. In figure 6.12a, it is observed that a coarser mesh allows for a delayed damage initiation point, which is desirable for the final results of this thesis. While 0.3 mm is the highest mesh in the analysis, a mesh of 0.2 mm was selected. This is because the interface for the coarser model only reached partial failure in the desired time increment, which was determined by a time sensitivity analysis as seen in figure 6.12b.

Time Sensitivity Analysis

A time sensitivity analysis was ran with 8 different time durations. A mesh of 0.2 mm was selected, with an applied deflection of 1 mm. Past the time of 1.25 seconds, the results lost significant accuracy. Any time less than 1 seconds was not sufficient to exceed the ductile failure point of the element. The 1.25 seconds time duration was selected for the final model. The plotted outputs of this sensitivity analysis can be seen in figure 6.12b.

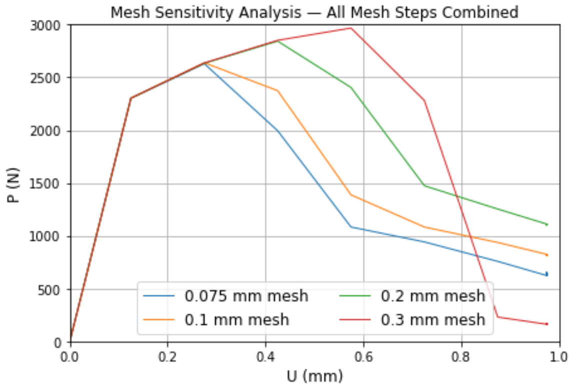

(a) Mesh Sensitivity Analysis of the explicit ductile failure model

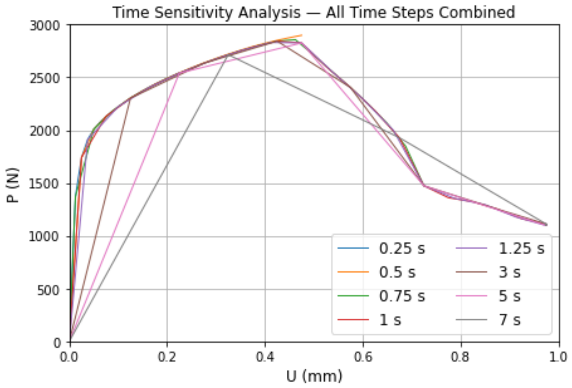

(b) Time Sensitivity Analysis of the explicit ductile failure model

Selected Variables

The model was run with the 0.2 mm mesh for a 1.25 second duration. All simulation steps steps with their corresponding deflections and axial loads for all three model iterations are displayed in table 6.6.

Step	D [mm]	P (Non-retrofitted) [N]	P (Retrofitted) [N]	P (Undamaged) [N]
0	0	0	0	0
1	0.0375	601.521	1910.02	1909.52
2	0.1	1000.51	2222.78	2204.60
3	0.1625	1120.40	2402.34	2381.90
4	0.225	1159.65	2540.04	2516.15
5	0.2875	1180.36	2654.86	2626.95
6	0.350	1160.41	2752.26	2723.05
7	0.4125	1124.25	2830.60	2806.10
8	0.475	1082.00	2826.30	2874.47
9	0.5375	1036.34	2554.43	2928.27
10	0.600	986.343	2296.54	2972.61
11	0.6625	930.514	2000.36	2920.74
12	0.725	873.104	1473.60	2508.43
13	0.7875	814.682	1354.47	2067.15
14	0.85	756.303	1294.74	1830.74
15	0.9125	700.814	1178.54	1704.66
16	0.975	629.383	1096.53	1443.10
17	0.975	644.526	1106.99	1446.91
18	0.975	645.152	1111.07	1445.41
19	0.975	638.368	1108.93	1443.95
20	0.975	650.793	1110.30	1442.55

Table 6.6: Force-displacement data for all simulation steps for all three C(T) model variations

6.3.2 C.1: Non-Retrofitted Cracked Specimen (Open Notch)

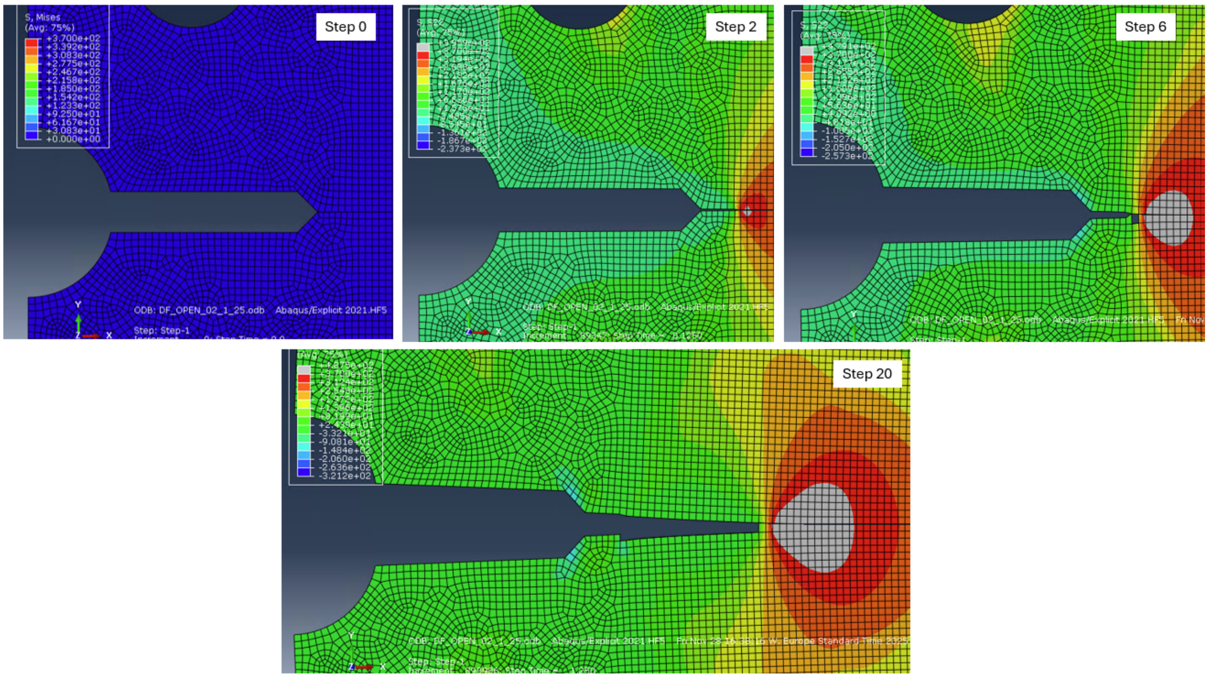

Figure 6.13: Significant steps throughout the ABAQUS simulation of the original compact specimen.

For the open-notch model, the same mesh and time durations were set as for the retrofitted model, which is seen in the next section. A sensitivity analysis was run for both variables. The force-displacement curve of the specimen is seen in figure 6.14.

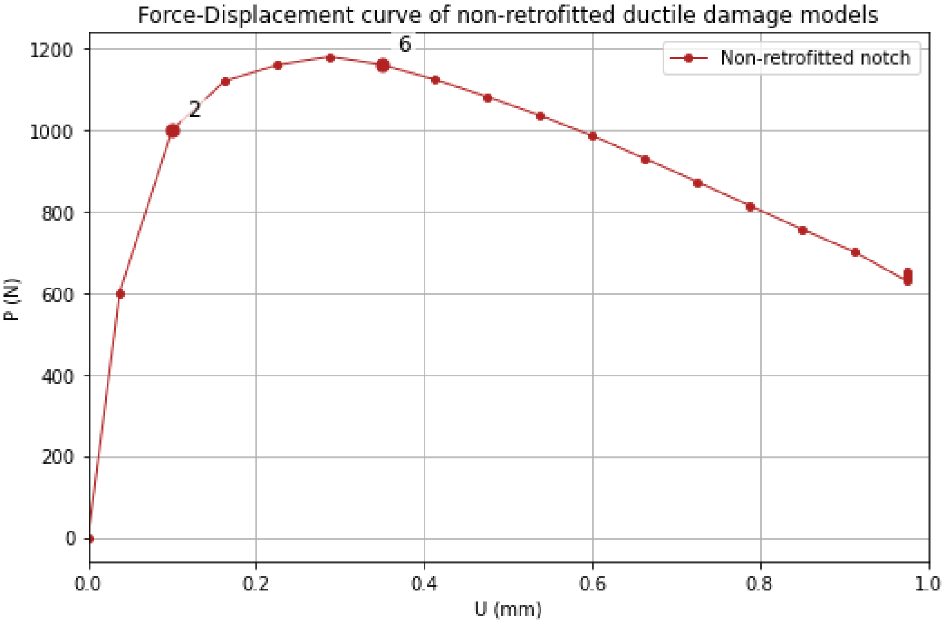

Figure 6.14: Force-displacement curve of the non-retrofitted compact specimen.

This model sustains approximately 1200 N of tensile load before damage initiation occurs in the material surrounding the crack. At step 6, which is denoted by the 7th dot in plot 6.14 (considering the step count begins at 0), damage initiation and thus element deletion begins in the ABAQUS model. This point signifies the start of tension-induced cracking and material softening. The load capacity steadily decreases as the damage factor increases from 0 towards 1. Ultimately the damage comes to an end partway between the crack end and the specimen edge, as only 1 mm of deflection was applied. At the 1 mm point, the capacity of the specimen has dropped to 650 N, from a max capacity of 1180 N. All the mentioned steps are documented in figure 6.13.

This model serves as a basis of comparison for the retrofitted model, to observe the capacity of the specimen prior and post retrofitting.

6.3.3 C.2: Retrofitted cracked specimen (Closed Notch)

The selected time duration for the analysis is 1.25 seconds, with a mesh size of 0.2 mm. Both of these values were selected by running a sensitivity analysis for each variable, as seen in figures 6.12b and 6.12a. The final force displacement curve is seen in Figure 6.15.

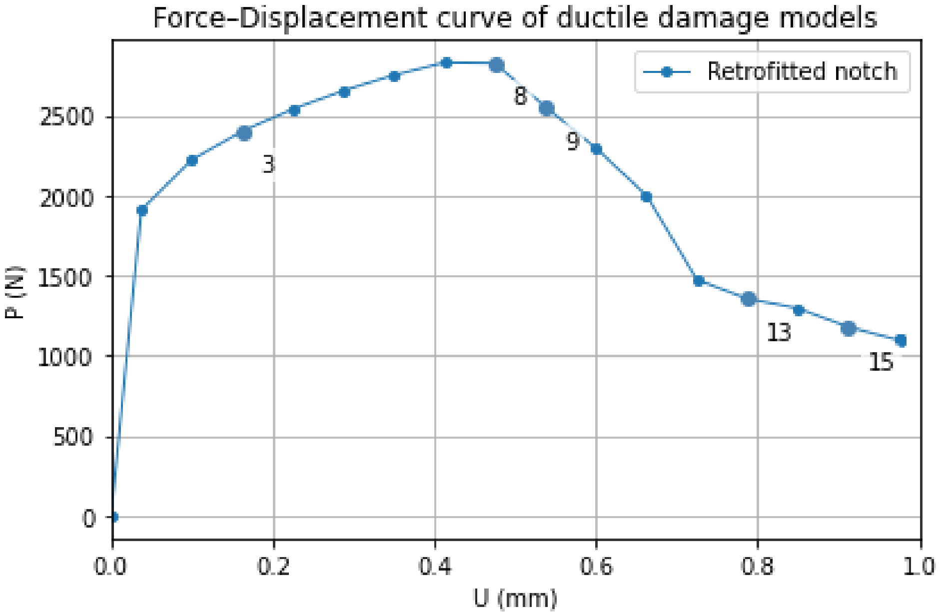

Figure 6.15: Force-displacement curve of the retrofitted compact specimen.

The retrofitted model reaches 2830 N as its ultimate tensile capacity. Damage initiation and material softening begins somewhere between steps 8 and 9, which are denoted by the 9th and 10th dots, respectively, on figure 6.15. At these points, much of the substrate area surrounding the notch has exceeded its maximum load capacity, and the S235 steel begins to fail at the interface. The damage criterion significantly drops as the horizontal area around the notch fails and slows down as the damage around the angled interface begins and extends onto the rest of the specimen. The same steps are shown in figure 6.16, where the regions exceeding the S235 UTS value are marked in gray.

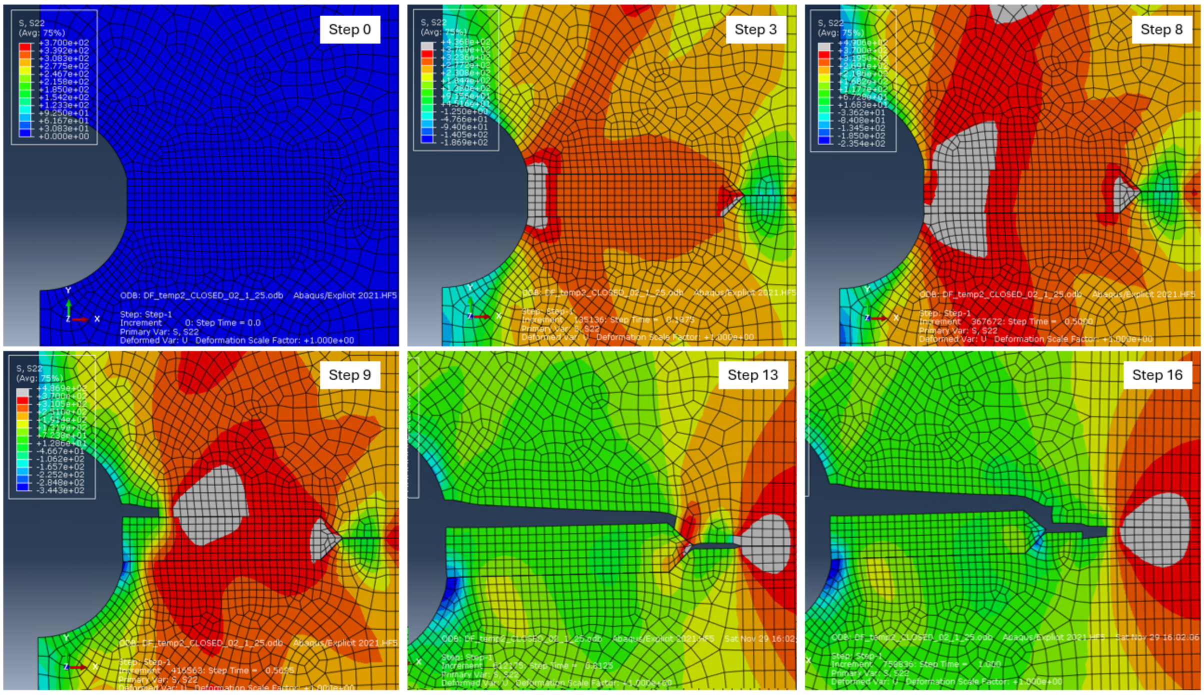

Figure 6.16: Significant steps throughout the ABAQUS simulation of the retrofitted compact specimen.

6.3.4 Discussion

Comparing non-retrofitted and retrofitted compact specimen models

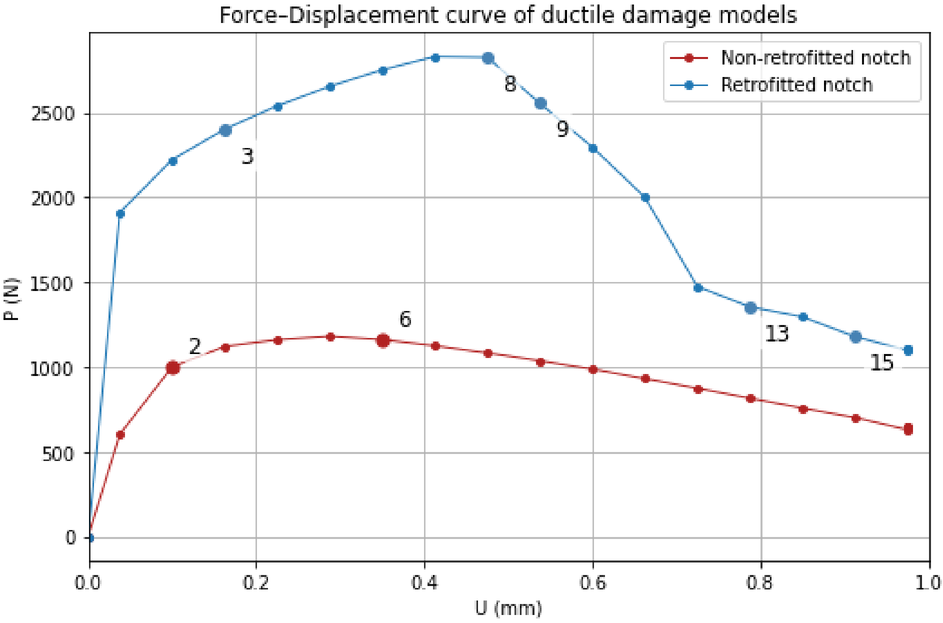

Figure 6.17: Force-displacement curves of both retrofitted and non-retrofitted specimen, annotated with important steps from the simulation

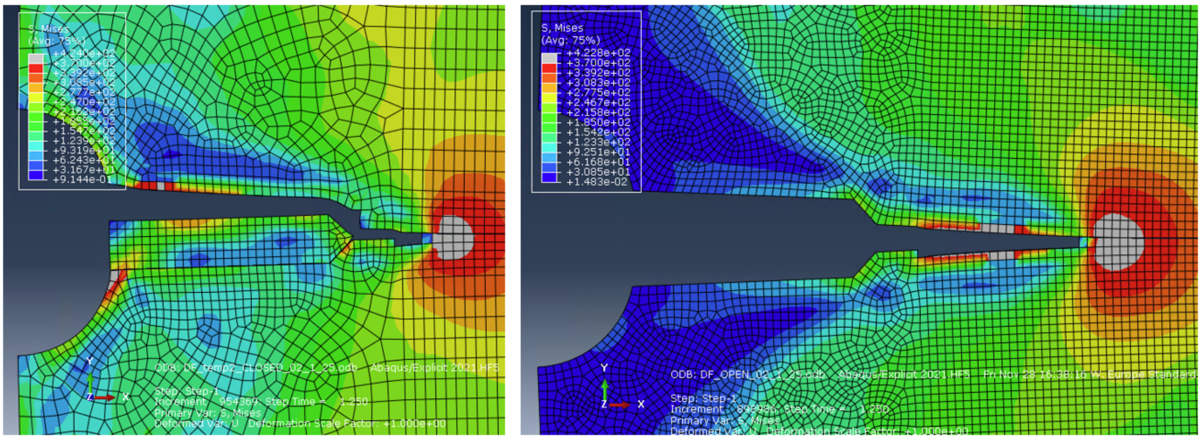

Figure 6.18: Retrofitted and non-retrofitted specimen (respectively) at the final step of the simulation (U2 = 1 mm).

The retrofitted model exhibits a substantially higher tensile capacity, reaching a peak load of 2830 N compared to 1180 N for the non-retrofitted model. Its capacity at the end of the simulation is also higher, at 1110 N versus 650 N.

The damage initiation for each model begins at different points of the simulation. The open model loses some cross-sectional capacity due to its reduced cross-sectional area, as the notch remains open and the crack is free to open further. The retrofitted model not only has a stronger material, the 316L, as part of its cross-section, but the filled notch provides additional cross-sectional area to resist the tensile load that is induced by the displacement. As a result, the element has a higher stiffness, denoted by the steeper slope of the force-displacement curve in the elastic region. The stiffness values were calculated with the following process, where the gauge length is taken as the distance between the two reference points (where the boundary conditions are applied):

$$Gauge\,Length : L = 14.4mm$$

And the areas exclude the fatigue precrack length from the cross-section:

$$A_{open} = 9.6 \cdot (15.5 - 1.2) = 137.28mm^2 \qquad A_{closed} = 9.6 \cdot (21.57 - 1.2) = 195.5mm^2$$

To calculate the equivalent elastic modulus of the specimen, the force-displacement curves need to be converted to stress-strain curves. They can be converted through the following:

$$\sigma = \frac{P}{A} \qquad \varepsilon = \frac{D}{L} \qquad E = \frac{\sigma}{\varepsilon}$$

Looking at the points in the elastic region, the newly obtained values can be inserted in the axial stiffness equation seen below:

$$k = \frac{AE}{L}$$

The initial stiffness of the open model is 16,040 N/mm, while for the closed its 50,933 N/mm, over three times the magnitude.

The damage evolution of each model occurs at different rates: the non-retrofitted specimen reaches and then exceeds its maximum load capacity at around 0.3 mm, after which its capacity gradually decreases until the end of the simulation. In contrast, the retrofitted model shows a more pronounced damage response, with a noticeably steeper post-damage-evolution softening slope. The steep slope occurs during the debonding phase between the deposit and substrate, specifically the horizontal section. Since the deposit material offers substantially higher tensile strength than the substrate, this explains why significant capacity is lost during the debonding process. Once the top has fully debonded at step 13, visualized in figure 6.16, the damage evolution proceeds at a gentler slope. Once the ductile damage extends to the S235 steel past the crack, the capacity values begin to match, although for the closed-notch specimen this occurs at step 15, whereas the open-noth at step 6. The capacity values of these two points are 1178 N and 1160 N, respectively. The difference in the final capacity can be explained by figure 6.18, which shows the overall damage at the last step of the simulation. There is less cross-sectional area remaining for the non-retrofitted specimen, thus justifying its reduced capacity. All steps mentioned in these observations are annotated in figure 6.17.

To act as a reference point, a simulation was run without any cracking or retrofitting present to act as a representation of the original undamaged specimen. This way, the retrofitted specimen could be compared to its ideal scenario, and evaluate the limitations of the debonding. Studying this additional plot, seen in figure 6.19, one can observe that because of the filled notch, the yield strength between the original and the retrofitted material are similar. The early stages of the plastic behavior have a slightly higher tensile capacity for the retrofitted model, reaching a capacity of 2830 N as opposed to the 2806 N of the undamaged model. This 0.8% increase is due to the higher-strength material used to seal the crack. The main difference between the two is the damage initiation point. The undamaged model reaches a maximum load of 2972 N, at a displacement of 0.6 mm, before damage initiation occurs (step 11). When compared to the damage initiation point of the retrofitted model, which occurs at displacement 0.4125 mm with a load capacity of 2830 N (step 7), this shows a 5% improvement in load capacity and a 45% increase in fracture initiation displacement when using a deposit that is the same strength as the substrate. Since the deposit orientation is perpendicular to the load and there is a high mismatch of tensile strength between the two materials, the interface becomes the critical section of the retrofitted C(T) specimen, thus debonding occurs at an earlier stage. When the same material is applied to seal the notch, a uniform cross-section is built across the specimen, thus preventing the interface from governing. This applies only is full bonding and full shear interaction are achieved.

It should be noted that since the undamaged model does not fail at the interface, it fails at the next weakest cross-section, which is at the top or bottom bolts of the specimen, where the boundary conditions are applied, as seen in figure 6.20. As discussed previously, this is not the intended failure location for this specimen, so the height and width dimensions surrounding this bolt should be redesigned to localize the failure at the notch. This way, the two model variations (retrofitted and undamaged) can be more accurately compared. Regardless of this, the current comparison shows the limitations that come with the retrofitted model.

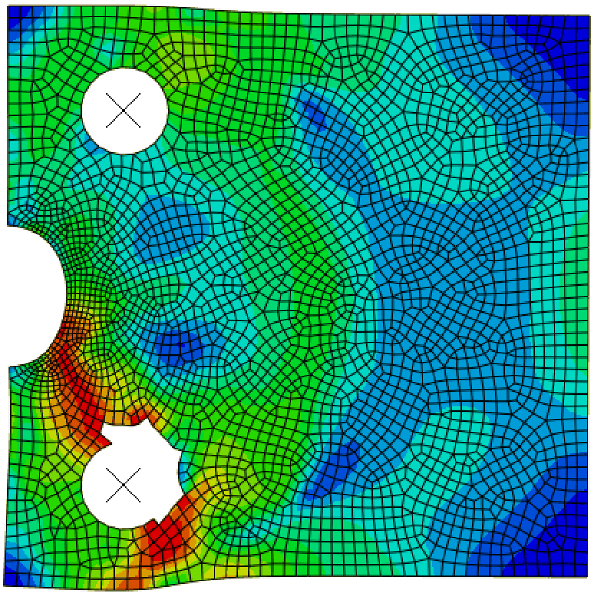

Figure 6.20: ABAQUS simulation of the same specimen geometries as the compact specimen, without any cracking present.

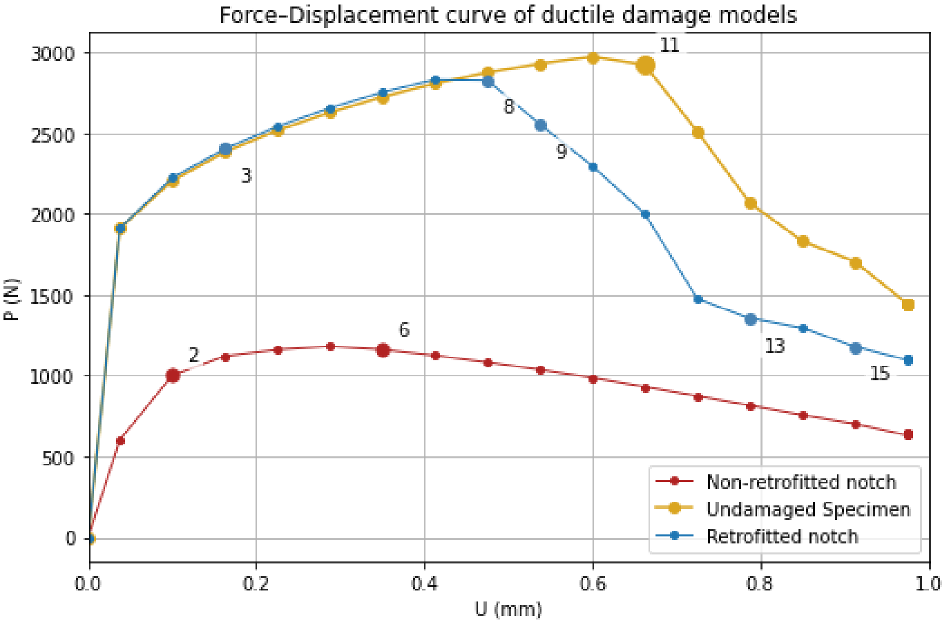

Figure 6.19: Force-displacement curves of both retrofitted and non-retrofitted specimen, plotted against the undamaged specimen.

In short, most of the capacity is restored when the crack is filled, as the cross-sectional area and thus specimen stiffness are restored, regardless of the material. Since the cold spray material is significantly stronger than the substrate, the internal stresses are not distributed uniformly, and the weakest cross-section shifts to the interface. In this case, the S235 steel at the interface fails first, inducing preliminary damage evolution in the specimen. Unlike the A.1 model study, the mismatch of yield strength between the two materials weakens the structural behavior of the element.

For the retrofitted model, the bonding between the deposit and substrate is modeled as full shear interaction due to research limitations. In experimental cases, it is expected that the debonding will occur at an earlier deflection point, thus lowering the overall tensile capacity more than what is shown in figure 6.19.

Tying K1 and Force-Displacement results together

While the results from the ductile-failure models are quite intuitive, the results from the previous model exploring crack failure should also be taken into consideration.

The two cannot be directly compared, since one is a linear model, and the other is a non-linear. A direct comparison between the two is not entirely reliable due to the different analyses, however an assumption can be made about the governing type of failure of each model by comparing their axial load capacities.

Looking at the non-retrofitted model in figure 6.17, damage evolution of the specimen begins at a load of 1.2 kN, which represents its max tensile capacity. The plots and interpretation from the fast-fracture study showed that fast fracture occurs at 5.7 kN, which is never reached throughout the non-linear model simulation. Based on these results, ductile damage governs.

As for the retrofitted notch, it is able to reach 2.8 kN of tensile load before ductile damage initiation. Fast fracture is reached at 59 kN, which is significantly higher than the peak load of this simulation. As a result, interface debonding due to ductile damage governs for the retrofitted model as well.

It should be noted that the steel will yield before the fracture toughness is exceeded for both models. This may affect the crack propagation and ultimately the fast fracture behavior. The exact behavior is uncertain based on the available data.

It is possible to run a nonlinear model to evaluate the energy release rate, represented by J-integrals, of each crack. Due to time limitations, this analysis was not run for comparison.

Chapter 7

Life Cycle Analysis

As environmental risks increase, and awareness of the environment grows, both the manufacturing and consuming of products must be studied to better understand their impact on the worsening state of the environment. One of the techniques commonly used for this assessment is the Life cycle assessment (LCA) [46].

7.1 Goal and Scope

7.1.1 Goal

The goal of this LCA is to compare the greenhouse gas footprint of recycling steel versus retrofitting steel to see whether this retrofitting process is actually beneficial environmentally speaking, or if there are hidden CO_2 emissions that are not obvious at first glance. If there is a chance that recycling is more environmentally beneficial, then more research may be needed for cold spray additive manufacturing applications to meet the current Dutch carbon emission goals, since the main purpose of retrofitting as compared to recycling is to further reduce the carbon footprint of steel usage. Finally, both shall be compared to newly fabricated steel, which acts as a baseline of carbon emissions typically produced from steel use.

For this LCA, a cradle to cradle approach is selected. This approach assesses a product's lifecycle where the aim is to keep it in circulation, whether this is through recycling, remanufacturing, or retrofitting [47], thus disregarding the disposal stage. This way, all the possible life cycles per element can be taken into consideration and used to determine each element's overall footprint. This is because a cradle-to-cradle product may end up showing an increased burden, so it is important to assess conclusions depending on the overall number of cycles [48].

These results are intended for steel manufacturing companies and direct stakeholders for new steel construction projects. A flowchart showcasing the applicable life cycle stages is shown in Figure 7.1. The use stage was excluded from the analysis due to lack of data. It was also considered less critical than the production and dismantling stages, which more clearly distinguish between the three selected elements. The selected impact category is total GWP emissions, including fossil fuels, biogenic, and luluc (when provided), and all data is representative of current Dutch construction practices.

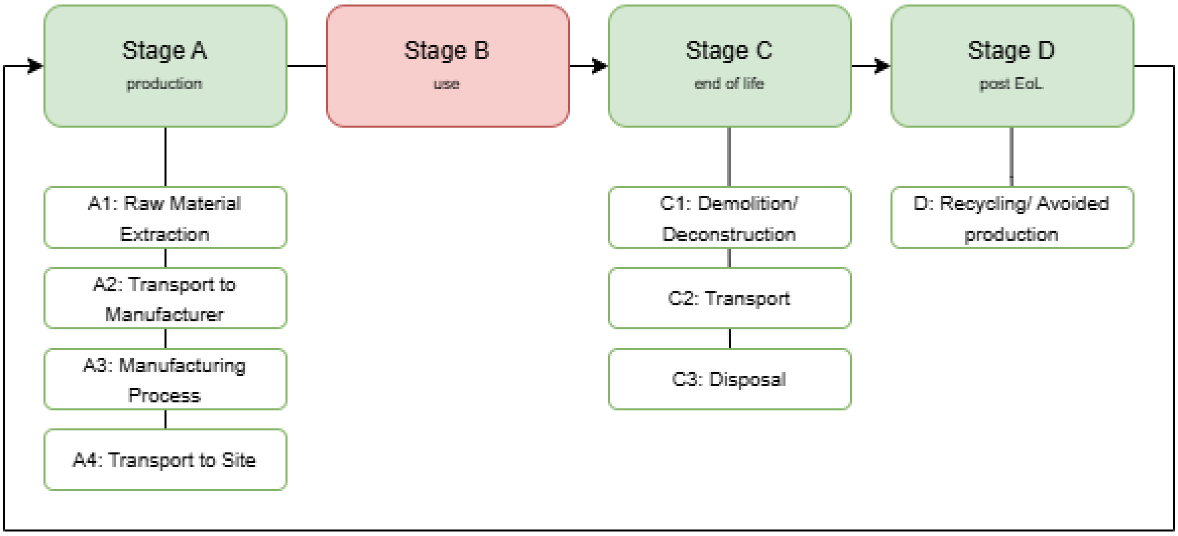

Figure 7.1: LCA Applicable Stages Flowchart

7.1.2 Scope

Considering the fatigue cracking patterns and locations as seen in existing case studies [15], a connection resembling the bolt-layout as seen in figure 2.2 was selected for this LCA. This is because it represents a stringer-to-floor-beam connection, one of the most common areas for fatigue cracking in steel bridges. As seen in the image, a fatigue crack may form along the length of the plate connecting the two beams. Thus fatigue cracking along the connection plate was selected as the failure mechanism for which the cold-spray will be applied to in this LCA. When replaced or retrofitted, the rivets will have to be removed and replaced, so the entire connection material will be considered in the final global warming potential calculations. This study focuses on S235 structural steel and explores three scenarios, each representing different EOL pathways:

- Scenario A - recycled S235 steel plate and rivets produced primarily from secondary steel scrap
- Scenario B - retrofitted S235 steel plate repaired with a 316L stainless steel cold spray deposit, extending its functional lifespan, with new rivets
- Scenario C - newly fabricated S235 steel plate and rivets, serving as the baseline for comparison

The functional unit of this study is the floor beam, the main girder that transfers the vehicle loads to the bridge supports. If the connection at this beam fails, so does the bridge structure. The function is for the second life cycle of this girder (thus bridge) to last another 100 years. Only one connection will be included per girder in this analysis, as there are higher chances of failure on one side than both sides.

The lifespan for each scenario is stated as the following:

- Scenario A - 100 years
- Scenario B - 10 years
- Scenario C - 100 years

The newly fabricated elements are expected to have a service life of 100 years for bridge elements. Recycled elements are expected to match this service life. Due to lack of data, it is unknown how long the additional lifespan of a girder is after retrofitting its connection through CSAM. For this analysis, 10 years was assumed. It is also assumed for scenario B that perfect bond and full shear interaction happens between the deposit and substrate, and that localized heat-treatment is possible to allow material ductility.

The level of intervention required also changes depending on the scenario. Rather than including the full embedded carbon of the bridge structure, each scenario accounted for its corresponding level of intervention required for connection repair:

- Scenario A: Replacement of the existing connection plate requires full disassembly of the connection. Temporary structural supports are assumed to be installed locally on each beam supported by the connection to ensure load transfer during removal and installation of the recycled plate is possible. This intervention results in short-term disruption of the bridge operation during disassembly and reconstruction, but does not require removal or replacement of the main girder.

- Scenario B: Retrofitting is assumed to be performed in situ without disassembly of the main girder. Depending on the geometry of the crack, the rivets may require removal for full access. In this case, temporary supports are required locally to provide support to the beams. No removal of large existing structural components is required. Under this scenario, the bridge functionality will be disrupted for the duration of the CSAM application and rivet placement. Since no major structural elements need to be removed, the duration of this is reduced.

- Scenario C: The replacement of the connection plate with a newly fabricated element follows the same intervention strategy as Scenario A, including local disassembly, temporary support installation, and short-term bridge disruption, while retaining the existing main girder.

The carbon emissions required to fix the bridge at each scenario vary due to the different EoL processes. When considering the functional unit into the LCA, which is the main girder's lifespan lasting an additional 100 years, the GWP for each scenario must be adjusted according to its corresponding lifespan extension. This is completed in the interpretation section.

7.2 Application to Life Cycle Stages of each Product

The life cycle stages were taken according to the NEN EN 15978 - 2011 [49].

A1-A3: Product stage

Scenario A represents an element manufactured from primarily recycled steel scrap, combined with a limited amount of virgin iron ore. The recycling process includes [50] [51]:

- Collecting and transporting end-of-life (EoL) steel scraps to the manufacturer

- Melting the steel scraps with the new virgin material in electric arc furnaces

- Casting, shaping, and rolling into new structural sections

The environmental data, such as CO_2 emissions and energy use, will be extracted from EPDs or the Dutch National Environmental Database (NMD), referenced for secondary steel production.

Scenario B represents a damaged EOL steel element that has been repaired with CSAM, thus extending its lifespan. The CSAM production process includes [52]:

- Extracting and producing the 316L stainless steel powder into the appropriate grain size and shape via gas atomization
- Transporting the powder from the manufacturer to the site location
- In-situ repair preparation, such as preheating, surface preparation, and optimized parameter selection to ensure efficient deposit
- Heat treatment of the deposited material

The environmental data will be collected from literature, consulting experts, and any available EPDs for 316L stainless steel.

Scenario C represents a scenario where an EOL steel plate is fully replaced with a newly fabricated steel plate. The process consists of [50] [51]:

- Collecting and transporting virgin iron ore, coal, and other raw materials
- Utilizing a blast furnace to prepare the raw materials
- Steelmaking through a basic oxygen furnace or electric arc furnace
- Casting and hot rolling of the final steel profiles
- Painting and coating for finishing touches

This environmental data will be collected from primary steel production EPDs.

A4-A5: Construction process

Scenario A requires transport from the fabrication center to the construction site, using truck, water, air, or rail. Fuel emissions are calculated based on distance, weight, and vehicle type. The construction and installation processes include bolting or welding depending on the type of connections. The structure will either need to be entirely disassembled and have the critical failure elements replaced with recycled materials, or if partial disassembly is possible, then only the critical elements will be removed.

Scenario B does not require transport of the final fabricated item to the site. However, the CSAM and heat-treatment equipment must be transported. Fuel emissions are calculated based on distance, weight, and vehicle type. On-site energy use is covered in A1–A3, though minor assembly operations or accessibility equipment may be necessary to access the damages in the connection. Depending on the cracking geometry and location, it is possible to retrofit the bridge structure without any disassembly.

Scenario C requires transport of newly fabricated steel to the site, similar to Scenario A. The construction and installation process is the same as for Scenario A.

B1-B7: Use stage

Scenario A is expected to require minimal maintenance for coated steel elements. Some maintenance may be necessary depending on environmental exposure.

Scenario B is expected to have corrosion-resistant properties due to the stainless steel deposit; however, the substrate material may still be prone to corrosion. Some maintenance may be required.

Scenario C follows standard maintenance procedures, including periodic inspection, painting, and corrosion monitoring.

C1-C4: End of life

Scenario A is recycled into secondary steel, displacing primary steel production. Energy and emissions associated with dismantling, transport, and re-melting are included. If full-bridge disassembly is required, the rivets from all connections will also need replacing, as they are one-use.

Scenario B may be recycled; however, the deposited 316L layer may affect recyclability, requiring separation or resulting in alloying changes. Minor material losses may occur during dismantling. Little to no additional waste will take place from disassembling other bridge elements.

Scenario C is discarded without recycling or retrofitting.

D: Benefits

Scenario A can be recycled again, thus adding another life cycle. More secondary steel is added to the production, thus reducing the need for primary steel in future projects.

Scenario B extends the life span of the original element and avoids the added manufacturing emissions from the recycling process. This element can also be recycled eventually, however the stainless steel parts will have to be removed, which may introduce other complexities in the future.

Scenario C the plate is not recycled or retrofitted. It can be recycled, in which case the same procedure and standards as the first element apply.

7.3 LCI (inventory analysis)

All EPD data is in accordance with the ISO 14025:2006 and EN 15804:2012+A2:2019/AC:2021.

LCI Item	**Result (kg CO_2)**
S235 Steel production (A)	
Production emissions (A1–A3)	898
Transport to site (A4)	220
End-of-life processing (C)	
Demolition/Deconstruction (C1)	1.12
Transport (C2)	9.68
Waste processing (C3)	26.7
Disposal (C4)	0.964
Recycling credit (D)	
Avoided production	-549

Values from page 13 of EPD [53]: GWP-fossil = Global Warming Potential (Total) with a DU = 1000 kg.

Table 7.1: LCI summary for S235 steel, including recycling option.

LCI Item	**Result (kg CO_2)**
Architectural Powder production (A) [54]	
Raw Material (A1)	3.679
Transport to manufacturer (A2)	0.701
Manufacturing (A3)	-0.022
Transport to site (A4)	0.178
316L stainless steel profile production (A)[55]	
Production emissions (A1–A3)	4.45
Transport to site (A4)	0.031
End-of-life processing (C [55]	
Demolition/Deconstruction (C1)	0.00061
Transport (C2)	0.0073
Waste processing (C3)	0
Disposal (C4)	0.0717
Recycling credit (D) [55]	
Avoided production	-3.01

Values combined from two EPDs [55] [54]: Global Warming Potential (Total), both with a DU = 1 kg.

Table 7.2: LCI summary for 316L powder.

For table 7.2, no EPD documents are published in the database regarding cold spray additive manufacturing, so data from stainless steel profiles was taken instead [55], combined with architectural powder processing data. Life cycle stage A was ignored for the base steel, since it is considered to already exist on site, and is simply being retrofitted.

7.4 LCIA (Impact assessment)

7.4.1 Element Dimensions

The following parameters are selected based on an old riveted railway bridge in Sweden [14]:

- Plate size: L75 x 100 x 9 mm, with a length of approximately 800 mm
- Rivet diameter: ø23 & ø22
- Rivet spacing: 140 mm (5 & 6 total, respectively)
- Floor Beam: L 120 x 80 x 13

The connection design is shown in figure 7.2.

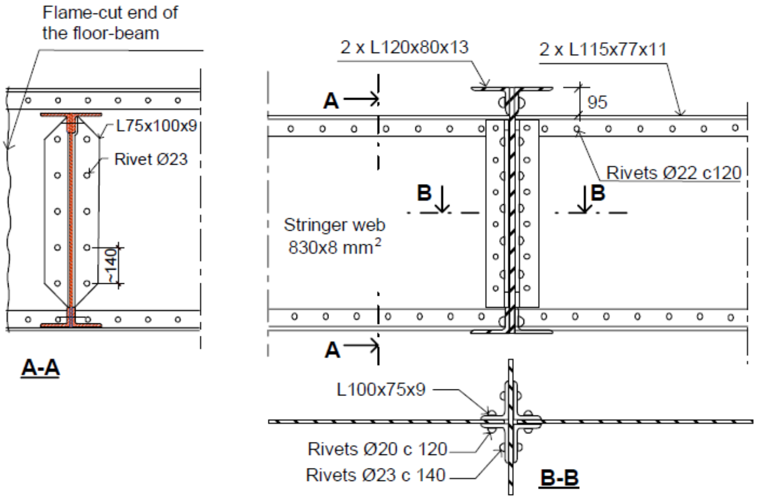

Figure 7.2: Stringer to floor connection, taken from the riveted railway bridge in Vindelälven, Sweden

Connection

Based on the dimensions, the volume of each element is calculated. The calculations start with the rivet of ø23 diameter:

$$A_{23,r} = \pi r^2 = \pi \cdot 11.5^2 = 415.476 mm^2 \qquad V_{23,rivet} = n \cdot A_{23,r} \cdot L = 5 \cdot 415.476 \cdot 25 = 51934.5\, mm^3$$

Rivet, ø22 diameter:

$$A_{22,r} = \pi r^2 = \pi \cdot 11^2 = 380.13 mm^2 \qquad V_{22,rivet} = n \cdot A_{22,r} \cdot L = 6 \cdot 380.13 \cdot 25 = 57019.9\, mm^3$$

Where the rivet length is approximated as 25 mm to account for the plate and web thicknesses, and n represents the number of rivets per side.

Next, the expected volume for the steel plates is the following, subtracting the volume where the rivets are present:

$$V_{plt} = (((75 + 100) \cdot 800) - (380.13 + 415.476)) \cdot 9 = 1252840\, mm^3$$

For riveted connections, equation 7.1 can be used as an estimate for the smallest detectable crack length in millimeters, where d is the diameter of the rivet [18]:

$$a_0 = \frac{d}{2} + 5 \tag{7.1}$$

This equation can be used as a minimum crack length for visual inspections. It is assumed that cracks below this length are likely to be missed during visual inspection [18]. The minimum crack length that will be used for this LCA is therefore:

$$a_0 = \frac{23}{2} + 5 = 16.5\,mm$$

This value falls within the observed fatigue-crack lengths of 10-20 mm of the Vindelälven bridge in Sweden [14]. When applying cold spray additive manufacturing, it is necessary to widen the crack to allow for the deposition particles to fill the entire plate through-thickness. A width of 5 mm was selected to allow for ample space. Assuming that one longitudinal crack forms along the plate, this means the volume of retrofitting material that is required to fill it is:

$$V_{crack} = 9 \cdot 16.5 \cdot 5 = 742.5\,mm^3$$

Girders

Floor beam: L 120 x 80 x 13 (length = 6000 mm)

$$A_{floor} = (120 + (80 - 13)) \cdot 13 = 2431\,mm^2 \qquad V_{floor} = 2431 \cdot 6000 = 14586000\,mm^3$$

The lengths are taken from bridge diagrams shown in the case study [14].

Element Weight Calculations

The density of both the 316L and S235 materials is $7.98e^{-6} kg/mm^3$ [25]. Taking this into consideration, the weights in kilograms of each element are summarized in table 7.3.

Element	**Volume (mm^3)**	**Weight (kg)**
Rivets ø23 (5 pcs)	51,934.5	0.414
Rivets ø22 (6 pcs)	57,019.9	0.455
Steel plate	1,252,840	9.99
Crack repair volume (CSAM)	742.5	0.006
Floor beam	14586000	116.40

Table 7.3: Summary of calculated volumes and corresponding weights for selected elements.

7.4.2 Global Warming Potential Calculations

Total embedded carbon

The fatigue cracking damage will occur at the connection between the stringer and floor beams of the bridge, specifically at the plate of the connection. This affects the entire bridge structure's structural stability. Due to the bridge's structural layout, the main girder, the floor beam, will be included in the GWP calculations of the connection failure, as it is directly impacted by the stability of the connection, and its failure would mean the failure of the bridge structure. By retrofitting or replacing only the connection plate, the main girder can be saved. As a result, the embedded carbon of the connection is in truth much higher than the GWP value from retrofitting or replacing the connection material itself.

Scenario A & C

The total Global Warming Potential (GWP) for a typical L75x100x9 carbon steel section is calculated as the following, where the LCI values from table 7.1 for stage A and C are added together:

$$\mathrm{GWP_C} = (989 + 220 + 1.12 + 9.68 + 26.7 + 0.964) \cdot \frac{0.414 + 0.455 + 9.99}{1000}$$

$$\mathrm{GWP_C} = 12.68 \text{ kg CO}_2$$

This value is the GWP value per newly fabricated steel connection, including the plate and all rivets. While the manufacturing process between steel sections and rivet bolts is different, data for steel sections was used for both due to data availability. Due to the new material, the life expectancy of the connection and thus main girder is 100 years. For the recycled connection, the recycling credit seen in stage D from table 7.1 is subtracted from the total:

$$\mathrm{GWP_A} = 12.68 - 549 \cdot \frac{10.86}{1000} = 6.72 \text{ kg CO}_2$$

In this calculation, 10.86 kg is the sum of all the S235 elements' weights (rivets and plate). It is used to scale down the recycling credit GWP to match that of a single connection.

Scenario B

For the powder, there was no 316L powder information available, so data was combined from stainless steel profiles and architectural durable powder used for coatings [55][54] to serve as an approximation. Only the powder production EPD was utilized for stage A, and the stainless steel EPD for stage C.

Since the base material is being retrofitted, the production life cycle (stage A) for the steel plate and rivets is neglected from the total GWP value. Instead, stage A of the stainless steel and powder production is taken into account, and multiplied by the weight of the required CSAM volume to fill the approximated cracks.

Since the DU for this LCI is 1 kg, the weight of the CSAM does not need to be scaled down by a factor of 1000. In this calculation, the LCI stainless steel and coating powder values from table 7.2 were summed and multiplied by the weight of the retrofit material required to fill the crack. More specifically, the manufacturing and construction values (stage A) for the architectural powder were added to the stage A and C values of the stainless steel profiles. This was done because this was the only available data relevant to 316L stainless steel powder. Since for this thesis' CSAM process 316L steel needs to be extracted, the 4.45 kg $\mathrm{CO_2}$ seen in stage A1-A3 is justified as a conservative value (since it also includes molding the material into cross-section profiles). The powder's stage A is broken down into more detail. Since raw material extraction and transportation is already considered in the 4.45 kg CO_2, only the A3 value, −0.022 kg CO_2 is relevant, as that is the part where the material is transformed into powder. Therefore only that value is considered in the summation of CO_2 emissions for CSAM. As for stage C, only data for the stainless steel profiles is available, thus it was used by default. The recycling credit was neglected, because for the final element to be recycled, the retrofitted connections will likely be sent to the landfill at their end of life. These numbers are then scaled by the expected weight of the CSAM material, which leads to:

$$\mathrm{GWP}_{\mathrm{B,CSAM}} = 0.006 \cdot (-0.022 + 4.45 + 0.031 + 0.00061 + 0.0073 + 0.0717)$$

$$\mathrm{GWP}_{\mathrm{B,CSAM}} = 0.02723 \text{ kg } \mathrm{CO_2}$$

New bolts are required for this connection, which adds an additional GWP of 1.084 kg CO_2 onto the final sum for scenario B. This value is found from this calculation, which utilizes the GWP values from table 7.1 for new steel, but only for the weight needed for the bolts:

$$\mathrm{GWP}_{\mathrm{rivets}} = (989 + 220 + 1.12 + 9.68 + 26.7 + 0.964) \cdot \frac{0.414 + 0.455}{1000}$$

$$\mathrm{GWP}_{\mathrm{rivets}} = 1.084 \text{ kg } \mathrm{CO_2}$$

The GWP value for scenario B is thus:

$$\mathrm{GWP}_{\mathrm{B}} = 0.0273 + 1.084 \text{ kg } \mathrm{CO_2}$$

$$\mathrm{GWP}_{\mathrm{B}} = 1.11 \text{ kg } \mathrm{CO_2}$$

Therefore, the final GWP values for each scenario are summarized below.

Element	**GWP (kg CO_2e)**
Scenario A	6.72
Scenario B	1.11
Scenario C	12.68

Table 7.4: Summary of Global Warming Potential (GWP) for selected elements.

7.5 Interpretation

7.5.1 Lifetime Extension

The lifetime extension of each scenario must be taken into consideration in this analysis.

Scenario A

Replacing the damaged connection with a new connection consisting of recycled steel will extend the main girder's lifespan by 100 years, given the fact that the girder itself has not undergone critical damage that will jeopardize its performance, such as plastic yielding, cracking, or extreme corrosion. This way, the bridge will be able to carry out an entire second life cycle with a GWP of 6.72 kg CO_2.

Scenario B

For the retrofitted scenario, the existing connection is scanned for fatigue cracks, where they are expanded and refilled with 316L deposit material. According to the assumptions stated in the scope, this will extend the connection's service life by 10 years before maintenance is required. Assuming that maintenance consists of reopening and refilling the same crack due to material degradation or debonding, the same process and amount of CSAM is applied at each maintenance stage. To reach the service life of 100 years, 10 maintenance checks are required. If the bolts need to be replaced each time, since rivets are not reusable, then the scenario B GWP of 1.11 kg CO_2 must be multiplied by 10. The final GWP for scenario B during a 100 year life cycle is therefore 11.11 kg CO_2.

The final GWP emissions for scenario B to satisfy a 100 year lifespan is higher than that for scenario A. This is primarily because of the use of rivets, which cannot be reused after removal. It is recommended to use a different type of bolt for scenario B, one that can be reassembled and reused after taking it apart. This would reduce the GWP of scenario B to the following:

$$\mathrm{GWP_B} = (0.0273) \cdot 10 + 1.084 \text{ kg CO}_2$$

$$\mathrm{GWP_B} = 1.357 \text{ kg CO}_2$$

This is because only the initial CSAM application requires new bolts (the same GWP as for the rivets was added due to the unknown geometry of the alternative bolts for simplicity), and only the CSAM GWP contributes for each maintenance application.

Scenario C

The same life expectancy is met as for scenario A, only with a GWP of 12.68 kg CO_2.

SUmmary

To summarize, the final values of GWP for each scenario according to the functional unit of extending the main girder's lifespan by 100 years are the following:

Element	**GWP (kg CO_2e)**
Scenario A	6.72
Scenario B (rivets)	11.11
Scenario B (reusable bolts)	1.35
Scenario C	12.68

Table 7.5: Summary of Global Warming Potential (GWP) for selected elements.

To conclude, based on the assumptions of this analysis, if the use of rivets is necessary, the recycling scenario yields the least carbon emissions at 6.72 kg CO_2. If alternative bolts can be used instead that allow for disassembly and reassembly, then scenario B is the most environmentally efficient, yielding a GWP of 1.35 kg CO_2. Between the two, it is the most environmentally efficient solution to proceed with scenario B and use reusable bolts in the second life cycle of the main girder.

7.5.2 Total Embedded GWP Emissions

Since the connection impacts the entire girder's life expectancy, its embedded carbon if it fails is higher than what is listed in table 7.5. The GWP required for a new floor girder of the dimensions in the selected case study is:

$$\mathrm{GWP}_{\mathrm{girder}} = (989 + 220 + 1.12 + 9.68 + 26.7 + 0.964) \cdot \frac{14586000}{1000}$$

$$\mathrm{GWP}_{\mathrm{girder}} = 18195509.9 \text{ kg } \mathrm{CO}_2.$$

Failure of the connection would result in significant carbon emissions due to the girder's reliance on it. Selecting scenario B to retrofit the connection has significantly lower emissions depending on the bolt-type used, specifically 6 times lower emissions than the recycling scenario, however the life extension is not confirmed and the structural stability depends on multiple assumptions. Using this scenario poses a failure risk to the connection due to the uncertainties in the results, which would be significantly more disruptive in terms of environmental emissions as compared to scenario A. It is not recommended scenario B is used until experimental tests are conducted, and its structural reliability is confirmed.

In addition to the structural performance assumptions, there are several assumptions regarding scenario B's LCI. For instance, transportation and access to cold-spray equipment, the extracting and processing of the exact steel material into a powder, obtaining the specified gas type, pressure, and temperature, the prepping of the substrate material for deposit to take place, and post-deposition heat treatment all contribute to the GWP of the CSAM process. Unfortunately, no available data exists as of now that follows this exact process. Therefore the actual GWP of the cold spray application will increase once more research is conducted. It is possible that for scenario B with rivets, the GWP will exceed that of scenario C, or that the scenario B with reusable bolts will more closely resemble the GWP value of scenario A. Until this research is conducted and data is gathered, the final results are not available.

Until these assumptions are confirmed or disputed, it is best to proceed with scenario A, and using recycled material to replace the entire connection. This guarantees a 100 year lifespan extension for the main girder at approximately half the GWP emissions of replacing the connection with new material.

Chapter 8

Conclusions and Recommendations

8.1 Connecting Findings to the Initial Problem Statement

The transition toward a circular economy in the Netherlands requires engineering solutions that reduce raw material consumption, extend the service life of steel components, and minimize carbon emissions. Cold spray additive manufacturing (CSAM) presents a promising alternative to recycling by enabling the repair and reuse of end-of-life (EoL) steel elements without the carbon-intensive production of new steel. The structural performance of CSAM-retrofitted steel is strongly influenced by a range of parameters, including particle material and size, gas type, temperature and pressure, spray angle, and nozzle geometry. These parameters govern impact velocity, which in turn determines the deposit structural performance.

A key challenge identified in the literature is the trade-off between material performance and process cost, particularly concerning helium-based spraying, which produces highly ductile deposits but is economically unfeasable for the desired application. Nitrogen-based CSAM, combined with annealing and the use of a soft WIP interlayer, offers a feasible alternative for achieving sufficient ductility and bonding. With these considerations in mind, this thesis investigated the structural behavior of composite elements formed by an annealed 316L nitrogen-sprayed deposit applied to S235 carbon-steel substrates.

The following subsections summarize the findings of the numerical models and respond directly to the research questions, illustrating how CSAM retrofitting could contribute to extending steel component lifespan while supporting national circularity and CO_2 reduction goals.

8.1.1 What factors govern the structural performance of a steel element retrofitted with cold-spray deposited material?

A parametric study of tensile coupons was conducted to investigate how composite behavior is influenced by the deposit-to-substrate ratio, substrate strength, and bond interaction. Two numerical models (A.1 & A.2) were developed to study these effects.

Model A.1 examined the influence of substrate material by comparing S235- and S355-based composite coupons (Models A and B). Increasing substrate tensile strength resulted in higher yield and peak load capacities across all retrofit configurations. Coupons with S355 substrates consistently showed higher load-carrying capacity, with a 27.6% higher peak load than S235 in the unretrofitted case and a 11.9% increase at 50% retrofitting. Although S355 steel is initially 19% more ductile, this advantage decreased as increased retrofit volume caused the deformation response to become governed by the deposit material. For the 16% and 33% variants, damage initiation in the S355-based coupons was delayed by approximately 1 mm, corresponding to ductility increases of 8.7% and 8.0%, respectively. At 50% retrofitting, the displacement at peak load converged to 15.5 mm for both substrates, indicating fully deposit-dominated behavior. The greater mechanical mismatch between S235 and the 316L deposit resulted in larger incremental gains for S235-based coupons as retrofit percentage increased, with peak load and ductility increases of 12.4% and 24%, respectively, between the 33% and 50% variants. For the coupon configuration studied, the deposit–substrate interface was oriented parallel to the applied load, resulting in a uniform cross-section along the gauge length and preventing the formation of a weakened section perpendicular to loading. Under these conditions, strength mismatch did not induce premature debonding. This conclusion is valid under the assumptions of full shear interaction and the absence of a critical heat-affected zone in the net section, which were beyond the scope of this study but may appear as limitations in practice. Overall, the results demonstrate that matching substrate and deposit yield strengths is not required to prevent debonding for this geometry, and that increasing substrate strength primarily enhances load-carrying capacity, while ductility is eventually governed by the deposited material.

Model A.2 demonstrates the influence of successful bonding at the interface. Under full shear interaction, the composite elements exhibited increased yield strength by 40% to 166.7% for variants 16% to 50%, respectively. If the bonding is not sufficient, the deposit cannot effectively transfer load, and the element's capacity becomes significantly lower, since substrate material was removed to allow space for the deposit. Retrofitting through CSAM is only successful and should be performed when a certain amount of shear interaction is guaranteed, since applying a large amount of retrofit material also introduces a high risk of lowered tensile capacity. The exact limit remains unknown and must be explored in future research.

Overall, the structural performance of a steel element retrofitted with cold-spray deposited material is governed by three key factors: the substrate mechanical properties, the retrofit volume, and the degree of interfacial bonding. Retrofits with high deposit content and strong bonding show the most stable and predictable behavior, whereas insufficient bonding introduce significantly lower tensile capacities. Future work should focus on experimentally quantifying the minimum bond requirement needed for effective composite action.

8.1.2 How does cold-spray remanufacturing influence the overall structural performance of reclaimed steel elements with riveted connection damages?

A coupon specimen model was set up to accommodate the present cracking, and also pave the way for future experimental work. In these coupons, a hole radius with a notch and crack expanding from it were modeled, to represent a bolt hole experiencing fatigue cracking. The notch was part of the compact specimen geometry, but during application of CSAM, it is necessary to expand any existing cracks to allow for space to fill them. Therefore, when exploring ductile damage, the same geometry was used to represent an expanded crack, plus the precrack in case voids or sub-millimeter cracks still exist.

Two failure mechanisms were explored, each requiring its own model setups. This geometry was thus split into Model B and Model C.

Model B explored the stress intensity factors around the crack for a non-retrofitted and retrofitted notch. It showed that after retrofitting was applied, the applied load at which the crack reached its fast fracture increased by 935%, from 5.7 kN to 59 kN. The crack propagated on the side of the retrofit material, which can be attributed to the fact that the 316L has a slightly lower fracture toughness threshold, and that the load was placed directly above the notch. Had the fracture toughness threshold of the deposit been higher than the substrate, which is ideal for retrofitting fatigue-loaded elements, then the S235 side would have failed first at a load of 80 kN. This would increase the load capacity by an additional 36%. Therefore significant improvements in both the load and displacement capacities were observed from applying retrofit material to the open notch.

Model C explored ductile damage evolution, specifically around the interface of the two materials. The point of expected failure is around the two bolt holes where the boundary conditions are applied, since those two areas represent the weakest cross-section of the specimen. The intended area of study was around the interface to study debonding, therefore the mesh around the notch geometry was refined. Two additional models were run as performance reference points: a non-retrofitted and undamaged model. As expected, the ultimate tensile capacity increased from the non-retrofitted to the retrofitted models by 139.8% due to the increased area added to the specimen cross-section. Since the retrofit material is stronger than the S235 substrate, the tensile capacity of the retrofitted model exceeded that of the original model in the early plastic stages by 0.8%. Due to the significantly lower strength of the S235 steel, the substrate begins to fail at the interface, described as debonding. This uneven distribution of forces caused a preliminary damage evolution by in the specimen, thus lowering its ultimate tensile capacity by 4.7% and its fracture displacement by 31%. It is possible that using a lower-strength retrofit material will avoid this preliminary failure and allow the retrofitted specimen to perform as well as the original, assuming perfect bond is achieved.

While the two models cannot be directly compared due to the different modeling assumptions, the debonding occurs earlier in the load application stage than the fast fracture. It is therefore expected that under full shear interaction, ductile failure will govern as the primary failure mechanism, however this must be confirmed by running both models as non-linear.

What is the environmental impact of these techniques?

When considering two life cycles (the initial and the lifetime extension of a riveted connection in a steel bridge), the recycling scenario displayed the most promising results from both an environmental and structural perspective. When fatigue cracking occurs in the steel plate of a riveted connection, as defined by the LCA scope, this plate must be either retrofitted or replaced. In the retrofitting option, the plate remains intact and the added material from the CSAM process yields minimal CO_2 emissions, making this scenario (Scenario B) appear initially as the most favorable. However, the bolts may need to be removed prior to CSAM deposition to ensure full access to the cracked region. Since rivets are not reusable, new rivets must be installed during each maintenance cycle, which is estimated to occur ten times over a 100-year bridge lifespan. As a result, the Global Warming Potential (GWP) for Scenario B increases to 11.11 kg CO_2e. This value decreases significantly (to 1.35 kg CO_2e) if reusable bolts are used instead of rivets.

Replacing the damaged plate and bolts with recycled equivalents (Scenario A) provides a 100-year lifetime extension with a GWP of 6.72 kg CO_2e, which is nearly half that of

Scenario B. Under the assumptions of this study, Scenario A is therefore the more reliable solution for minimizing environmental impact.

In addition, the available EPD data did not specify the manufacturing and construction steps associated with 316L powder production. As a result, it remains uncertain whether high gas temperatures, powder atomization, and post-heat treatment were included in the reported GWP values. Further research is required to establish accurate emissions for both CSAM production and application. It is also crucial to determine the actual lifetime extension achievable by CSAM-retrofitted, fatigue-cracked steel elements. Once these values are known, the CO_2 emissions and scenario ranking may change, and a revised LCA should be performed.

8.2 Future Recommendations

ABAQUS Modeling

- Explore compression strength capacity and the governing failure mechanisms related to this load configuration.
- Apply cyclic loading to better resemble the typical loading applied to bridge elements.
- Explore a symmetrical geometry for the crack propagation study, where the hole, retrofitting, and load are located in the center.

Cold Spray Additive Manufacturing

- Conduct further research for CSAM optimization using a powder resembling the substrate material and determine the governing failure mechanism for the C(T) specimen.
- Repeat the research with the as-sprayed CSAM deposit and study the brittle failure mechanisms and the anisotropic material behavior in case heat treatment is not available.

Experimental Tests

- Explore bonding properties between deposit and substrate through experimental testing and modeling to complement model A.2.
- Conduct experimental tests to validate ABAQUS results for all models and verify or reject the concluded governing failures.

Fracture Mechanics

- Explore modes 2 and 3 of the fracture mechanics failure modes to complement this study on mode 1.
- Run a nonlinear model and study the J-integral outputs to compare the two nonlinear models for more accurate comparison of the B and C models.

LCA

- Conduct a life cycle analysis with updated data on 316L stainless steel powder and the optimized CSAM settings.

Bibliography

[1] M. Villa, S. Dosta, and J.M. Guilemany. Optimization of 316l stainless steel coatings on light alloys using cold gas spray. *Surface and Coatings Technology*, 235:220–225, 2013.

[2] European Commission. Communication from the commission to the european parliament, the council, the european economic and social committee and the committee of the regions - a new circular economy action plan - for a cleaner and more competitive europe, 2020. COM(2020) 98 final, Accessed: 2025-02-18.

[3] Government of the Netherlands. Circular dutch economy by 2050, 2025. Accessed: 2025-02-18.

[4] World Steel Association. December 2024 crude steel production and 2024 global totals, 2025. Accessed: 2025-02-13.

[5] Trading Economics. Netherlands trade in recyclable raw materials exports (extra-eu, eurostat data), 2025. Accessed: 2025-02-13.

[6] Bert Daniels, Marit van Hout, and Andrew Keys. Decarbonisation options for the dutch steel industry, December 2019. Accessed: 2025-02-13.

[7] H. Van Den Berg, G. Bettens, G. Kockelkoren, J. Van Gils, D. De Jong, Y. Lieffering, Royal Steel Federation, R. Kwintenberg, A. Averesch, B. Soetekouw, N. Hoogendijk, B. Evers, M. Den Hollander, M. Rubbens, S. Delrue, C. Van Dijken, H. Van Der Horst, F. Maatje, R. De Roos, and PMC. Steel construction agreement, 2022.

[8] Bouwakkoord Staal. Handleiding nta 8713:2023 - hergebruik van constructiestaal, 2025. Accessed: 2025-02-13.

[9] Alper Kanyilmaz, Mussie Birhane, Roy Fishwick, and Carlos del Castillo. Reuse of steel in the construction industry: Challenges and opportunities. *International Journal of Steel Structures*, 23:1399–1416, 10 2023.

[10] Shuo Yin, Pasquale Cavaliere, Barry Aldwell, Richard Jenkins, Hanlin Liao, Wenya Li, and Rocco Lupoi. Cold spray additive manufacturing and repair: Fundamentals and applications, 5 2018.

[11] Ryan B. Gottwald, R. Joey Griffiths, Dylan T. Petersen, Mackenzie E.J. Perry, and Hang Z. Yu. Solid-state metal additive manufacturing for structural repair. *Accounts of Materials Research*, 2:780–792, 9 2021.

[12] Behrouz Shafei and Weizhuo Shi. Use of cold gas dynamic spraying for repair of steel structures. Final report, Bridge Engineering Center, Iowa State University, Ames, Iowa, 2021.

[13] B. D. Schagen, S. Zhang, John A. Hart, Wen Chen, Haden Quinlan, and Simos Gerasimidis. Feasibility of 3d printing applications for highway infrastructure construction and maintenance. Technical Report 24-058, University of Massachusetts at Amherst. Transportation Center, August 2024. Prepared for the Massachusetts Department of Transportation, Office of Transportation Planning, and the United States Department of Transportation, Federal Highway Administration.

[14] Mohammad Al-Emrani. Fatigue performance of stringer-to-floor-beam connections in riveted railway bridges. *Journal of Bridge Engineering - J BRIDGE ENG*, 10, 03 2005.

[15] Reza Haghani, Mohammad Al-Emrani, and Mohsen Heshmati. Fatigue-prone details in steel bridges. *Buildings*, 2(4):456–476, 2012.

[16] NEN Standards Committee. NTA 8713:2023 nl, 2023.

[17] Huile Li and Gang Wu. Fatigue evaluation of steel bridge details integrating multiscale dynamic analysis of coupled train-track-bridge system and fracture mechanics. *Applied Sciences*, 10:3261, 05 2020.

[18] Rosemarie Helmerich. *Riveted Steel Bridges: Semantic Management of Knowledge*. PhD thesis, Wroclaw University of Technology, Poland, 2014.

[19] Iman Shakeri. Fatigue F9: Fracture Mechanics. Lecture notes, CIEM5240: Steel and Composite Structures, 2025. TU Delft course material.

[20] Iman Shakeri. Fatigue F10: Fatigue Crack Growth. Lecture notes, CIEM5240: Steel and Composite Structures, 2025. TU Delft course material.

[21] Abishek Kafle, Raman Silwal, Bikram Koirala, and Weihang Zhu. Advancements in cold spray additive manufacturing: Process, materials, optimization, applications, and challenges. *Materials*, 17(22), 2024.

[22] X. Wang, F. Feng, M. A. Klecka, M. D. Mordasky, J. K. Garofano, T. El-Wardany, A. Nardi, and V. K. Champagne. Characterization and modeling of the bonding process in cold spray additive manufacturing. *Additive Manufacturing*, 8:149–162, 2015.

[23] Surinder Singh, R. Raman, Christopher Berndt, and Harpreet Singh. Influence of cold spray parameters on bonding mechanisms: A review. *Metals*, 11:2016, 12 2021.

[24] S. Lett, J. Cormier, A. Quet, P. Villechaise, E. Meillot, and S. Hémery. Microstructure optimization of cold sprayed ti-6al-4v using post-process heat treatment for improved mechanical properties. *Additive Manufacturing*, 86:104168, 2024.

[25] S. Bagherifard, J. Kondas, S. Monti, J. Cizek, F. Perego, O. Kovarik, F. Lukac, F. Gaertner, and M. Guagliano. Tailoring cold spray additive manufacturing of steel 316 l for static and cyclic load-bearing applications. *Materials & Design*, 203:109575, 2021.

[26] A. List, C. Huang, L. Wiehler, C.-P. Gieseler, M. Schulze, F. Gärtner, and T. Klassen. Influence of ductility on fracture in tensile testing of cold gas sprayed deposits. *Journal of Thermal Spray Technology*, 32(6):1780–1795, 2023.

[27] Yusuke Hiwa, Tetsuhiro Shimozato, and Yoshiaki Tamaki. Denseness and adhesion of low-pressure cold spray coating to corroded steel bridges. *International Journal of Steel Structures*, 24, 2024.

[28] Yannik Sinnwell, Anton Maksakov, Stefan Palis, and Sergiy Antonyuk. Influence of the particle morphology on the spray characteristics in low-pressure cold gas process. *Powder Technology*, page 121084, 2025.

[29] H. Assadi, T. Schmidt, H. Richter, J.-O. Kliemann, K. Binder, F. Gärtner, T. Klassen, and H. Kreye. On parameter selection in cold spraying. *Journal of Thermal Spray Technology*, 20(6):1161–1176, 2011.

[30] N. Fan, Aran Rafferty, Rocco Lupoi, Wenya Li, Yingchun Xie, and Shuo Yin. Microstructure evolution and mechanical behavior of additively manufactured cocrfeni high-entropy alloy fabricated via cold spraying and post-annealing. *Materials Science and Engineering A*, 868:144748, 2023.

[31] Z. Zhao, N. ul H. Tariq, J. Tang, C. Jia, X. Qiu, Y. Ren, H. Liu, Y. Shen, H. Du, X. Cui, J. Wang, and T. Xiong. Microstructural evolutions and mechanical characteristics of ti/steel clad plates fabricated through cold spray additive manufacturing followed by hot-rolling and annealing. *Materials & Design*, 185:108249, 2020.

[32] M. Saleh, V. Luzin, and K. Spencer. Analysis of the residual stress and bonding mechanism in the cold spray technique using experimental and numerical methods. *Surface and Coatings Technology*, 252:15–28, 2014.

[33] S. Yin, N. Fan, C. Huang, Y. Xie, C. Zhang, R. Lupoi, and W. Li. Towards high-strength cold spray additive manufactured metals: Methods, mechanisms, and properties. *Journal of Materials Science & Technology*, 170:47–64, 2024.

[34] R.N. Raoelison, Ch. Verdy, and H. Liao. Cold gas dynamic spray additive manufacturing today: Deposit possibilities, technological solutions and viable applications. *Materials Design*, 133:266–287, 2017.

[35] K. Spencer and M.-X. Zhang. Optimisation of stainless steel cold spray coatings using mixed particle size distributions. *Surface and Coatings Technology*, 205(21):5135–5140, 2011.

[36] José Correia, Abilio De Jesus, A.L.L. Silva, Isabel Brás, Carlos Rebelo, Helena Gervasio, and Luís Silva. Fatigue behaviour of a riveted beam-to-column connection. 09 2016.

[37] S. Seitl, P. Pokorný, P. Miarka, J. Klusák, Z. Kala, and L. Kunz. Comparison of fatigue crack propagation behaviour in two steel grades s235, s355 and a steel from old crane way. In *MATEC Web of Conferences*, volume 310, page 00034. EDP Sciences, 2020.

[38] Yong Zhong, Yiyin Shan, Furen Xiao, and Ke Yang. Effect of toughness on low cycle fatigue behavior of pipeline steels. *Materials Letters*, 59(14):1780–1784, 2005.

[39] Standard test method for measurement of fracture toughness, 2021.

[40] ASTM International. ASTM E647-24: Standard test method for measurement of fatigue crack growth rates, 2024.

[41] NEN-ISO 6892: Metallic materials - tensile testing - part 1: Method of test at room temperature, 2019.

[42] Adam Kaľavský, Peter Palička, Róbert Huňady, and Michal Kicko. A comprehensive approach to the evaluation of material properties of s235jr steel. *Acta Mechanica Slovaca*, 25(2):36–45, 2021.

[43] Ali Mustapha Alibe, A. A. Janga, and I. M. Alibe. Fracture mechanics assessment of a compact tension specimen using abaqus cae. *International Journal of Advances in Engineering and Management (IJAEM)*, 5(9):472–483, September 2023.

[44] Ahmed Elkady. 39 ABAQUS Tutorial: Ductile Damage For Metals, May 2025.

[45] Ahmed Elkady. 25 abaqus tutorial: Explicit solver dos and donts. YouTube, 2021. https://www.youtube.com/watch?v=CaNIBwlOygU.

[46] Environmental management — life cycle assessment — requirements and guidelines, 2006.

[47] Tamara Rosic. An introduction to life cycle assessments: From cradle-to-cradle and beyond. Online article, reTyre ECO Blog, 2024. Published October 1, 2024; Accessed: October 22, 2025.

[48] PRé Sustainability. Life cycle assessment (LCA) explained. https://pre-sustainability.com/articles/life-cycle-assessment-lca-basics/, 2022. Accessed on October 22, 2025.

[49] En 15978:2011 — sustainability of construction works — assessment of environmental performance of buildings — calculation method, 2011. European Standard.

[50] SSAB. The life cycle of steel, 2025. Accessed: 2025-10-22.

[51] World Steel Association. The steelmaking process, 2025. Accessed: 2025-10-22.

[52] Dileep Kumar, Suresh Palanisamy, Kannoorpatti Krishnan, and Md Morshed Alam. Life cycle assessment of cold spray additive manufacturing and conventional machining of aluminum alloy flange. *Metals*, 13(10), 2023.

[53] Stalia AB. Steel beams. Environmental Product Declaration (EPD), October 2023. Accessed: 2025-10-24.

[54] NEOKEM S.A. Pp652 (12-30% tio$_2$) architectural super durable smooth matt bonded powder coatings (class 2), epd-ies-0008150:004 (s-p-08150). Environmental Product Declaration (EPD), 2023. Accessed: 2025-10-27.

[55] JUAL A/S. Building profiles in stainless steel – environmental product declaration epd-ies-0012086:002 (s-p-12086). Environmental Product Declaration (EPD), 2024. Accessed: 2025-10-27.

Appendix A

Tensile Coupon Dimensioning

According to these standard requirements, the following calculations were done to size the first-stage coupons according to the selected plate thickness:

$$t = 3 \text{ mm} \qquad \text{(thickness)}$$

The width-to-thickness ratio shall not exceed an 8:1 ratio. For this thesis, the maximum limit was selected to account for any additional dimensioning required when cracking is present:

$$\frac{b_0}{t} = 8$$

$$b_0 = 8 \cdot t$$

$$b_0 = 8 \cdot 3 \text{ mm} = 24 \text{ mm}$$

Cross-sectional area of the necked section is

$$S_0 = b_0 \cdot t$$

Substitute $b_0 = 24$ mm and $t = 3$ mm:

$$S_0 = 24 \text{ mm} \times 3 \text{ mm} = 72 \text{ mm}^2$$

Next, we compute the minimum coupon lengths based off these initial dimensions.

Original gauge length L_0

Formula:

$$L_0 = k\sqrt{S_0}$$

Using the standard and alternative k values:

$$k = 5.65 : \quad L_0 = 5.65 \cdot \sqrt{72} \quad = 47.942 \text{ mm}$$

(Check: the minimum allowed L_0 is 15 mm. The output value exceeds this, thus we can proceed.)

Parallel length L_c (proportional test pieces)

Formula (proportional pieces, non-cylindrical):

$$L_c \geq L_0 + 1.5\,\sqrt{S_0}$$

Substitute values:

$$\text{For } k = 5.65: \quad L_c \geq 47.942 + 1.5 \cdot \sqrt{72} \quad = 60.670 \text{ mm}$$

Parallel-side test-piece special rule

Note: the special rule “for parallel side test pieces less than 20 mm wide set $L_0 =$ 50 mm” does *not* apply here because $b_0 = 24$ mm > 20 mm.

Transition radius (as provided)

For this type of coupon (non-cylindrical), a transition radius of = 12 mm is needed.

Grips and end width

Requirement:

$$\text{width of gripped ends} \geq 1.2\,b_0$$

Width of gripped ends:

$$2\,r + b_0 = 2 \times 12 \text{ mm} + 24 \text{ mm} = 48 \text{ mm}$$

Minimum limit check:

$$1.2\,b_0 = 1.2 \times 24 \text{ mm} = 28.800 \text{ mm}$$

$$48 \text{ mm} \geq 28.800 \text{ mm}$$

Summary of computed numeric values

$$\begin{aligned} S_0 &= 72.000 \text{ mm}^2 \\ L_0(k = 5.65) &= 47.942 \text{ mm} \\ L_c\ (\text{prop.}, k = 5.65) &\geq 60.670 \text{ mm} \\ \text{Gripped-end width} &= 48 \text{ mm} \\ \text{Transition radius} &= 12 \text{ mm} \end{aligned}$$

Appendix B

Compact Specimen Dimensioning

Numerical Evaluation for base width $1.25W = 24$ mm

For a specimen width of base width $1.25W = 24$ mm, a summary of the final parameters can be seen in Table B.1. This width was selected to match the neck width of the tensile coupons from the first stage of the modeling.

For the selected base width of $1.25W = 24$ mm, the actual specimen width W is first determined as:

$$W = \frac{24}{1.25} = 19.2 \text{ mm}.$$

All subsequent dimensions are calculated as proportional values of W, according to the ASTM E1820 requirements.

The specimen depth, d, is defined as $0.188W$, giving:

$$d = 0.188(19.2) = 3.61 \text{ mm}.$$

The specimen height, H, is set to $1.20W$, therefore:

$$H = 1.20(19.2) = 23.04 \text{ mm}.$$

The specimen thickness, B, corresponds to half the width, calculated as:

$$B = 0.50(19.2) = 9.6 \text{ mm}.$$

Next, the total notch length, a, is determined as 70% of W:

$$a = 0.70(19.2) = 13.44 \text{ mm}.$$

The inner notch height, h, represents 6.3% of W:

$$h = 0.063(19.2) = 1.21 \text{ mm}.$$

From this, the sharpened notch length, a_s, is obtained using a trigonometric relationship that depends on the notch opening angle of 30°:

$$a_s = \frac{h/2}{\tan(30^\circ)} = \frac{1.21/2}{\tan(30^\circ)} = 1.05 \text{ mm}.$$

The precrack minimum length was defined as the maximum value between $h/2$ and 0.25 mm.

$$h/2 = 1.21/2 = 0.605 \text{ mm}$$

The value 0.605 mm is thus selected as the initial precrack value. This value must be checked against the following requirement:

$$a_p + a_s \geq 2.0\,h$$

This results in:

$$a_p + a_s = 1.65 \text{ mm}, \qquad 2.0\,h = 2.42 \text{ mm}$$

The initial precrack length does not suffice. It must be increased to 1.4 mm to surpass both requirements, which is calculated by rearranging the previous equation:

$$2.0\,h - a_s = a_p \qquad 2(1.21) - 1.05 = 1.4 \text{ mm}$$

Finally, the outer notch height, h_o, and the outer notch width, w_o, are then calculated as 20% and 10% of the width, respectively:

$$h_o = 0.20(19.2) = 3.84 \text{ mm}, \qquad w_o = 0.10(19.2) = 1.92 \text{ mm}.$$

Parameter	**Value (mm)**
W	19.2
d	3.61
H	23.04
B	9.6
a	13.44
h	1.21
a_s	1.05
h_o	3.84
w_o	1.92

Table B.1: Dimensional evaluation of specimen geometry for $1.25W = 24$ mm.

Additional Notes

- All linear dimensions shall comply with a tolerance of $\pm 0.013\,W$.
- The pin hole shall be sized so that the maximum clearance with the pin does not exceed $0.01\,W$.
- The crack-starter notch shall be centered within $\pm 0.005\,W$ of the specimen mid-height.

Appendix C

Tensile Coupon Results

C.1 Tensile Coupons - Behavior and Analysis

Retrofitting Tensile Coupons - Sensitivity Analysis

A sensitivity analysis was performed with varying thicknesses of the deposit and substrate, where their gross thickness remained at 3 mm. The vertical lines in the plots in figure C.1 represent the displacement corresponding with the yield strain, which was calculated with Hooke's law by multiplying the yield strain of the material by the length of the coupon. These plots are the same as plots 6.2, run as nonlinear models without ductile failure. In this case, the strain at which each variant yielded was quite different, since the yield point of 316L and S235/S355 materials are quite different.

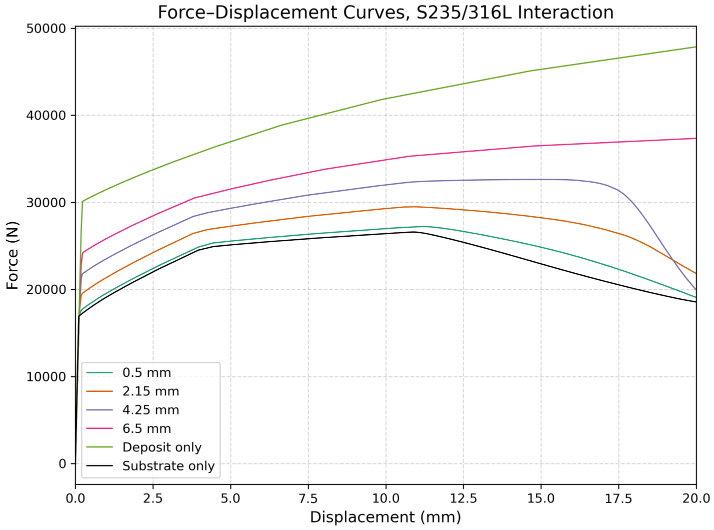

(a) Force-displacement plots of sensitivity analysis for varying deposit-to-substrate widths

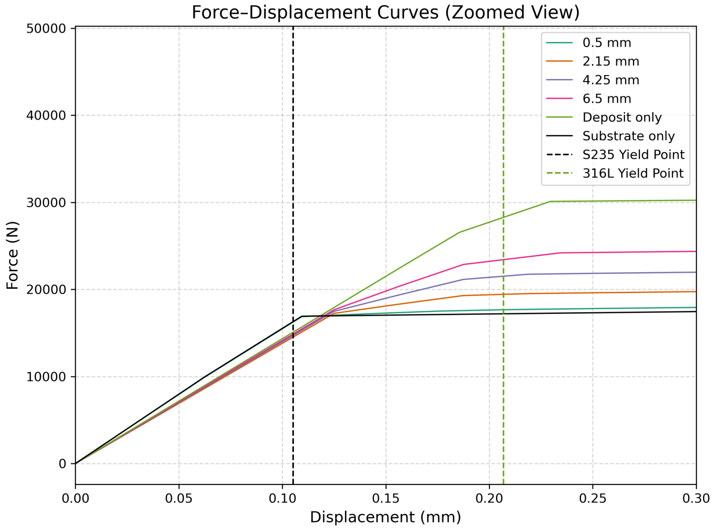

(b) Zoomed-in force-displacement plots of sensitivity analysis for varying deposit-to-substrate widths

Figure C.1: Sensitivity analysis plots for different deposit-to-substrate widths.

Deposit Orientation Comparison

Originally, the coupons were retrofitted across their thickness from one side. This asymmetric geometry can make the coupons prone to eccentricity depending on the stiffness of the materials, therefore a new geometry was introduced, where equal parts of material were applied to each side of the coupon, providing a symmetric distribution. The two orientations had three variants of retrofit material, each characterized by the percentage of volume of the overall coupon. The percentage of CSAM volume was kept consistent between the two, denoted by percentages 16%, 33%, and 50%.

The results are plotted in figures C.2a, C.2b, and C.2c. As the percentage of retrofit material increases, the tensile strength capacity follows. Comparing the values in the last figure, figure C.2c, the capacity at yield increases by 3.2 %, and the capacity at the final point increases by 2.6%. This value is not very significant, but it confirms the hypothesis that asymmetry in the geometry weakens the overall performance of the specimen, A likely possibility for this is due to eccentricity and uneven distribution of stresses.

Displacement D (mm)	Load P (N)
Retrofit Across the Width	
0.234 **(yield)**	$24,192$
20 **(final value)**	$37,336$
Retrofit Across the Thickness	
0.205 **(yield)**	$23,440$
20 **(final value)**	$36,382$

Table C.1: Displacement and load values for yield and ultimate points for two retrofit configurations.

For the models with smaller percentages of retrofitted volume, the tensile capacities are nearly identical, however the ultimate failure occurs at different points. Ductile damage was not considered for these models, therefore the degradation data from the force-displacement plots is neglected in the analysis.

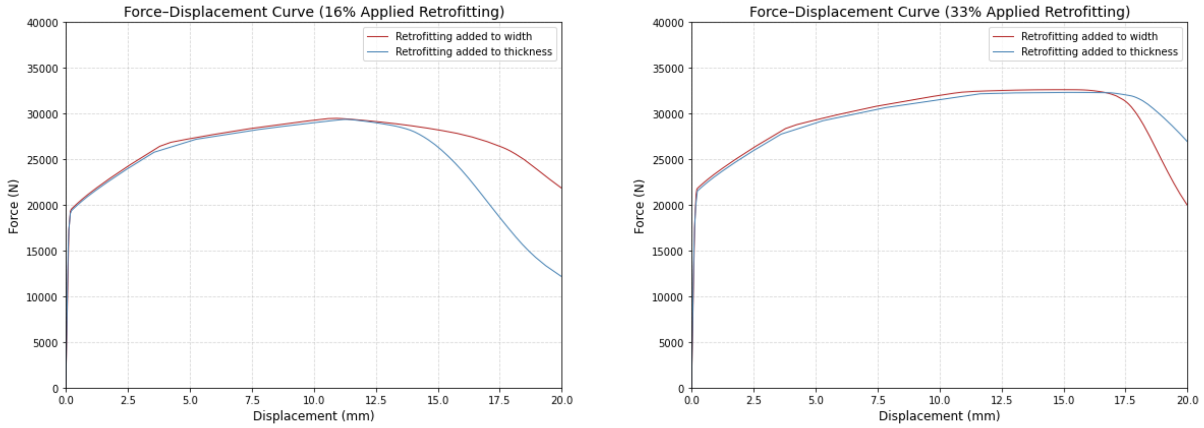

(a) 16% retrofitting

(b) 33% retrofitting

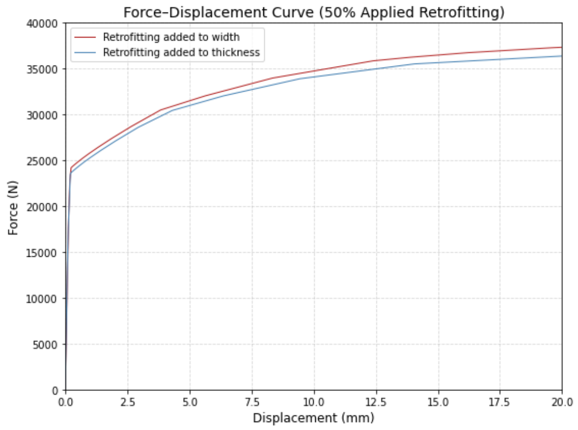

(c) 50% retrofitting

Figure C.2: Comparison of 16%, 33%, and 50% retrofitting applied across width and thickness.

Base Material Comparison

After incorporating ductile damage in the model variants, the following figure shows the last step of each simulation. The damage initiated from the substrate for each variant.

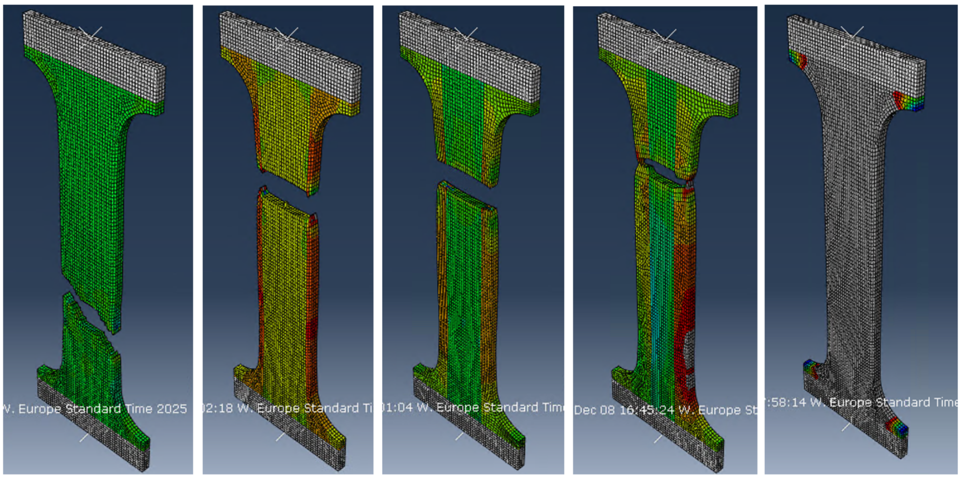

(a) ABAQUS simulations of all variants from S235 substrate.

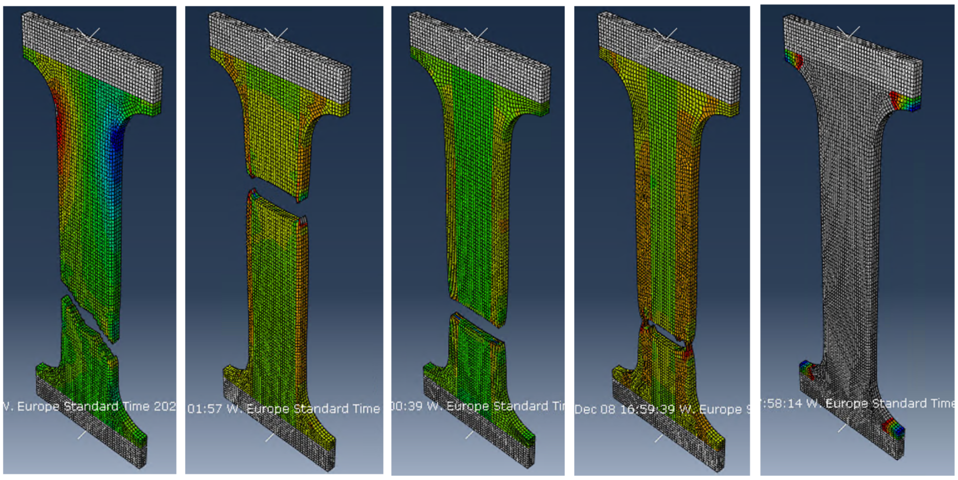

(b) ABAQUS simulations of all variants from S355 substrate.

Figure C.3: ABAQUS simulations showcasing ductile damage in all coupon variants.

The following plots and tables are from the models that do not include ductile damage, which are not as reliable as the updated ones. They were disregarded from the interpretation of results. The exact moments at which the substrate and deposit reached their UTS values were documented to understand the force-displacement behaviors:

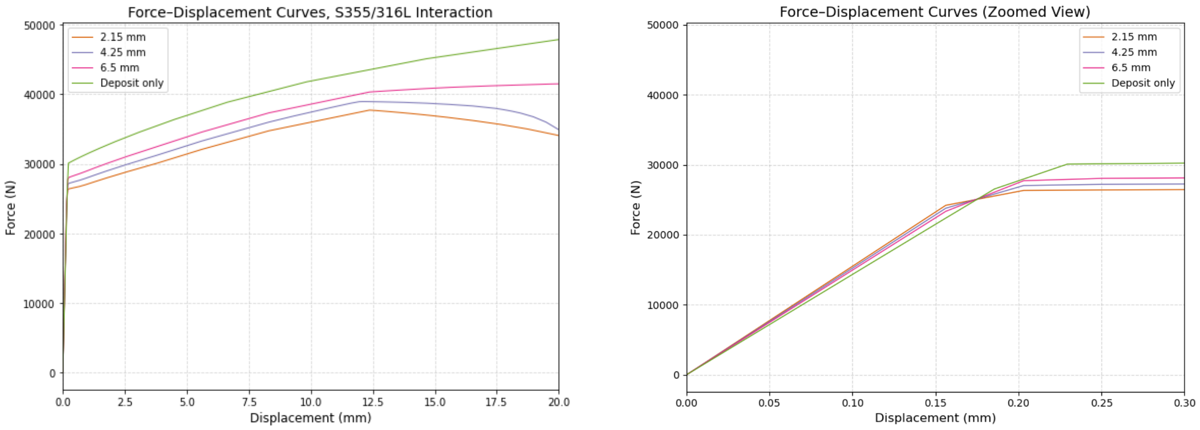

(a) Caption (b) Caption.

Figure C.4: Model B force-displacement curves under different retrofitting dimensions

50% (S235 / 316L)				
Step	S22 (S235 middle)	S22 (316L outer)	U2	P (N)
1	Yield (235)	Elastic	0.125	17655.8
3	Yield	Yield (418)	0.187	22860.1
16	UTS (370)	Yield	5.04	31557
20	UTS (370)	UTS (696)	14.8	36470.8

Table C.2: Model A: 50% retrofitted volume (S235 / 316L)

50% (S355 / 316L)				
Step	S22 (S355 middle)	S22 (316L outer)	U2	P (N)
3	Yield (355)	Elastic	0.203	27724.5
4	Yield	Yield (418)	0.25	28055.2
16	UTS (510)	Yield	8.312	37322.8
17	UTS (510)	UTS (696)	12.37	40382.5

Table C.3: Model B: 50% retrofitted volume (S355 / 316L)

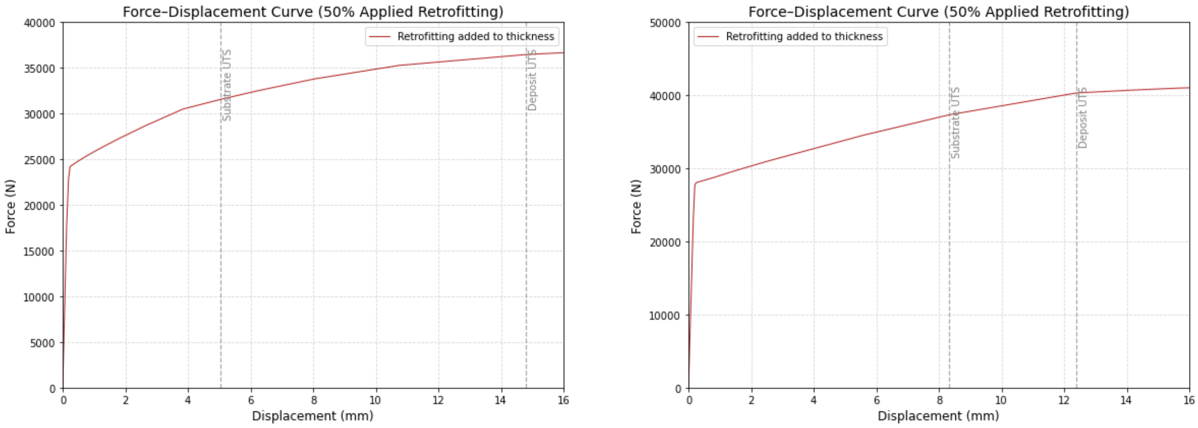

(a) Caption

(b) Caption

Figure C.5: 50% PD comparisons

33%				
Step	S22 (S235 middle)	S22 (316L outer)	U2	P (N)
1	Yield (235)	Elastic	0.125	17477.8
3	Yield	Yield (418)	0.187	21141.8
16	UTS (370)	Yield	4.24	28790.7
23	UTS (370)	UTS (696)	11.39	32429.8

Table C.4: ABAQUS results for 33% configuration.

33%				
Step	S22 (S355 middle)	S22 (316L outer)	U2	P (N)
3	Yield (355)	Elastic	0.203	27032.3
4	Yield	Yield (418)	0.25	27203.9
16	UTS (510)	Yield	8.312	35993.8
22	UTS (510)	UTS (696)	12.07	38943.9

Table C.5: ABAQUS results for 33% configuration (S355 / 316L).

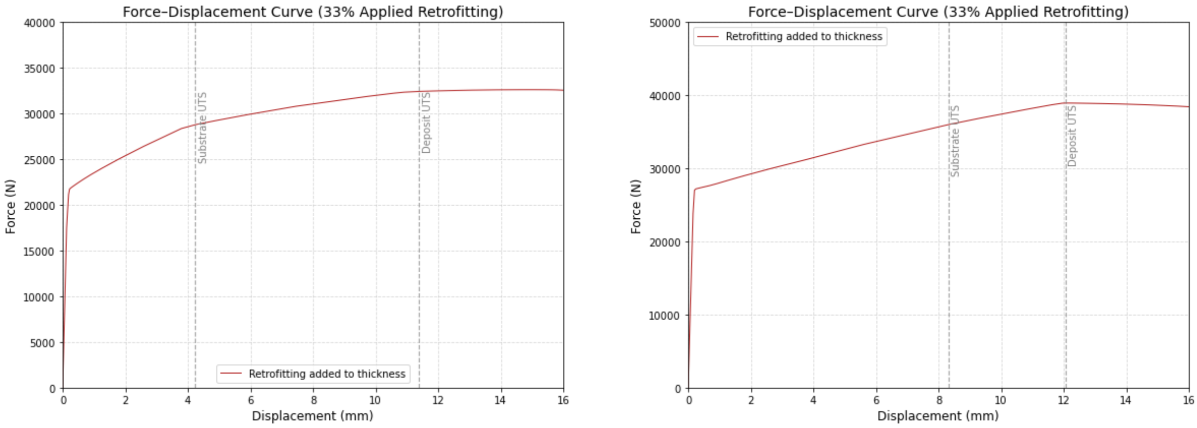

(a) Caption (b) Caption

Figure C.6: 33% PD comparisons

		16%		
Step	S22 (S235 middle)	S22 (316L outer)	U2	P (N)
1	Yield (235)	Elastic	0.156	17246.2
3	Yield	Yield (418)	0.187	19291.2
17	UTS (370)	Yield	4.918	27213.1
23	UTS (370)	UTS (696)	10.99	29474.7

Table C.6: ABAQUS results for 16% configuration.

		16%		
Step	S22 (S355 middle)	S22 (316L outer)	U2	P (N)
3	Yield (355)	Elastic	0.203	26336.2
4	Yield	Yield (418)	0.25	26408
16	UTS (510)	Yield	8.312	34745.1
17	UTS (510)	UTS (696)	12.37	37717.7

Table C.7: ABAQUS results for 16% configuration (S355 / 316L).

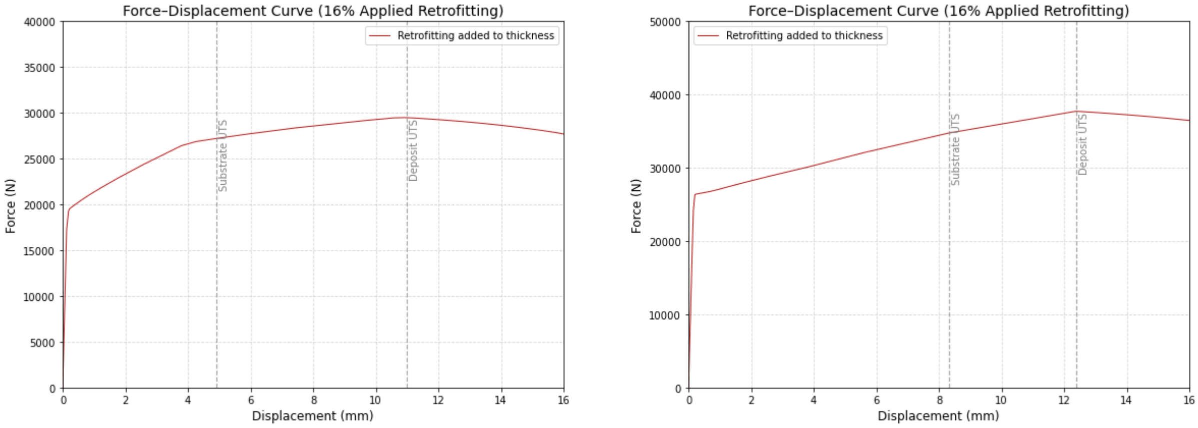

(a) Caption

(b) Caption

Figure C.7: 16% PD comparisons

Upper and Lower Bound Comparison

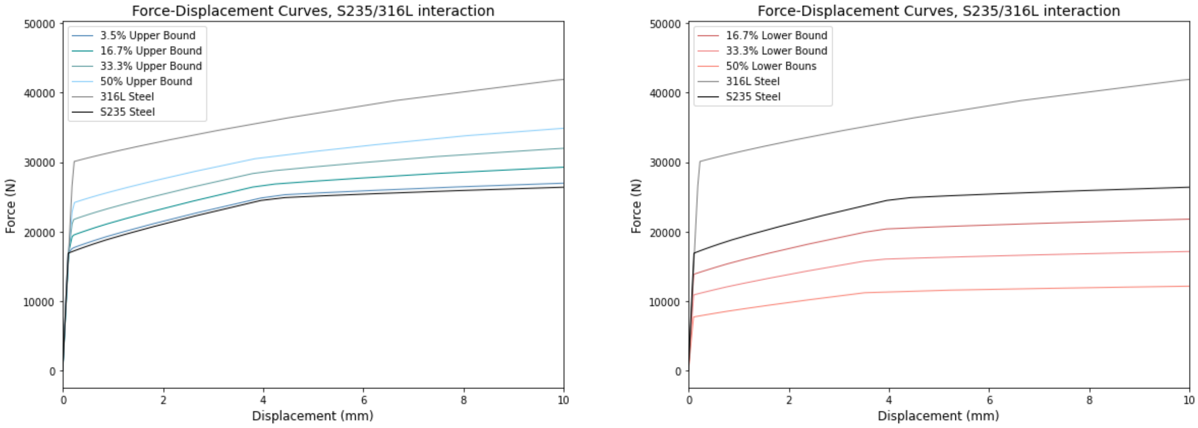

(a) Caption

(b) Caption

Figure C.8: 50% PD comparisons

Appendix D

Compact Specimen Results

D.1 Compact Specimen - Behavior and Analysis

Preliminary Hand Calculations - minimum required displacement to exceed K_{IC}

Initially while constructing the models, the following calculations were completed to understand approximately what value would suffice in exceeding the K_{IC} value of the steel. These equations are based off of a simple rectangular plate rather than a compact specimen, so they are not usable for the hand-calculation comparison. This step was done as a simplified assumption.

Table D.1: Input parameters used for fracture mechanics calculation.

Parameter	**Symbol**	**Value**
Crack length (disregarding the notch)	a	1.2 mm
Specimen depth (disregarding the notch)	d	15.9 mm
Plane-strain fracture toughness [37]	K_{IC}	$22.5\,\mathrm{MPa}\sqrt{\mathrm{m}}$ / $711.52\,\mathrm{MPa}\sqrt{\mathrm{mm}}$
Geometry factor constants [19]	A, B, C, D	1.26, 82.7, 76.9, -36.2
Gauge length	L	23.04 mm
Elastic modulus	E	210 000 MPa

As mentioned previously, small deflections are required to study the stress intensity factors near the crack. According to hand calculations, only 0.03 mm of applied vertical displacement is required to exceed the fracture toughness threshold, K_{IC}, of S235 material with the specified crack geometry. These calculations were completed using equations 2.1 and 2.3 from Section 2.2.1. The input parameters calculations can be seen below in table D.1 and the listed equations.

$$Y = \frac{1}{1 - \frac{1.2}{15.9}} \cdot \sqrt{\frac{1.26 + 82.7 \cdot \frac{1.2}{15.9-1.2}}{1 + 76.9 \cdot \frac{1.2}{15.9-1.2} - 36.2\left(\frac{1.2}{15.9-1.2}\right)^2}}$$

$$Y = 1.155$$

Since the model is displacement-controlled, the equation below displays the relationship between stress, σ, and applied displacement, ΔL.

$$\sigma = \frac{\Delta L}{h} \cdot E$$

Plugging this into equation 2.1, the equation can be rearranged to solve for the required applied displacement at which K_{IC} is exceeded, represented by equation D.1

$$\Delta L = \frac{K \cdot h}{Y \cdot E\sqrt{\pi \cdot a}} \tag{D.1}$$

Plugging in all the inputs from table D.1, the following calculation is done:

$$\Delta L = \frac{711.52 \cdot 23.04}{1.155 \cdot 210000 \cdot \sqrt{\pi \cdot 1.2}}$$

Resulting in this displacement value:

$$\Delta L = 0.0348\, mm$$

Using the provided parameters in Table D.1, Y is computed as approximately 1.15.The dimensions listed in the table exclude the notch dimensions.

Fracture Toughness Results and Interpretation

D.1.1 Model 1: Non-retrofitted cracked specimen (Open Notch)

Mesh Sensitivity Analysis

Four meshes were selected for this analysis, each specifying a different number of seeds along the countour line perimeter.

- Mesh 1: 16 seeds
- Mesh 2: 20 seeds
- Mesh 3: 28 seeds
- Mesh 4: 40 seeds

The individually plotted meshes are shown below in figure D.1. All contours converge for all meshes.

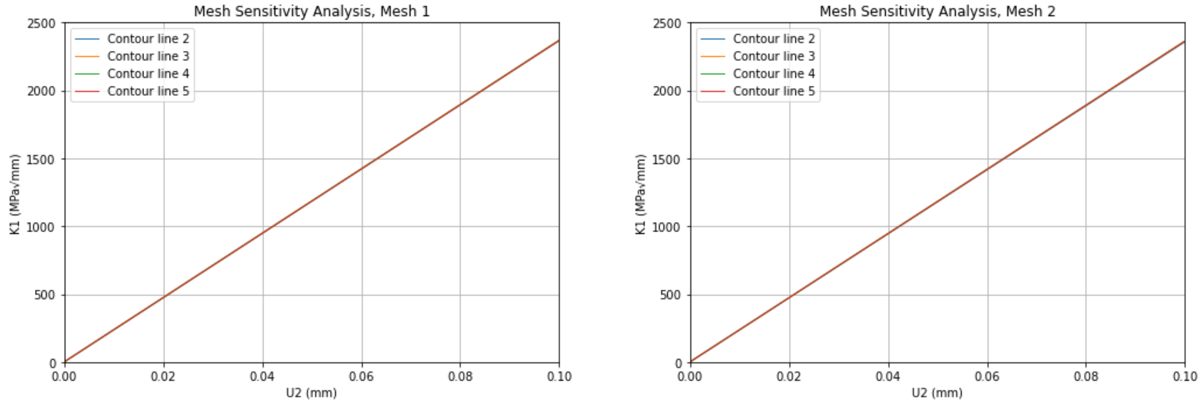

(a) K1 values from contour lines 2 - 4, displaying results from Mesh 1

(b) K1 values from contour lines 2 - 4, displaying results from Mesh 2

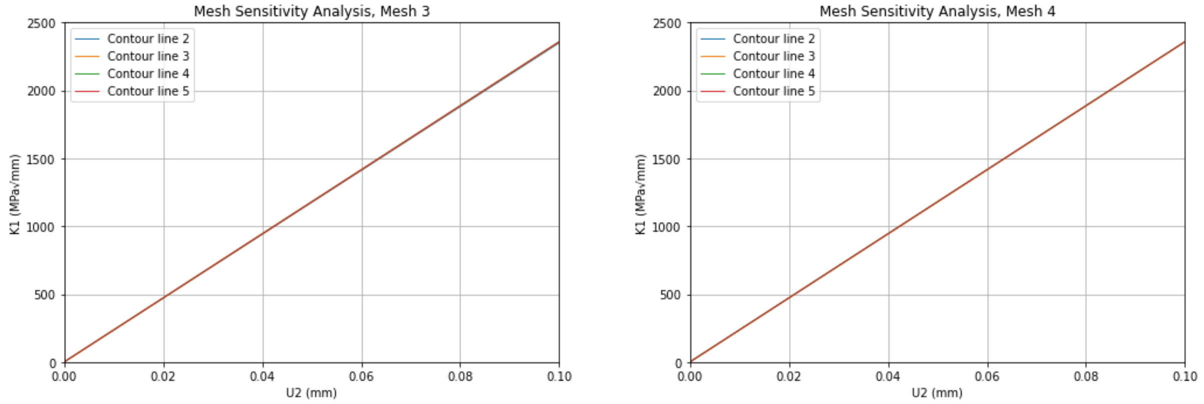

(c) K1 values from contour lines 2 - 4, displaying results from Mesh 3

(d) K1 values from contour lines 2 - 4, displaying results from Mesh 4

Figure D.1: Mesh sensitivity analysis of open model, displaying results from four contour lines.

All K1 values converge.

Hand Calculations and Discussion

The hand-calculated values were computed using the same notch length and specimen width as what was defined in the model. They were calculated based on a range of applied displacements, ranging from 0 to 0.08 in increments of 0.005 mm.

The following hand calculations for K1 were completed to plot against the ABAQUS outputs:

$$a = 4.9, \qquad B = 9.6, \qquad W = 19.2, \qquad k = 190577$$

As defined in the Results chapter, a is not the full notch length, but the length between the end of the notch to the point of load application.

The factor k was found from figure D.2, and it represents the proportional value between the force and the displacement of the linear elastic model.

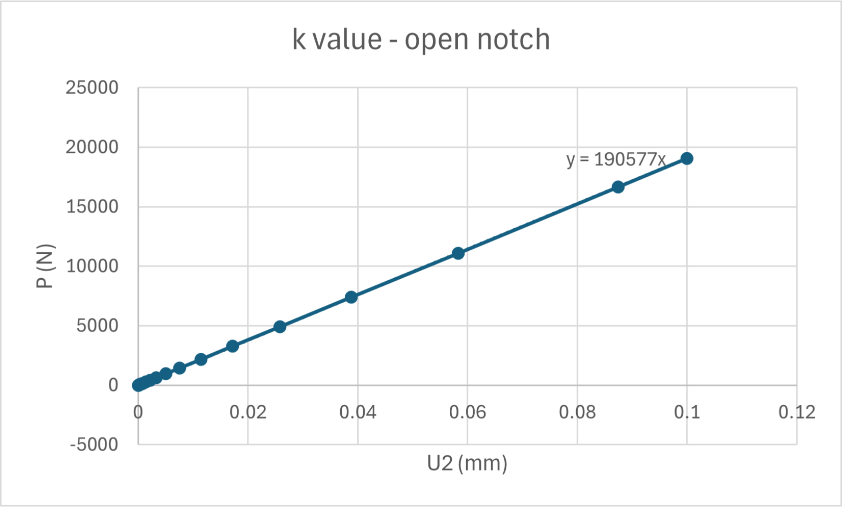

Figure D.2: Origin of k-ratio value, screenshot taken directly from ABAQUS

$$\frac{a}{W} = \frac{4.9}{19.2} = 0.2552083333$$

$$F\left(\frac{a}{W}\right) = \frac{2 + a/W}{(1 - a/W)^{3/2}}\left(0.886 + 4.64\frac{a}{W} - 13.32\left(\frac{a}{W}\right)^3 - 5.6\left(\frac{a}{W}\right)^4\right)$$

$$F = 6.403$$

$$K_1 = \frac{\Delta P}{B\sqrt{W}}F, \qquad \text{with} \quad \Delta P = \Delta \cdot k.$$

An example calculation is as follows,

$$\Delta P = 0.005 \times 190577 = 952.885$$

$$K_1 = \frac{952.885}{9.6\sqrt{19.2}} \times 6.403 \approx 145.05 \ (\text{MPa}\sqrt{\text{mm}})$$

All the values are seen below:

U (mm)	ΔP	ΔK (MPa$\sqrt{\text{mm}}$)
0.005	952.885	145.049831
0.010	1905.77	290.099662
0.015	2858.655	435.149493
0.020	3811.54	580.199324
0.025	4764.425	725.249155
0.030	5717.31	870.298986
0.035	6670.195	1015.348817
0.040	7623.08	1160.398648
0.045	8575.965	1305.448479
0.050	9528.85	1450.49831
0.055	10481.735	1595.548141
0.060	11434.62	1740.597972
0.065	12387.505	1885.647803
0.070	13340.39	2030.697634
0.075	14293.275	2175.747465
0.080	15246.16	2320.797296
0.085	16199.045	2465.847127
0.090	17151.93	2610.896958
0.095	18104.815	2755.946789
0.100	19057.7	2900.99662

D.1.2 Model 2: Retrofitted cracked specimen (Closed Notch)

The k value of the closed notch was found from the slope in figure D.3. This was used to find the corresponding P value at which the specimen reached fast fracture.

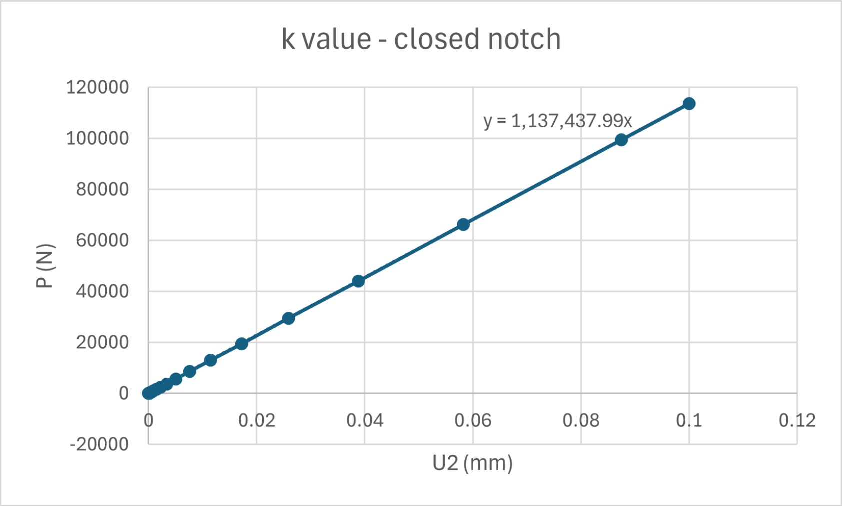

Figure D.3: Origin of k-ratio value, screenshot taken directly from ABAQUS

The following plots show the sensitivity analyses run for the mesh size, as well as the final results.

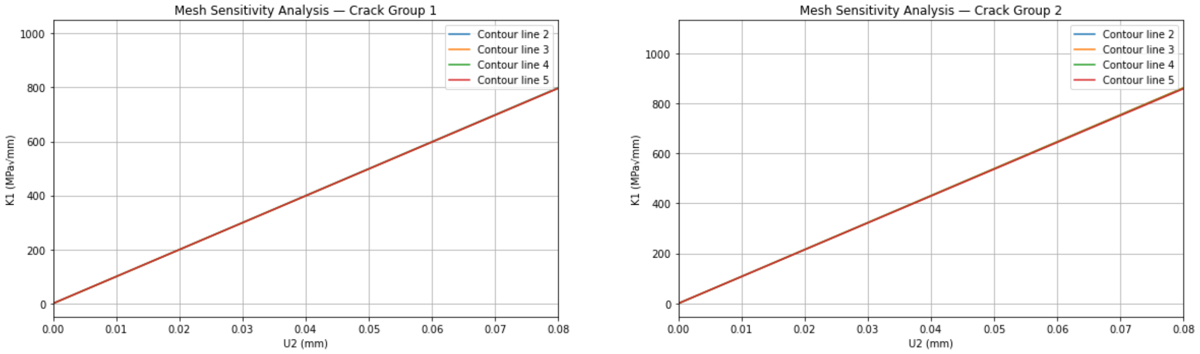

(a) Crack 1, converging K1 values from different contour lines

(b) Crack 2, converging K1 values from different contour lines

Figure D.4: Caption for Model 2 K_I results

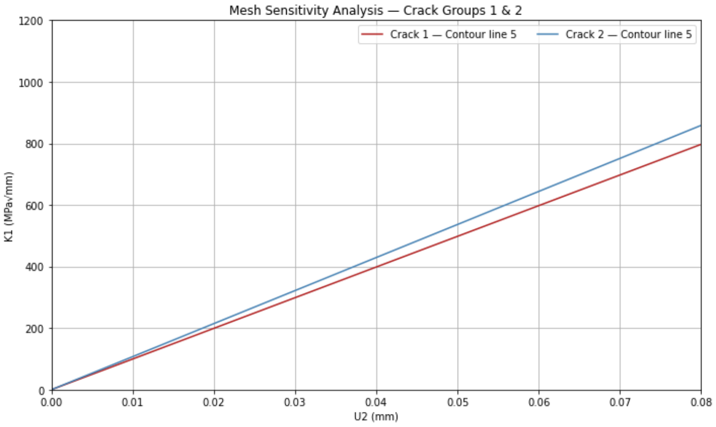

Figure D.5: Caption